The Dissertation Committee for Vishal Nayyar Certifies that this is the approved version of the following dissertation:

STRETCH-INDUCED WRINKLING OF THIN SHEETS

Committee:

Rui Huang, Supervisor

K. Ravi-Chandar, Co-Supervisor

Stelios Kyriakides

Chad M. Landis

Michael P. Marder

STRETCH-INDUCED WRINKLING OF THIN SHEETS

by

Vishal Nayyar, B.E.; M.S.E.

Dissertation

Presented to the Faculty of the Graduate School of

The University of Texas at Austin

in Partial Fulfillment

of the Requirements

for the Degree of

Doctor of Philosophy

The University of Texas at Austin

August 2013

Dedication

To My Parents

Acknowledgements

I would like to begin my acknowledgement by thanking my supervisor, Dr. Rui Huang, whose guidance and encouragement were a constant source of inspiration during my five years at the university. He has been an important mentor who helped me develop research and presentation skills. I would also like to express my gratitude to Dr. K. Ravi-Chandar for his interest in this research and helping me with the experimental study. I wish to thank my other committee members, Dr. Stelios Kyriakides, Dr. Chad Landis and Dr. Michael Marder for their helpful suggestions and insights through the course of this work. I am grateful to all the professors with whom I took courses at UT Austin.

I would like to thank my friends and colleagues who I came to know during my stay in Austin. In particular, I would like to thank Ali Ghahremaninezhad and Fasset Hickey, for helping me in using 3D-DIC technique; members of the machine shop for their help in preparing equipment for the experiments; Scott Messec for the IT support; Ranjiv Gupta for diligently reviewing my dissertation. A special thanks to all my friends at Austin, who made my life much easier and joyful. It was great to have them around during these years of my life; I thoroughly enjoyed their company.

Most importantly, my eternal gratitude goes to my family for their support. All of them have kept me in good spirits with their love and humor over all these years. It is because of them that I have been able to pursue and achieve my goals.

STRETCH-INDUCED WRINKLING OF THIN SHEETS

Vishal Nayyar, Ph.D.

The University of Texas at Austin, 2013

Supervisor: Rui Huang

Co-Supervisor: K. Ravi-Chandar

Thin sheets and membrane structures are widely used in space applications such as solar sails, sunshields and membrane optics. Surface flatness over a large area is one of the key requirements for many applications using the flexible thin structures. However, wrinkles are commonly observed in thin sheets. It is thus important to understand the mechanics of thin sheets for practical applications that require reliable control of surface wrinkles.

In this study, a model problem of stretch-induced wrinkling of thin sheets is considered. First, a two-dimensional (2-D) finite element model was developed to determine stretch-induced stress distribution patterns in hyperelastic thin sheets, assuming no wrinkles. As a prerequisite for wrinkling, development of compressive stresses in the transverse direction was found to depend on both the length-to-width aspect ratio of the sheet and the applied tensile strain. Next, an eigenvalue analysis was performed to predict the critical conditions for buckling of the elastic sheet under the

prescribed boundary conditions, followed by a nonlinear post-buckling analysis to simulate evolution of stretch-induced wrinkles.

Experiments were conducted to measure stretch-induced wrinkling of polyethylene thin sheets, using the three-dimensional digital image correlation (3D-DIC) technique. It was observed that the wrinkle amplitude first increased and then decreased with increasing nominal strain, in agreement with finite element simulations for a hyperelastic thin sheet. However, unlike the hyperelastic model, the stretch-induced wrinkles in the polyethylene sheet were not fully flattened at high strains (> 30%), with the residual wrinkle amplitude depending on the loading rate. The hyper-viscoelastic and the parallel network nonlinear viscoelastic material models were adopted for finite element simulations to improve the agreement with the experiments, including the wrinkle amplitude, residual wrinkles and rate dependence.

Finally it is noted that wrinkling is sensitive to defects and material inhomogeneity in thin sheets. By varying the elastic stiffness in a narrow region, numerical simulations show drastically different wrinkling behavior, including the critical strain and evolution of wrinkle amplitude and wavelength. In conclusion, a comprehensive understanding of stretch-induced wrinkling is established, where geometry, material, and boundary conditions all play important roles.

Table of Contents

List of Tables

List of Figures

CHAPTER 1

Introduction

1.1 RESEARCH MOTIVATION

Wrinkles are commonly observed in thin sheets as shown in Figure 1.1. Specifically, Figure 1.1a shows a Mylar cylindrical shell pressurized and then subjected to bending [Stein et al., 1961]. The longitudinal stress in the upper half of the cylinder is compressive due to bending and responsible for wrinkling observed in the figure. The wavelength, amplitude and extension of the wrinkles depend on the internal pressure, thickness, diameter and bending applied to the cylinder. Similar bending-induced wrinkles were observed in steel tubes by Aguirre et al. (2004) and Hallai and Kyriakides (2011). Figure 1.1b shows wrinkles in an annular pre-stretched rubber sheet subject to in-plane torsion applied through rotation of the hub. In this case, one of the in-plane principal stresses is compressive, and causes the wrinkles. Under the same boundary conditions, wrinkles were also observed in thin sheets of Polyester, Teflon and PVC coated textile [Miyamura, 2000]. Figure 1.1c shows wrinkling in a spherical shell of polyethylene that occurred due to a vertical concentrated load applied on surface of the shell [Szyszkowski et al., 1987]. Figure 1.1d shows wrinkles in a clamped thin sheet of Kapton subjected to shear [Wong et al., 2006a]. Similar to torsion, shearing of the clamped edges leads to a compressive principal stress in an inclined direction, which generates wrinkles. In Figure 1.1e, the polyethylene sheet is clamped at two opposite

ends and then stretched uniaxially in the longitudinal direction [Cerda et al., 2002]. In this case, wrinkles appear at the center of the sheet. Although less intuitive, it has been shown that uniaxial stretch with the clamped ends induces compressive stresses in the transverse direction [Friedl et al., 2000; Zheng, 2010], which is a necessary condition for wrinkling. Figure 1.1f shows wrinkling in a sheet metal that occurred during the cylindrical cup deep drawing process [Kim et al., 2003]. In this process the cylindrical punch applies a radial inward stretch to the metal sheet, which leads to circumferential compression and hence wrinkling as shown in the figure. In this case, wrinkling is permanent due to plastic deformation. Figure 1.1g shows wrinkling in a thin square Kapton sheet subject to point loads applied at the sheet corners [Blandino et al., 2002]. In Figure 1.1h, a thin square Kapton sheet was clamped at two opposite corners and then stretched, similar to the case shown in Figure 1.1e. Figure 1.1i shows wrinkles in a rubber sheet due to the transverse impact loading, which results in circumferential compression, leading to radial wrinkles as observed. Several other examples of wrinkling were discussed by Jenkins et al. (2006).

Among all the examples shown, a common feature observed is that one of the in-plane principal stress components is compressive, leading to wrinkling. The wrinkled regions relax the compressive stress by deforming into a lower energy bending state than the higher energy in-plane compression. The presence of compressive stress is a necessary but not a sufficient condition for wrinkling. Both sheet geometry and the boundary conditions play critical roles in the wrinkling behavior. There have been several

studies on wrinkling of thin sheets under various boundary conditions, but the effects of material properties on the wrinkling behavior have not been well understood.

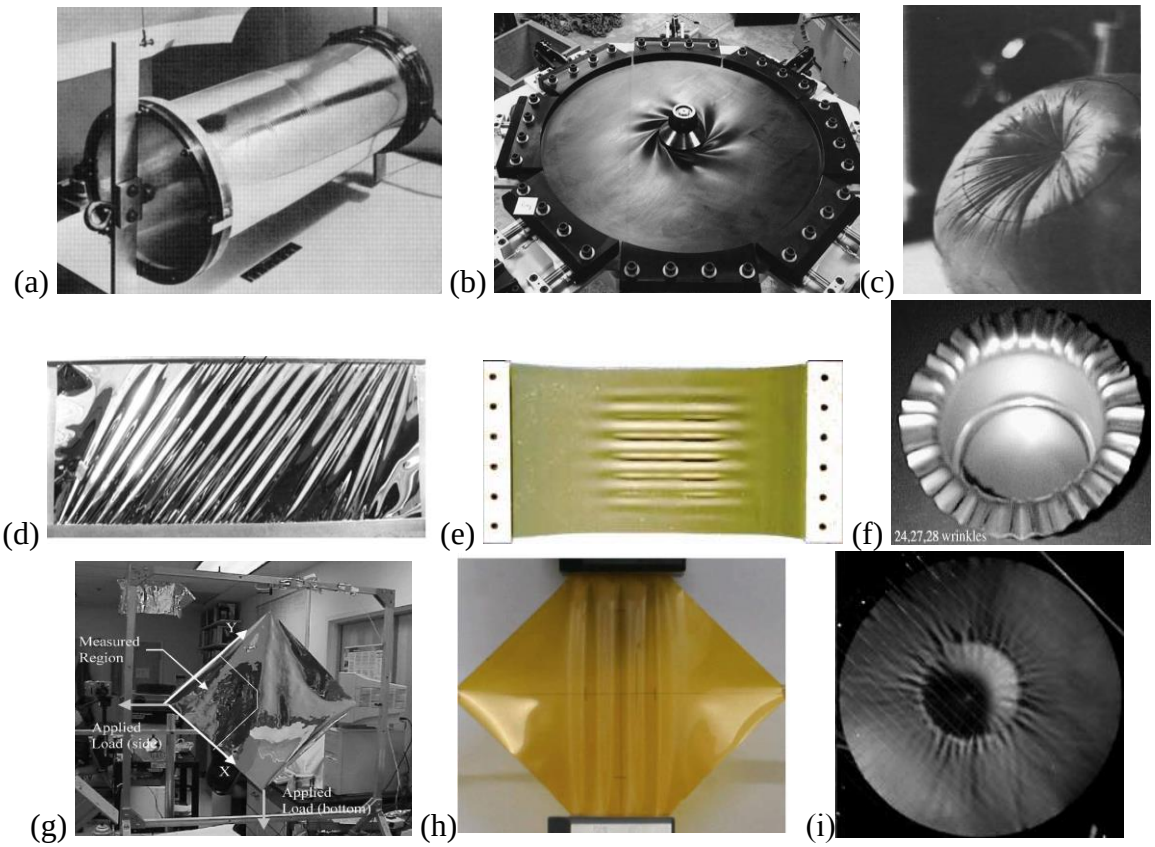

Figure 1.1: (a) Wrinkling of a pressurized Mylar cylindrical shell under bending [Stein et al., 1961] (b) Wrinkling of a stretched annular rubber sheet due to rotation of its hub [Miyamura, 2000]; (c) Wrinkles in a spherical polyethylene shell due to a vertical point load [Szyszkowski et al., 1987]; (d) Wrinkling of a rectangular Kapton sheet subjected to shear [Wong et al., 2006]; (e) Wrinkling of a uniaxially stretched rectangular polyethylene sheet [Cerda et al., 2003]; (f) Wrinkles in a sheet metal as a result of cylindrical cup deep drawing process [Kim et al., 2003]; (g) Wrinkles in a square Kapton sheet under point loads acting at the corners [Blandino et al., 2002]; (h) Wrinkles in a square Kapton sheet clamped at the two corners and subjected to tension along one of its diagonals [Wang et al., 2009]; (i) Wrinkling in a thin rubber sheet due to transverse impact loading [Vermorel et al., 2008].

The examples in Figure 1.1 show occurrence of wrinkles in a wide range of materials under a variety of loading conditions. Thus, for practical applications of thin sheets that require better control over surface flatness, it is important to understand the mechanics of wrinkling. Typically, wrinkles form as a result of structural instability under compressive stresses. These wrinkles may be permanent or temporary. The permanent wrinkles occur as a result of permanent plastic deformation and are also called material or plastic wrinkles. Temporary wrinkles form due to elastic buckling of thin sheets and can be removed by unloading. Such wrinkling is also called structural or elastic wrinkling. A few practical applications of thin sheets are described in Section 1.2.

1.2 APPLICATIONS OF THIN SHEETS

1.2.1 Space Structures

Due to their lightweight and low space requirements, thin sheets and membrane structures are used in many space applications such as inflatable space antennas, solar sails, sun shields, radars and solar energy systems (Talley et al., 2002; Sleight et al., 2005; Sakamoto and Park, 2005; Redell et al., 2005; Wang et al., 2007; Peypoudat et al., 2005). For some of these applications, as described below, surface flatness over a large area is one of the key requirements and reliable control of surface wrinkling is critical.

a. Solar Sails

A solar sail is a gossamer structure that has been proposed as a propulsion system for future space missions. Traditionally propulsion is accomplished in spacecraft through expelling of a propellant from an engine mechanism. Solar sails are made of thin polymer (Mylar or Kapton) sheets coated with aluminum. It generates thrust through the

momentum exchange between solar photons and the sail, thus the power source of a solar sail is essentially unlimited. Since the photon pressure is small, solar sails must be very large in surface area and light in weight. Typically the in-plane dimensions of a solar sail can go up to a few hundred meters where the thickness is only a few microns. These membrane structures are installed through inflatable booms, which allow unfolding of the large sails [Block et al., 2011]. In addition to large-scale solar sails, a subscale solar sail system (NanoSail-D, which was NASA's first-ever solar sail deployed in low-Earth orbit [Johnson et al., 2011]) has already been tested.

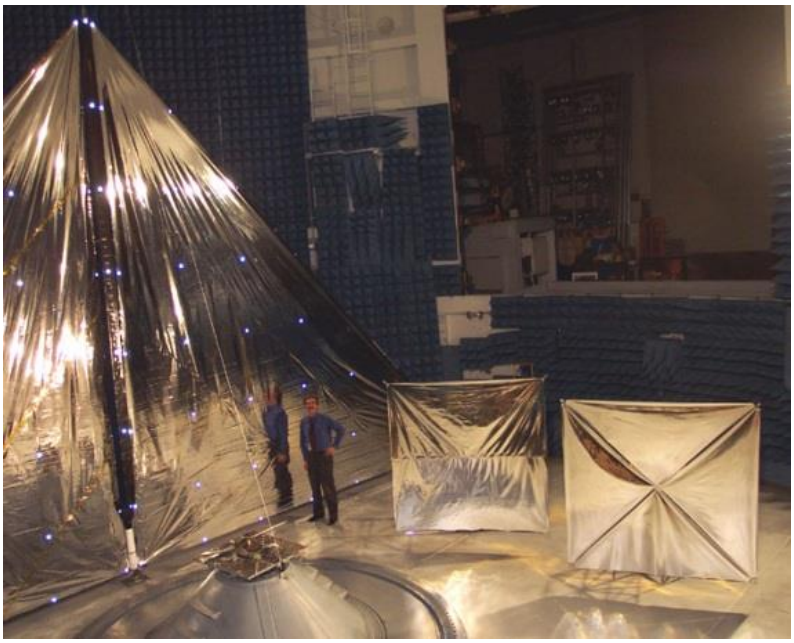

Figure 1.2: Two-Quadrant 10 m solar sail model and a 2 m solar sail model [NASA Langley Research Center].

A detailed study of the solar sail propulsion system is given in Garbe et al. (2006). Figure 1.2 shows a 2-quadrant 10 m and a full 2 m solar sail model with wrinkles clearly visible in both. It is estimated that solar sails can achieve speeds up to 70 km/s which is

equivalent to approximately 15 AU/yr. Wrinkles in the membrane solar sails may lead to controllability difficulties such as non-uniform sail loading, loss of momentum transfer to sail, and undesirable torques on the spacecraft [Talley et al., 2002].

b. Membrane Mirrors in Space Telescopes

There has been an increasing interest in using inflatable space based optical telescopes. The space telescopes use membrane mirrors that are made by coating metal on thin films. Figure 1.3a shows a schematic diagram of a membrane mirror space telescope setup that uses an inflatable membrane mirror (OTE). Traditionally such optical systems would involve massive, stiff substances such as low-expansion glass, beryllium, and similar materials, which are difficult for compact storage and deployment in space. Membrane optics offers the potential for orders of magnitude increase in aperture size and significant mass reduction for extremely lightweight space-based optical systems. In the absence of optical aberrations, the ability of such a telescope to resolve distant objects is directly proportional to the diameter of its collecting aperture. This leads to an increasing demand for larger aperture size of such mirrors with the diameter-to-thickness ratio in the range of 10^4 -10^7 [Blonk et al., 2006]. Currently, the 2.4 m mirror in diameter of the NASA Hubble Space Telescope (HST) is the largest mirror on orbit. The James Webb Space Telescope (JWST) will increase it up to 6.5 m in diameter by using an inflatable membrane mirror which is expected to be launched in 2018 [http://www.jwst.nasa.gov/]. Typically the membrane mirror needs to achieve the prescribed shape within the tolerance of tens of nanometers, based on the wavelength of the light to be studied. Since wrinkling in the membrane mirrors can cause large shape

errors, membrane apertures in space telescopes require exceptional surface accuracy with minimal wrinkles.

(a) 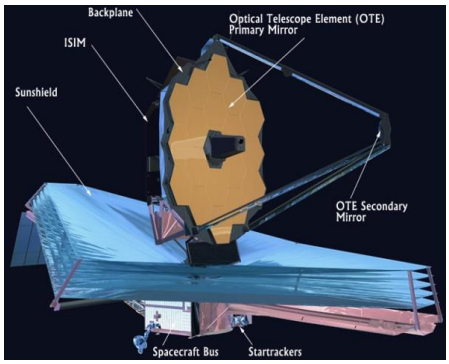

(b) 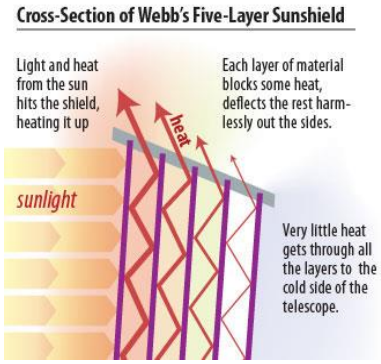

(c) 

Figure 1.3: (a) Schematically showing the different components of James Webb Space Telescope, where the telescope is kept isolated from the sun facing side by several sunshield layers; (b) Schematically showing the working of a sunshield [http://www.jwst.nasa.gov/sunshield.html]; (c) One-tenth scale model of NGST sunshield showing wrinkles [Johnston, 2002].

c. Sunshields

Next Generation Space Telescope (NGST) requires a lightweight, deployable sunshield subsystem, which separates the observatory into a warm sun-facing side and a cold anti-sun facing side. The James Webb Space Telescope is one of the examples of

such NGST's as shown in Figure 1.3a, which schematically shows the placement of a sunshield with respect to the telescope. The basic structure of a sunshield consists of multiple layers of pre-tensioned, thin-film membranes supported by deployable booms. With several layers of thin membranes, each layer blocks some sunlight, preventing it from reaching the anti-sun side, as schematically illustrated in Figure 1.3b.

When fully deployed, the sunshield is about the size of a regular tennis court. The structural behavior of the sunshield becomes a concern due to the telescope's strict line-of-site pointing requirements. Figure 1.3c shows a one-tenth scale model of a sunshield with wrinkles originating from the sheet corners. Due to the challenges involved in ground testing of the full-scale structure, the prediction and verification of sunshield dynamics is crucial to the development of this technology [Johnston, 2002].

1.2.2 Other Applications

Thin metal sheets are commonly used in the automobile industry. Different types of wrinkling patterns (stretch buckling, rolling buckling) have been observed in the long strips of sheet metal when they are conveyed through annealing lines (Fischer et al., 2000; Rammerstorfer et al., 2001; Fischer et al., 2003; Jacques et al., 2007). Figure 1.4 shows buckling in a metal strip near the roll as a result of stretch in the sheet. Permananet wrinkles are also observed during deep drawing process in sheet metals (Yu et al., 1982).

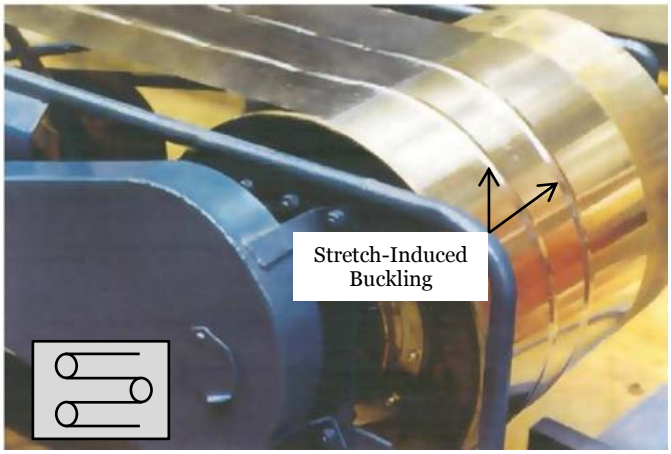

Figure 1.4: Formation of wrinkles in metal strip on a roll. The inset shows schematically the sheet conveying in the process lines [Jacques et al., 2007].

Thin sheets of glass panels are widely used in consumer electronics such as smartphones, tablets and TV screens. Figure 1.5a shows a schematic diagram of the process followed in manufacturing a glass sheet. The molten glass is first collected at the top and then allowed to take the form of a thin sheet as it emerges in a semi-solid state from the bottom of the collector which is also known as fusion-forming process. During this process, wrinkles are observed along the length of the glass sheet. Figure 1.5b shows an ultra slim flexible glass (Corning Willow Glass), which is 100 μm thick. With such a small thickness the probability of wrinkling increases and hence there is a need to carefully examine the cause of wrinkles and control them.

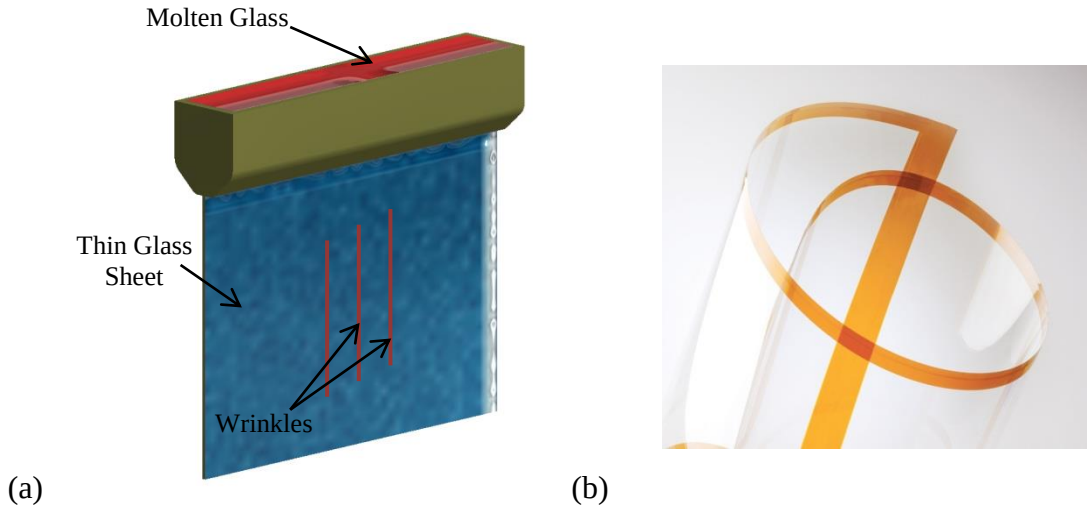

Figure 1.5: (a) Schematically showing the fusion-forming process used to manufacture glass in the form of thin sheets. Also schematically showing the direction of wrinkles that may occur during this process; (b) Ultrathin Corning Willow glass with thickness of 100 μm, which is the key reason for its flexibility [http://www.corning.com/CMS/Overview.aspx?id=48975].

In the applications discussed so far, wrinkles are undesirable and need to be suppressed. On the other hand, quantitative understanding of wrinkle patterns has been exploited as an effective method to measure mechanical properties of ultrathin sheets. Measuring these properties of an ultrathin film could be challenging. With precise measurement of wrinkles the elastic properties and thickness of the sheet can be determined as shown by Huang et al. (2007). In this study, property of PS sheet was studied by suspending the sheet on water surface and adding a drop of water on the sheet surface. Figure 1.6 shows a polystyrene (PS) film floating on water, which wrinkled due to the capillary forces exerted by the water drop, which is present on its surface. A scaling analysis similar to that by Cerda and Mahadevan (2003) was derived to relate the number of wrinkles and their length to the elastic properties and thickness of the film.

Furthermore, relaxation of the wrinkle pattern was observed which may be used to study the viscoelastic properties of polymer thin films. Moreover, wrinkling-based methods have been proposed for measuring mechanical properties of thin films on polymer substrates (Stafford et al., 2004; Chung et al., 2011).

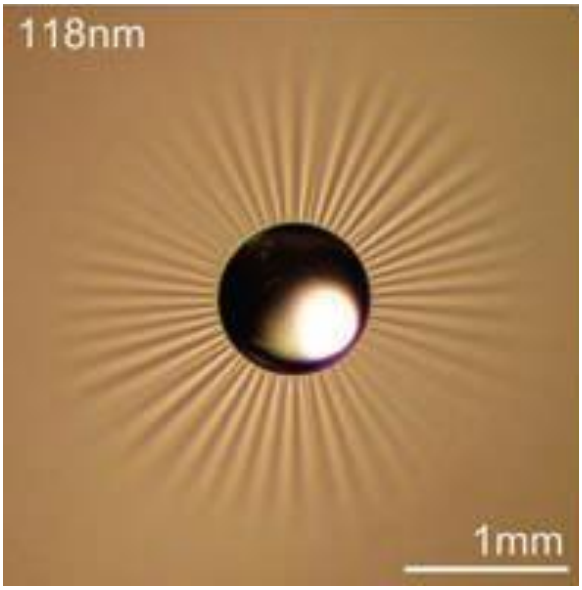

Figure 1.6: A polystyrene (PS) film floating on water surface and wrinkled due to a water drop with radius of 0.5 mm and mass of 0.2 mg on its upper surface [Huang et al., 2007].

Wrinkling of thin sheets has also been used to study cell activities such as cell locomotion (Burton et al., 1999) and cell division (Burton et al., 1997). Crawling cell locomotion involves protrusion at the leading edge, adhesion to the substratum, and retraction of the trailing edge. These movements require the cell to apply mechanical forces both internally and externally, which are too weak and are exerted over too small an area to be studied by conventional techniques. Similarly, during the cell division process, the applied forces by the cell change depending on the state of division. In such

cases, the applied forces range from nanonewtons to few hundred nanonewtons and its distribution is not well-defined as compared to the case of water droplet on a thin sheet as discussed earlier (Figure 1.6). It is quite challenging to solve this kind of wrinkling problem, but it was reported that traction forces can be made visible as elastic distortion and wrinkling of substratum (Harris et al., 1980), as shown in Figure 1.7, thus allowing estimation of forces. Through the shape, size and orientation of wrinkles in the substratum around the cell, the small traction force can be detected visibly.

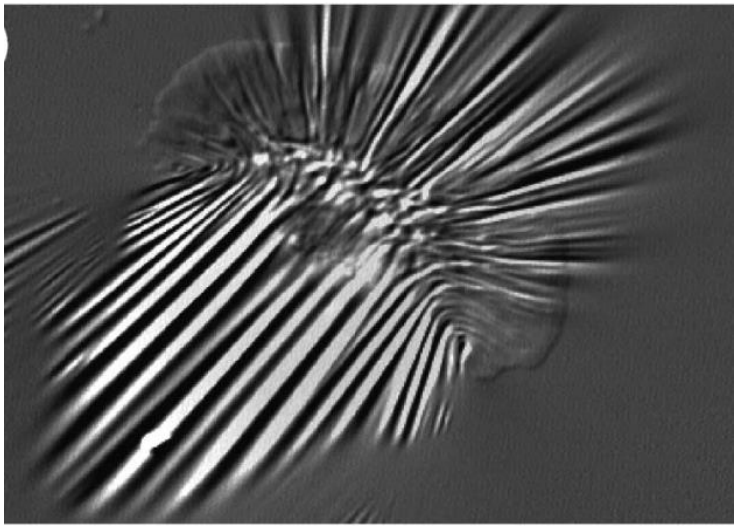

Figure 1.7: Formation of wrinkles in a Silicone sheet induced by cell traction forces [Burton et al., 1999].

1.3 PREVIOUS STUDIES AND MODEL PROBLEM

Two approaches have been commonly used for wrinkling analysis of elastic membranes: the tension field theory and the bifurcation analysis. In the tension field theory, the membrane is assumed to have zero bending stiffness. This approach was first applied by Wagner (1929) to estimate the maximum shear load that can be carried by a

thin web. Stein and Hedgepeth (1961) adopted this approach in analysis of partly wrinkled membranes, where a wrinkling region is assumed whenever one of the in-plane principal stresses becomes negative. Subsequently, the tension field theory has been continuously developed and extended for various applications (e.g., Mansfield, 1970; Danielson and Natarajan, 1975; Wu, 1978; Pipkin, 1986; Steigmann, 1990; Alder, et al., 2000; Liu et al., 2001; Coman, 2007). The tension field theory approach typically provides a satisfactory prediction of the stress distribution and wrinkling regions. However, it does not provide detailed information about the amplitude and wavelength of the wrinkles.

In the bifurcation analysis, the membrane is treated as a thin shell with non-zero bending stiffness. Typically, a geometrically nonlinear finite element method is employed using shell elements for numerical analysis (e.g., Tomita and Shindo, 1988; Friedl et al., 2000; Lee and Lee, 2002; Leifer and Belvin, 2003; Iwasa et al., 2004; Tessler et al., 2005; Wong and Pellegrino, 2006c; Diaby et al., 2006; Zheng, 2009). The critical condition for the onset of wrinkling and as well as the post-buckling behavior can be predicted by this approach. For relatively simple cases, analytical methods have also been proposed to obtain approximate solutions (Jacques and Potier-Ferry, 2005; Wong and Pellegrino, 2006b; Coman and Haughton, 2006; Steigmann, 2008; Puntel et al., 2011).

In the present study, we take the approach of bifurcation analysis and consider a model problem as shown in Figure 1.8: rectangular thin sheet is clamped at two ends and subjected to uniaxial stretching. Figure 1.8b shows an optical image of a stretched polyethylene sheet with wrinkles. During the course of this research, a literature review

found that numerous studies have been conducted on the same model problem. Segedin et al. (1988) solved for the critical conditions for onset of buckling with the described boundary conditions using a semi-analytical approach. Friedl et al. (2000) showed that compressive transverse stress is induced in the sheet under clamped-ends stretching specifically for length-to-width aspect ratios of 2 and 7. Jacques et al. (2005) presented an analytical solution to explain the wrinkle wavelength selection and mode localization in relatively long sheets. Cerda et al. (2002) presented the first experimental data for stretch-induced wrinkle wavelengths along with a scaling analysis, which predicted the wrinkle wavelength to decrease and amplitude to increase, with increasing longitudinal strain. Cerda and Mahadevan (2003) later extended the scaling analysis for a wide range of wrinkling phenomena. With a more elaborate analysis, Puntel et al. (2011) and Kim et al. (2012) confirmed the scaling relation for the wrinkle wavelength but showed that wrinkling occurs only beyond a critical strain, which depends on the length-to-width ratio of the rectangular sheet. Zheng (2009) presented both numerical analysis and experimental measurements of wrinkles in stretched rubber sheets showing that the wrinkle amplitude does not follow the prediction by the scaling analysis. Recently, Healey et al. (2012) further confirmed the non-monotonic change of wrinkle amplitude with increasing strain. In this study, the modified Föppl-von Kármán plate equations were solved numerically by taking into account finite membrane strains. Most of these studies have assumed linear elasticity for the materials, which are limited to relatively small strains. Moreover, experimental data is scarce especially for the wrinkle amplitude.

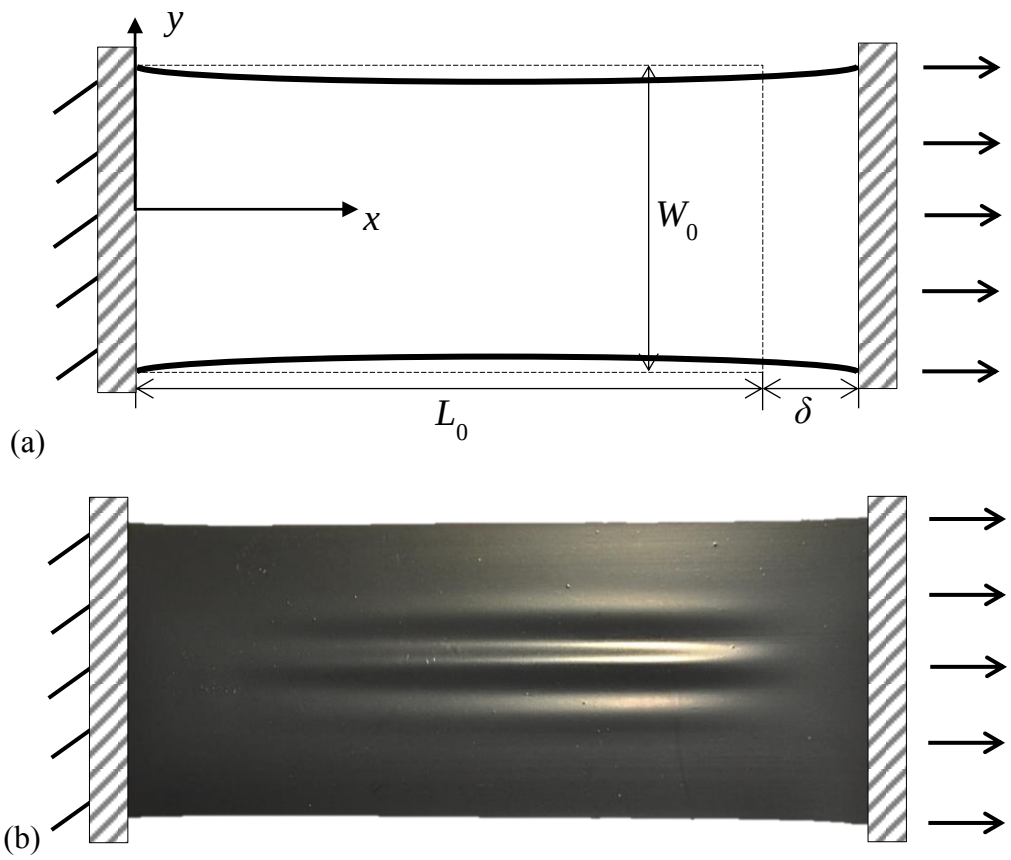

Figure 1.8: (a) Schematic illustration of a rectangular sheet with two clamped-ends, subject to uniaxial stretch; (b) An optical image of a wrinkled polyethylene sheet under stretch (ε ~ 10%).

1.4 DISSERTATION OUTLINE

In this dissertation, the model problem (Figure 1.8) is studied by both numerical simulations and experimental measurements. A finite element analysis using a commercial finite element package (ABAQUS) is carried out to analyze stresses and wrinkling instability of hyperelastic and hyper-viscoelastic thin sheets under clamped-

ends stretching. Experiments are conducted on polyethylene sheets and wrinkles are observed and measured using the 3D-Digital Image Correlation (3D-DIC) technique. Overall, the results from experiments and modeling are found to be in qualitative agreement. In addition, effects of different material models and material inhomogeneity on the wrinkling behavior are studied. Through this study, a comprehensive understanding of stretch-induced wrinkle formation in this particular boundary value problem is established. The dissertation is organized as follows.

In Chapter 2, stress distributions in hyperelastic thin sheets under clamped-ends stretching are studied using 2-D finite element models, assuming no wrinkles. It is found that, with the specific boundary conditions, compressive stresses develop in the transverse direction upon stretching, which is the necessary condition for wrinkling. The magnitude and distribution of the compressive stress depend on the applied nominal strain and the length-to-width aspect ratio of the sheet. A phase diagram is constructed with four different distribution patterns of the stretch-induced compressive stresses, spanning a wide range of aspect ratio and nominal strain.

In Chapter 3, an eigenvalue analysis is performed to determine the critical condition for onset of stretch-induced wrinkling in hyperelastic thin sheets, followed by a nonlinear post-buckling analysis to simulate evolution of stretch-induced wrinkles. It is found that the wrinkle wavelength decreases with increasing strain, in good agreement with the prediction by a scaling analysis. However, as the tensile strain increases, the wrinkle amplitude first increases and then decreases, eventually to zero beyond a moderately large nominal strain.

Chapter 4 presents an experimental study using polyethylene sheets stretched under the clamped-ends condition. A three-dimensional digital image correlation (3D-DIC) technique was used to measure wrinkling deformation. It was observed that the wrinkle amplitude first increased and then decreased with increasing nominal strain, in agreement with finite element simulations for a hyperelastic thin sheet. However, unlike the hyperelastic model, the stretch-induced wrinkles in the polyethylene sheet were not fully flattened at large strains (> 30%), with the residual wrinkle amplitude depending on the loading rate.

In Chapter 5, a hyper-viscoelastic and a parallel network nonlinear viscoelastic material model was adopted for finite element simulations to improve the agreement with the experiments, including the wrinkle amplitude, residual wrinkles and rate dependence. It is found that the effect of viscoelasticity on stretch-induced wrinkling is most observable for the wrinkle amplitude at intermediate strain rates. The wrinkle wavelength, on the other hand, is insensitive to the specific material models for the thin sheet.

In Chapter 6, effect of material inhomogeneity on wrinkling is studied by assuming a different elastic modulus in a narrow modified region of the hyperelastic sheet. It is found that the critical strain for onset of wrinkling decreases sharply, for both stiffer and softer modified regions. Different wrinkling patterns are predicted for the inhomogeneous sheet. Remarkably, in presence of the material inhomogeneity, the number of wrinkles increases with increasing nominal strain, and the wrinkle amplitude remains nonzero up to very large strains.

Finally, Chapter 7 concludes the present study with a summary and discusses potential topics for future studies.

CHAPTER 2

Hyperelastic Stress Analysis

2.1 INTRODUCTION

In this chapter we study the stresses that develop in hyperelastic thin sheets when subject to clamped-ends stretching, focusing particularly on the compressive stress that might lead to wrinkling. The stresses under clamped-ends stretching are studied using a two-dimensional (2D) plane-stress model in ABAQUS. This is adequate for the study of stretch-induced stress distributions without wrinkling. A necessary condition for onset of wrinkling is the development of compressive stresses in the sheet, although the primary loading is tension. Figure 1.8a shows a schematic diagram of a rectangular sheet clamped at two opposite ends. Before stretching, the dimensions of the sheet are: length L_0, width W_0, and thickness t_0. The nominal strain is defined as, $\varepsilon = \delta/L_0$, where $\delta = L - L_0$ is the end displacement. Due to the constraint applied by the clamped ends, the deformation and stresses in the sheet are inhomogeneous. The sheet is modeled using quadrilateral plane-stress elements, specifically CPS4R in ABAQUS. A uniform mesh is used with 100 square-shaped elements across the width of the sheet, which is found sufficient to achieve convergence in the 2-D stress analysis. However, the mesh is not adequate to resolve the singular stresses at the corners of the sheet, which is not important for the present study. The geometry of the rectangular sheet is characterized by a single dimensionless ratio between the length and the width, $\alpha = L_0/W_0$. The thickness of the sheet has no effect on the 2-D stress analysis, but will be important for the wrinkling

analysis (Chapter 3). The material of the sheet is assumed to be hyperelastic so that moderately large deformations can be considered. Using the incompressible neo-Hookean material model, the only material property to be specified is the initial shear modulus (μ). With incompressibility, neo-Hookean strain energy function can be written as,

$$W = \frac{\mu}{2}(I_1 - 3) \tag{2.1}$$

where, I_1 is a principal invariant that can be written as,

$$I_1 = \lambda_1^2 + \lambda_2^2 + \lambda_3^2 \tag{2.2}$$

λ_1, λ_2 and λ_3 are the principal stretches. Under uniaxial loading conditions, Cauchy stress $\left(\sigma = \lambda\frac{\partial W}{\partial \lambda}\right)$ for an incompressible neo-Hookean solid becomes,

$$\sigma = \mu\left(\lambda^2 - \frac{1}{\lambda}\right) \tag{2.3}$$

To be specific, we set μ = 6 MPa, a representative value for rubberlike materials. In addition to the nonlinear elasticity of the material, the nonlinear kinematics for finite deformation is taken into account in the finite element analysis. To understand the effect of the aspect ratio ($\alpha = L_0/W_0$), we vary the initial length (L_0) of the sheet while keeping the width constant (W_0 = 100 mm, to be specific) in all models. For each aspect ratio, the sheet is increasingly stretched up to a moderately large nominal strain ($\varepsilon \leq 150\%$). In the following sections, different stress components and their distributions under increasing nominal strain are discussed (Nayyar et al., 2011).

2.2 TRANSVERSE STRESS

It is found that for a wide range of aspect ratios, compressive stress is induced in the transverse direction of the sheet (i.e., $\sigma_y < 0$). In addition, different distribution

patterns of the stretch-induced compressive stress are found, depending on the aspect ratio (α) and the applied stretch.

Figure 2.1 summarizes the results in a phase diagram for the stress patterns, including four different phases: (I) all-tension phase (see Figure 2.2); (II) transverse two-peak phase (see Figures 2.3 and 2.4); (III) central one-peak phase (see Figure 2.5); (IV) longitudinal two-peak phase (see Figures 2.6 and 2.7). The details are discussed in the following sections.

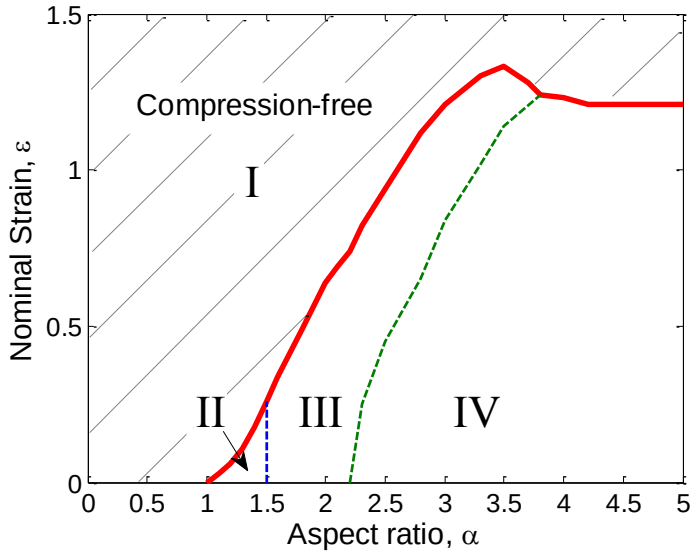

Figure 2.1: A phase diagram for stretch-induced compressive stress patterns in end-clamped rectangular sheets.

2.2.1 Case 1: low aspect ratio ($\alpha \leq 1$)

For rectangular sheets with low aspect ratios ($\alpha \leq 1$), no compressive stress is induced under clamped-ends stretching. Figure 2.2 shows the stress contour (σ_y) for a sheet with $\alpha = 1$ and $\varepsilon = 1\%$, where the stress magnitude is normalized by Young's

modulus of the material ($E = 3\mu$). The entire sheet is under tension in both the x and y directions; consequently, no wrinkling is expected in this case. We note that the resolution of the singular stress field at the corners (Benthem, 1963) may require use of a very fine mesh or singular elements in the finite element model. However, for the discussion of stretch-induced wrinkling, only the stress distribution away from the corners is of importance and thus a moderately fine mesh is sufficient. Due to the constraint of uniaxial strain at the clamped ends (i.e., zero strain in the y-direction), a biaxial tensile stress field develops near the ends. However, due to the two free edges at $y/W_0 = \pm 0.5$, the tensile stress in the y direction is partially relaxed in the center region of the sheet, but remains tensile everywhere for the low-aspect-ratio sheet. Figure 2.2b shows the transverse stress σ_y along the vertical center line of the sheet ($x/L_0 = 0.5$). The stress σ_y is necessarily zero at the edge ($y/W_0 = \pm 0.5$) by the boundary condition. Away from the edges, σ_y increases and reaches a peak at the center of the sheet ($y = 0$). As the nominal strain increases, the magnitude of the tensile transverse stress increases. Therefore, regardless of the applied stretch, the stress field is completely tensile for the low-aspect-ratio sheets; this is designated as Phase I in Figure 2.1.

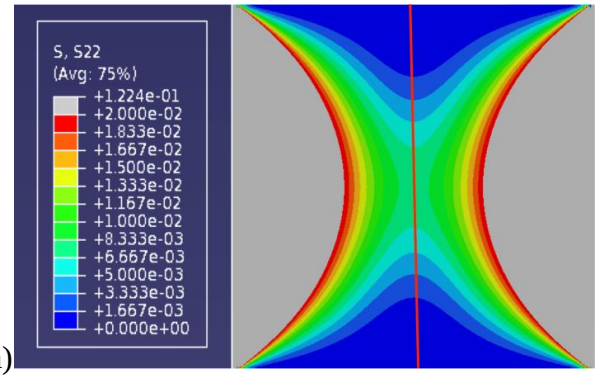

(a)

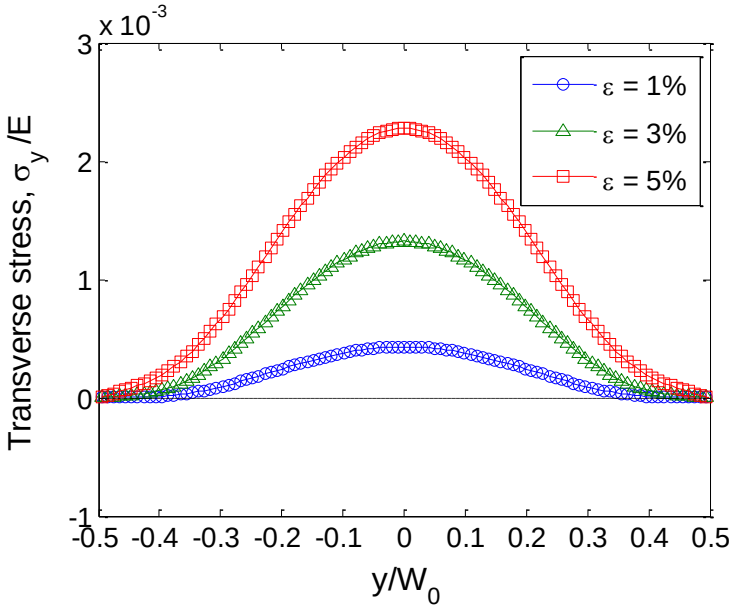

(b)

Figure 2.2: (a) Contour plots of the stretch-induced transverse stress (σ_y) for α = 1 and ε = 1%, showing no compressive stress; (b) Distribution of the transverse stress along the vertical center line of the sheet under different strains.

2.2.2 Case 2: $1 < \alpha < 1.5$

With the aspect ratio slightly greater than 1, a compressive stress is induced in the rectangular sheet upon stretching. As shown in Figure 2.3 for α = 1.1 and ε = 1%, the stress σ_y is negative in two separate regions symmetrically located near the free edges,

with two peak compressive stresses on the vertical center line. As shown in Figure 2.3b, at ε = 1% the transverse stress along the center line is compressive near the edges and tensile at the center. As the applied strain increases, the magnitude of the compressive stress first increases and then decreases, becoming all tensile at ε = 5%. Therefore, for such an aspect ratio, a two-peak compressive stress pattern is induced at small strains; this is designated as Phase II in Figure 2.1. A transition from Phase II to Phase I (all-tension) occurs at a critical strain that increases with the aspect ratio.

For aspect ratios up to 1.5, the distribution of the stretch-induced compressive stress exhibits a similar pattern, with two peaks along the vertical center line of the sheet. As the aspect ratio increases, locations of the two peaks move toward the center. Meanwhile, the two regions of the compressive stress expand and eventually merge into one region from edge to edge, as shown in Figure 2.4a for α = 1.35 and ε = 1%. With increasing stretch, the magnitude of the compressive stress first increases (Figure 2.4b) and then decreases (Figure 2.4c), becoming all tension at ε = 15%.

The boundary between Phase I and Phase II in Figure 2.1 is determined approximately from the finite element analysis. First, the critical aspect ratio between the two phases is found to be around 1. Second, for $1 < \alpha < 1.5$, the critical strain for the transition from Phase II to Phase I is calculated as a function of the aspect ratio. At α = 1.5, it is found that the two peaks of the compressive stress merge into one at the center of the sheet ($y = 0$ and $x/L_0 = 0.5$); this is designated as Phase III in Figure 2.1.

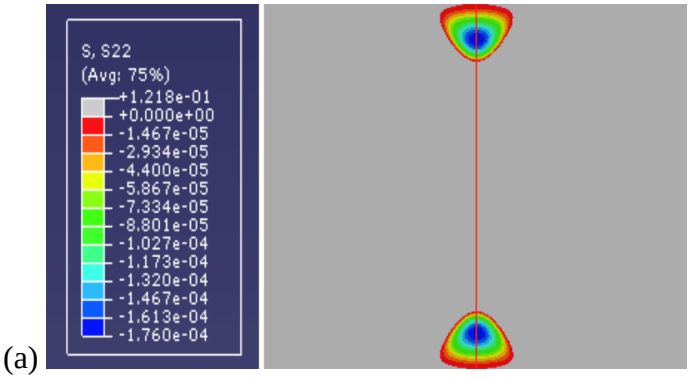

(a)

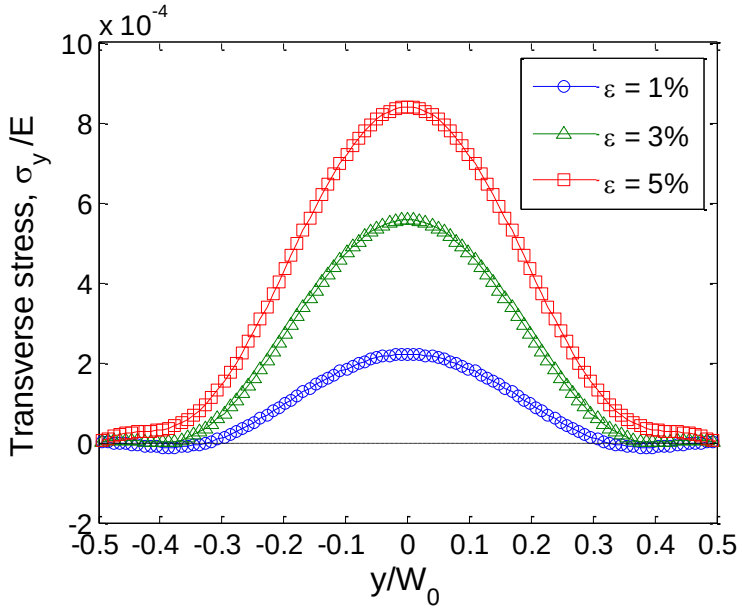

(b)

Figure 2.3: (a) Contour plots of stretch-induced transverse stress (σ_y) for α = 1.1 and ε = 1%, showing the compressive stress in two separate regions; (b) Distribution of the transverse stress along the vertical center line of the sheet under different strains.

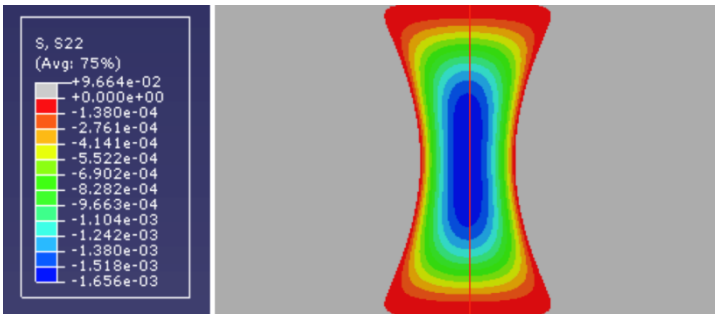

(a)

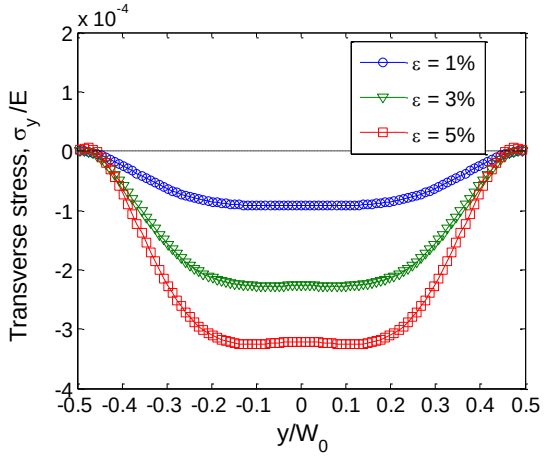

(b)

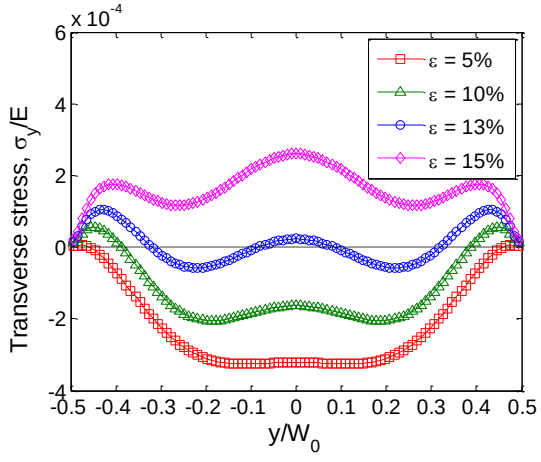

(c)

Figure 2.4: (a) Contour plots of stretch-induced transverse stress (σ_y) for α = 1.35 and ε = 1%, showing only the compressive stress region; (b) and (c) Distributions of the transverse stress along the vertical center line of the sheet under increasing nominal strains.

2.2.3 Case 3: $1.5 \leq \alpha < 2.2$

For $1.5 \leq \alpha < 2.2$, a region of compressive stress develops at the center of the rectangular sheet upon stretching, with the peak compressive stress at the center of symmetry ($y = 0$ and $x/L_0 = 0.5$), as shown in Figure 2.5a for $\alpha = 2$ and $\varepsilon = 1\%$. The one-peak distribution pattern is designated as Phase III in Figure 2.1. Friedl et al. (2000) showed a similar stress pattern for a linear elastic sheet with $\alpha = 2$. Along the vertical center line of the sheet, the stress σ_y is compressive from edge to edge for $\varepsilon < 20\%$. The magnitude of the peak compressive stress first increases as the applied stretch increases up to $\varepsilon = 20\%$, as shown in Figure 2.5b. As the applied stretch increases further, the stress becomes tensile near the edges and the magnitude of the peak compressive stress at the center decreases (Figure 2.5c). Eventually at $\varepsilon = 64\%$, the stress becomes all tension (Phase I) again. Similar to the transition from Phase II to Phase I, the critical strain for the transition from Phase III to Phase I increases as the aspect ratio increases, which defines the boundary between Phase III and Phase I in Figure 2.1.

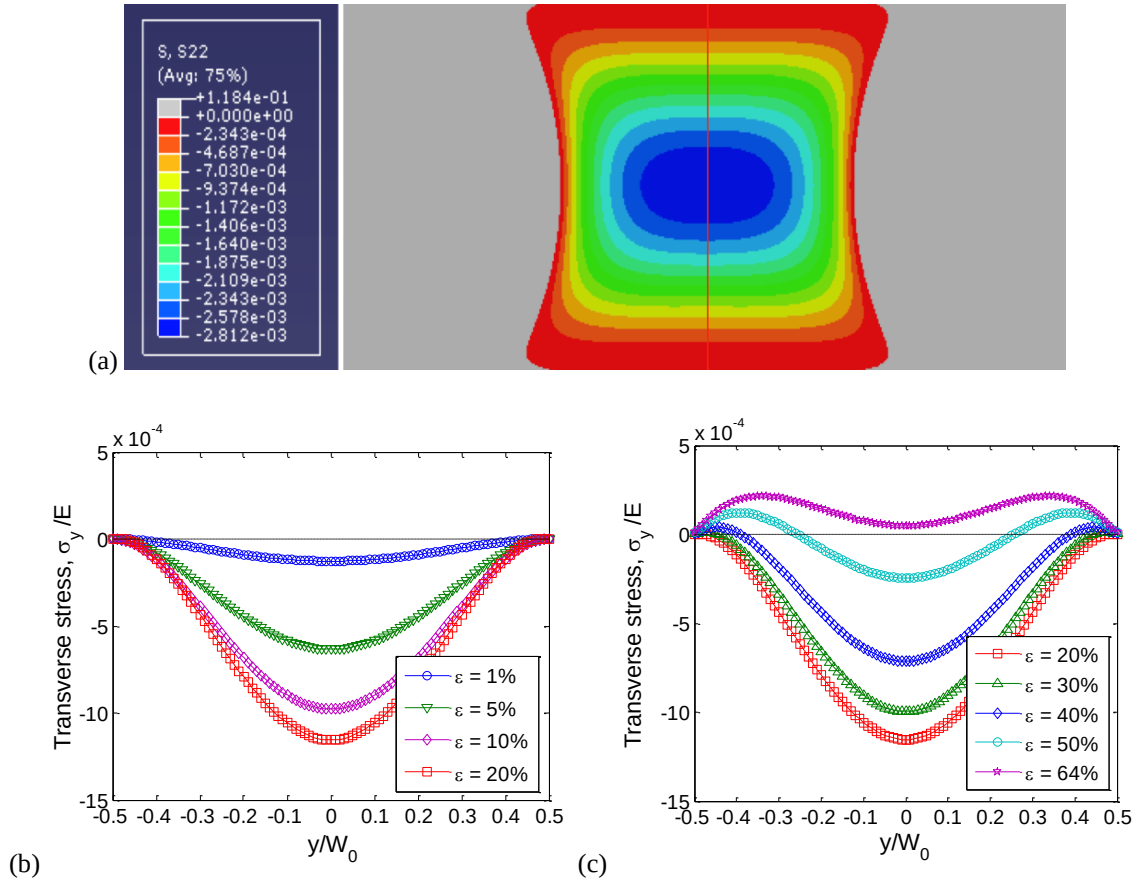

Figure 2.5: (a) Contour plots of stretch-induced transverse stress (σ_y) for α = 2 and ε = 1%, showing only the compressive stress region; (b) and (c) Distributions of the transverse stress along the vertical center line of the sheet under increasing nominal strains.

2.2.4 Case 4: $2.2 \leq \alpha < 3.7$

As the aspect ratio continues to increase, the region of the stretch-induced compressive stress expands in the x direction. When $\alpha \geq 2.2$, the peak compressive stress at the center splits into two peaks symmetrically located on the x-axis, as shown in Figure 2.6a for α = 2.5 and ε = 1%. The longitudinal two-peak distribution of the stretch-induced compressive stress is designated as Phase IV in Figure 2.1. Figure 2.6b shows the

transverse stress (σ_y) along the x-axis (horizontal center line of the sheet) for α = 2.5. The stress is tensile near the clamped ends, but becomes compressive approaching the center of the sheet. The magnitude of the peak compressive stress increases with increasing stretch up to ε = 20%. Further increasing the stretch, the magnitude of the peak compressive stress decreases, as shown in Figure 2.6c. Meanwhile, the location of the peak compressive stress moves towards the center as the stretch increases. At ε = 60%, the two peaks merge into one at the center of the sheet. Therefore, the distribution pattern of the stretch-induced compressive stress changes from Phase IV to Phase III. As shown in Figure 2.1, the critical strain for this transition increases with the aspect ratio for $2.2 \leq \alpha < 3.7$. As the applied stretch continues to increase, a transition from Phase III to Phase I (all-tension) occurs, similar to that shown in Figure 2.5 for Case 3.

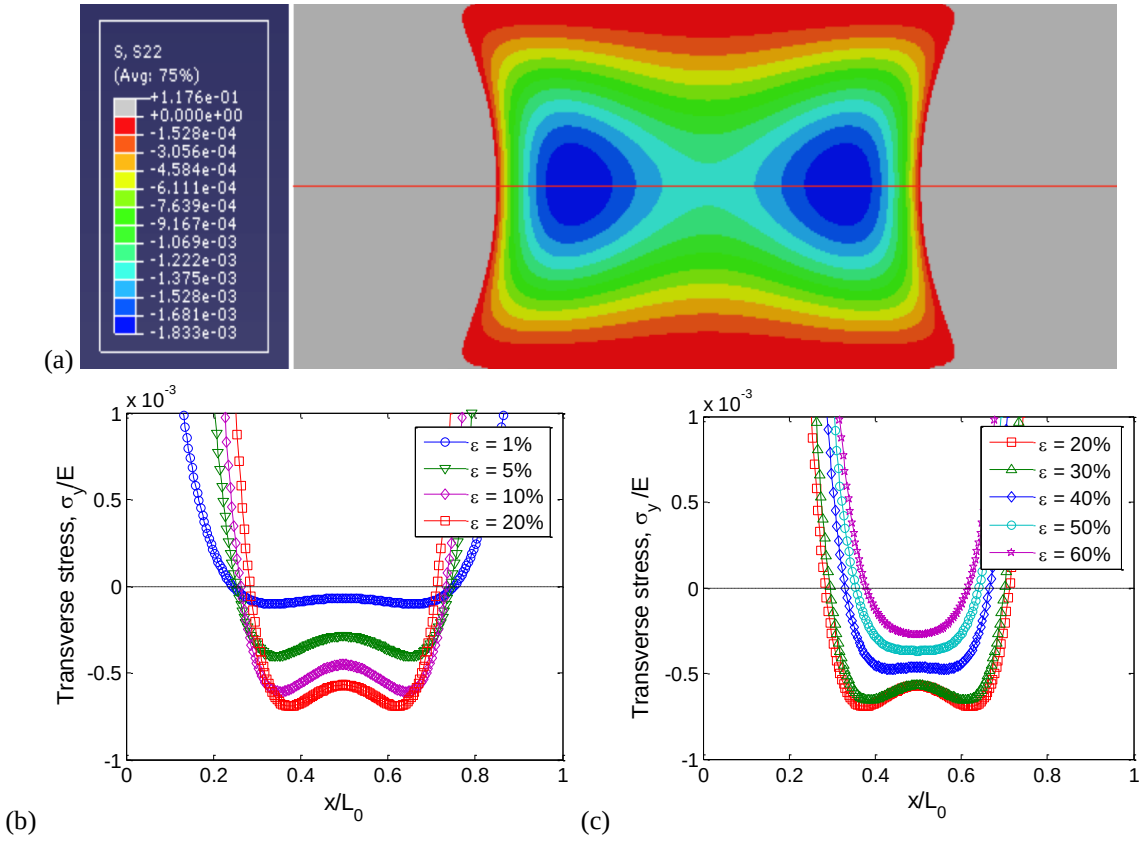

Figure 2.6: (a) Contour plots of stretch-induced transverse stress (σ_y) for α = 2.5 and ε = 1%, showing only the compressive stress region; (b) and (c) Distributions of the transverse stress along the horizontal center line of the sheet under increasing nominal strains.

2.2.5 Case 5: high aspect ratio ($\alpha \geq 3.7$)

For rectangular sheets with the length-to-width aspect ratio greater than 3.7, the stretch-induced compressive stress has two peaks symmetrically located on the *x*-axis (Phase IV) when the applied stretch is less than a critical strain. Beyond the critical strain, the stress distribution becomes all tension (Phase I). Unlike in Case 4, the stress pattern transitions directly from Phase IV to Phase I, without going through Phase III. As shown in Figure 2.1, the critical strain for this transition is nearly independent of the aspect ratio.

With a high aspect ratio, the two peaks of the compressive stress are located far apart from each other, and the region of compressive stress is split into two separate regions, with nearly zero σ_y at the center region of the sheet, as shown in Figure 2.7a for α = 5 and ε = 1%. Thus, the stretch-induced compressive stress is localized near the clamped ends. In between, the stress state is essentially uniaxial. Indeed, at the limiting case with $\alpha >> 1$, it is expected that most part of the sheet is under uniaxial tension with a uniform stress distribution ($\sigma_y = 0$ and $\sigma_x > 0$) except for the regions near the clamped ends. A similar stress pattern was predicted by Friedl et al. (2000) for α = 7 and by Benthem (1963) for a semi-infinite strip, both assuming linear elastic properties of the material. As the applied stretch increases, the locations of the peak compressive stress move towards the center of the sheet, but remain separated. The magnitude of the peak compressive stress first increases (Figure 2.7b) and then decreases (Figure 2.7c). Eventually, with the nominal strain beyond 130%, the stress distribution becomes all tension (Phase I). Since the two regions of compressive stress are separate with negligible interaction, the behavior becomes independent of the length (L_0) for the rectangular sheets with high aspect ratios.

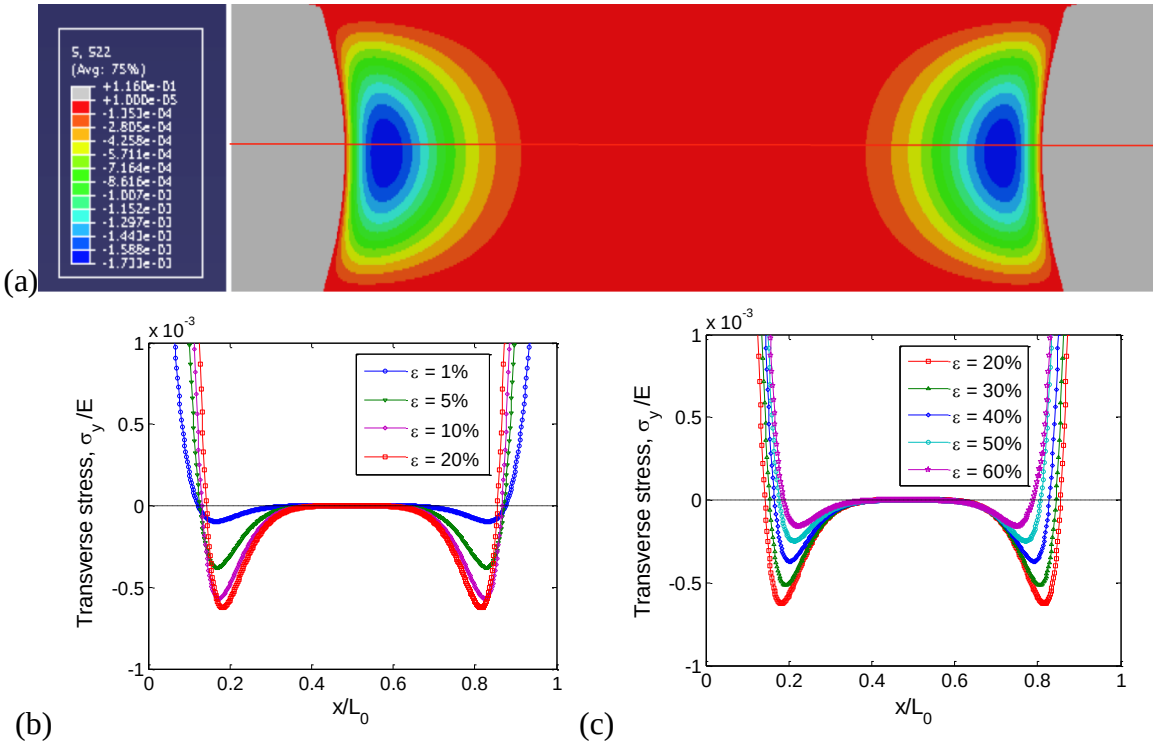

Figure 2.7: (a) Contour plots of stretch-induced transverse stress (σ_y) for α = 5 and ε = 1%, showing only the compressive stress region; (b) and (c) Distributions of the transverse stress along the horizontal center line of the sheet under increasing nominal strains.

To summarize the 2-D stress analyses, we plot in Figure 2.8a the magnitude of the peak compressive stress as a function of the nominal strain for the rectangular sheets with four different aspect ratios. For all cases with $\alpha > 1$, the magnitude of the peak compressive stress first increases with the nominal strain and then decreases, with a maximum magnitude at an intermediate strain. The maximum magnitude of the peak compressive stress increases with the aspect ratio for $1 < \alpha < 1.8$, but decreases for $\alpha > 1.8$, as shown in Figure 2.8b. It may be understood that the magnitude of the peak compressive stress increases as the two peaks on the vertical center line (Phase II) merge

into one (Phase III) and decreases as the peak split into two on the horizontal center line (Phase IV). In the case of high aspect ratios ($\alpha > 3.7$), the peak compressive stress and its dependence on the nominal strain becomes essentially independent of the aspect ratio; this can be understood to be the result of separation of the two regions with localized compressive stress near the clamped ends. As shown in Figure 2.1, the critical strain for the sheet to become all tension (Phase I) increases with the aspect ratio, with a small overshoot before it saturates at a constant strain (~130%) for high aspect ratios ($\alpha \geq 4$). As discussed above, several types of phase transition for the distribution patterns of stretch-induced compressive stress (σ_y) can be observed in the diagram (Figure 2.1), including II-to-I, III-to-I, IV-to-III, and IV-to-I.

We close this section by noting two necessary conditions to have stretch-induced compressive stress in the rectangular sheets. The first condition is the coupling between the longitudinal and transverse deformation, and the second is the constraint due to the clamped ends. In the present study, the longitudinal-transverse coupling arises from the incompressibility of the hyperelastic material model. Similar results were obtained by Friedl et al. (2000) using a linear elastic material model with Poisson's ratio $v = 0.3$. On the other hand, if $v = 0$, no compressive stress would be induced, regardless of the aspect ratio or the applied strain and hence, no wrinkles would form in the stretched sheet. Alternatively, if the constraint at the clamped ends is relaxed (e.g., allowing end displacement in the transverse direction), a uniaxial tensile stress in the longitudinal direction would be expected with zero transverse stress and hence no wrinkles either.

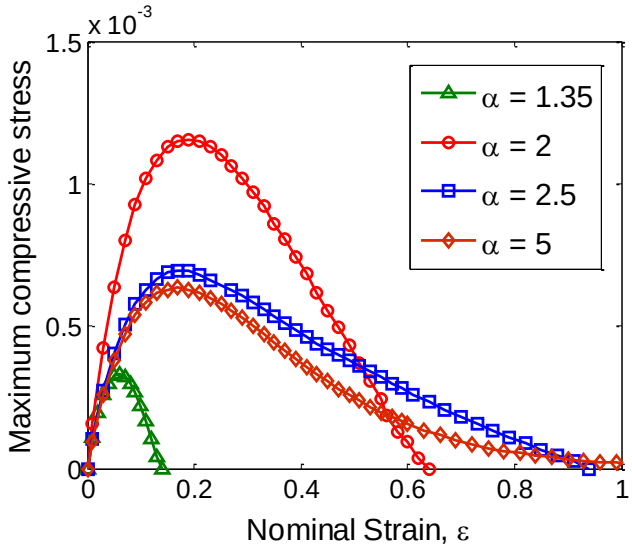

(a)

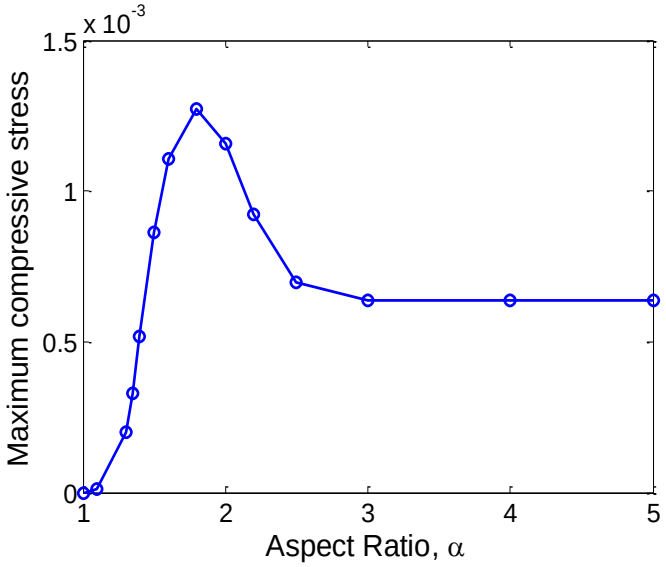

(b)

Figure 2.8: (a) Variation of the maximum compressive stress magnitude in the rectangular sheets under increasing stretch for different aspect ratios; (b) Maximum magnitude of the stretch-induced compressive stress as a function of the aspect ratio.

2.3 SUMMARY

In this chapter, a 2-D stress analysis was performed on hyperelastic sheets under clamped-ends stretching. It was found that because of the clamped-ends and Poisson's effect, the transverse compressive stress may develop in the sheet upon stretching, depending on the in-plane aspect ratio (α). It was found that with aspect ratios, $\alpha < 1$, transverse compression is absent. While for relatively large aspect ratios, $\alpha > 1$, in-plane transverse compression is present only in specific regions of the sheet, depending on both the sheet aspect ratio and the applied nominal strain. Qualitatively, for all aspect ratios that show transverse compression under clamped-ends stretching, magnitude of the compressive stress changes non-monotonically with the applied strain. The transverse compressive stress, which is independent of sheet thickness, becomes zero at a critical nominal strain. This critical strain for compression-free state is dependent only on the sheet aspect ratio. The critical conditions for wrinkling and post-buckling behavior are studied next in Chapter 3.

CHAPTER 3

Hyperelastic Wrinkling Analysis

3.1 INTRODUCTION

Based on the 2D stress analysis in Chapter 2, it is clear that compressive stresses may occur in the sheet in the transverse direction when stretched with clamped-ends. This is a necessary condition for sheet buckling, but formation of wrinkles is not assured; In this Chapter, the focus is on investigating the critical conditions for sheet wrinkling through numerical simulations. For such a thin sheet, the shell elements (S4R) in ABAQUS are used in the finite element analyses to allow three-dimensional deformation of the sheet. A uniform mesh similar to that used for the 2-D stress analyses (Chapter 2) is used in the 3-D buckling analyses. It is confirmed that if the out-of-plane displacement is suppressed numerically, then the finite element model with the shell elements reproduces correctly the stress patterns obtained from the 2-D model with the plane-stress elements. An eigenvalue buckling analysis is performed to identify the critical condition for the onset of wrinkling first and is then followed by a post-buckling analysis (Nayyar et al., 2011). An incompressible Neo-Hookean model is assumed for the sheet material. The effects of sheet geometry and its material properties on wrinkling are discussed. It is found that wrinkle formation is closely related to the transverse compressive stress patterns. The results obtained from the wrinkling analysis are compared with the scaling analysis by Cerda and Mahadevan (2003).

The model problem of stretch-induced wrinkling was considered by Cerda and Mahadevan (2003), who derived the scaling relations for the wrinkle wavelength and amplitude based on an analytical approximation of energy minimization. In their analysis, the total energy functional was written in the form

$$U = U_B + U_S - \Theta \tag{3.1}$$

where U_B is the bending energy, U_S is the stretching energy, and Θ imposes a geometrical constraint assuming inextensibility of the sheet in the transverse direction. The condition of inextensibility is commonly used in membrane analysis, but questionable for the present problem. Assuming a compressive displacement Δ in the transverse direction of the sheet, the inextensibility condition is

$$\int \left(\frac{1}{2} \left(\frac{\partial u_z}{\partial y} \right)^2 - \frac{\Delta}{W} \right) dy = 0 \tag{3.2}$$

We notice a possible error in the paper by Cerda and Mahadevan (2003), where the limits of the integral were taken in the longitudinal direction but should be taken in the transverse direction with respect to *y*. To impose the constraint everywhere in the sheet, a Lagrange multiplier $b(x)$ was used in the last term of the energy functional, namely

$$\Theta = \int_A \left(\frac{1}{2} \left(\frac{\partial u_z}{\partial y} \right)^2 - \frac{\Delta}{W} \right) b(x) dA \tag{3.3}$$

Moreover, in their expressions for the bending and stretching energy terms, Cerda and Mahadevan (2003) ignored the contributions from the bending curvature in the x-direction and the stretching in the y-direction so that

$$U_B = \frac{D}{2}\int_A \left(\frac{\partial^2 u_z}{\partial y^2}\right)^2 dA \tag{3.4}$$

$$U_S = \frac{1}{2}\int_A T(x)\left(\frac{\partial u_z}{\partial x}\right)^2 dA \tag{3.5}$$

where $D = Et^3/\left[12(1-\nu^2)\right]$ is the flexural rigidity of the sheet and $T(x)$ is the tension in the x-direction. The assumption that the tension is independent of y is again questionable. As shown by the stress analysis in Chapter 2, the stress distribution is highly non-uniform in both the x and y directions, especially near the clamped ends, where the tension is biaxial.

To minimize the energy functional in Eq. (3.1), the first variation of the functional with respect to the out-of-plane displacement (u_z) vanishes; this leads to an equilibrium equation

$$D\frac{\partial^4 u_z}{\partial y^4} - T(x)\frac{\partial^2 u_z}{\partial x^2} + b(x)\frac{\partial^2 u_z}{\partial y^2} = 0 \tag{3.6}$$

Eq. (3.6) appears to be a modified plate equation, which has selectively ignored several terms and added an additional term via the transverse inextensibility condition.

To solve Eq. (3.6) analytically, additional approximations were made by Cerda and Mahadevan (2003): (1) the tension was taken to be a constant in the sheet, $T(x) \approx Et\varepsilon$; (2) the compressive displacement Δ in the transverse direction was taken to be a constant, $\Delta \approx \nu\varepsilon W$, so that the Lagrange multiplier $b(x)$ became a constant too. As a result, Eq. (3.1) can be solved in form of a series expansion

$$u_z(x,y) = \sum_n A_n \sin(\omega_n x)\exp(ik_n y) \tag{3.7}$$

where $\omega_n^2 = \left(bk_n^2 - Dk_n^4\right)/T$. The boundary condition, e.g., $u_z = 0$ at both ends of the sheet (x = 0 and L), requires that $\omega_n = \pi / L$ (the first buckling mode only). Thus, the Lagrange multiplier is $b = \pi^2 T/(k_n^2 L^2) + Dk_n^2$ for each mode with wrinkle wavelength, $\lambda_n = 2\pi / k_n$. Then, by inserting (3.7) into Eq. (3.2) for transverse inextensibility and taking x = L/2 only, it leads to $A_n \approx \left(\Delta / W\right)^{1/2} \lambda_n / \pi$, which was taken as a general relationship between the wrinkle amplitude and wrinkle wavelength. With these approximations, the energy functional in Eq. (3.1) can be written as a function of the wrinkle wavelength for each mode

$$U = 2\pi^2 DL\Delta\lambda^{-2} + \frac{\lambda^2}{8} T\Delta / L \tag{3.8}$$

where the last term in Eq. (3.1) is zero by assuming $b(x)$ to be a constant.

Finally, the wrinkle wavelength is predicted by minimizing the energy in Eq. (3.8), leading to

$$\lambda = \left(16\pi^2 DL^2 / T\right)^{1/4} \tag{3.9}$$

With $T \approx Et\varepsilon$ and $\Delta \approx \nu\varepsilon W$, the wavelength and amplitude of stretch-induced wrinkles are predicted as

$$\lambda = \left(\frac{4\pi^2}{3(1-\nu^2)}\right)^{1/4} \left(Lt\right)^{1/2} \varepsilon^{-1/4} \tag{3.10}$$

$$A = \left(\frac{4}{3\pi^2(1-\nu^2)}\right)^{1/4} \left(\nu Lt\right)^{1/2} \varepsilon^{1/4} \tag{3.11}$$

Despite many assumptions in this analysis, the prediction for the wrinkle wavelength, Eq. (3.10), was found to be in close agreement with experimental measurements in polyethylene sheets (Cerda et al., 2002). However, the prediction for the wrinkle amplitude has not been validated by experiments.

Recently, Puntel et al. (2011) presented a more elaborate analysis on the same problem, which predicted modulated wrinkle profiles similar to the numerical results and experimental observations. In addition, their analysis predicted that the number of wrinkles increases with increasing stretch, which however has not been observed in experiments. More recently, Healey et al. (2013) presented a semi-analytical approach for wrinkling of highly stretched, thin rectangular sheets. Like most other studies, the material of the sheet was assumed to be linear elastic. They modified the nonlinear Föppl-von Kármán equations of elastic plates to correctly account for large in-plane strain prior to wrinkling. A numerical bifurcation analysis was then performed. Their results compare closely with the numerical results presented in this chapter, with quantitative differences likely due to the nonlinear elastic material properties assumed in the present study.

3.2 EIGENVALUE BUCKLING ANALYSIS

To determine the critical strain for a clamped sheet to undergo buckling under stretching, a buckling eigenvalue analysis is performed. In addition to the length-to-width (α) aspect ratio, the thickness (t_0) of the sheet becomes critical for both eigenvalue and post-buckling analyses. In the present study, we take the initial width-to-thickness ratio ($\beta = W_0/t_0$) of the sheet to be at least 1000. To obtain the relevant eigenmodes and the eigen

values for stretch-induced buckling, a small pre-stretch of ~1% is applied in the longitudinal direction before the eigenvalue analysis. With β = 1000 and the length-to-width aspect ratio α < 1.35, no buckling mode with positive eigenvalues can be found under the prescribed boundary conditions. While the stretch-induced compressive stress is present for 1 < α < 1.35, the magnitude of the compressive stress is low and it is distributed in two small regions as shown in Figure 2.3a for α = 1.1. For $\alpha \geq 1.35$, a number of eigenmodes are obtained for the pre-stretched sheet. Figure 3.1 shows the first eigenmode for four different in-plane aspect ratios with β = 1000. We note the correlation between the buckling mode shapes and the compressive stress patterns shown in Chapter 2 (Figures 2-4, 2-5, 2-6, and 2-7). In particular, the transition of the compressive stress pattern from Phase II to III and eventually to IV with increasing aspect ratio is faithfully replicated in the eigenmodes. For α = 2.5, however, the eigenmode shows apparently a single peak at the center of the sheet (Figure 3.1c), while the compressive stress has two peaks along the longitudinal axis (Figure 2.6). This may be attributed to the close proximity of two peaks in the compressive stress distribution. When the two peaks are sufficiently separated, the eigenmode shows two peaks as well with a relatively flat region in between, as shown in Figure 3.1d for α = 5.

(a)

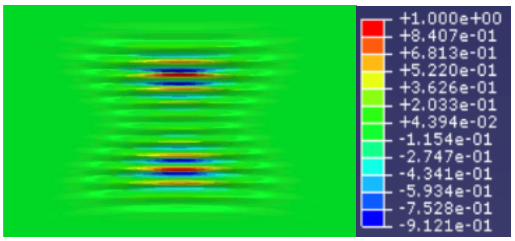

(b)

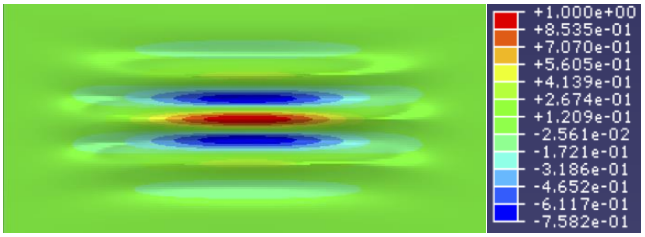

(c)

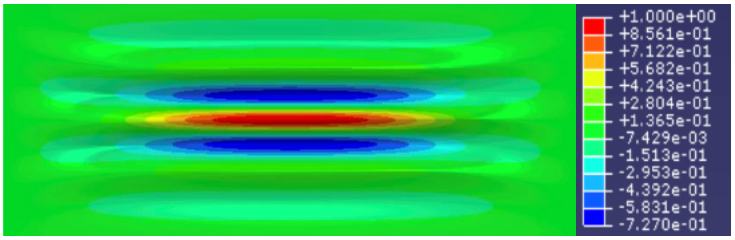

(d)

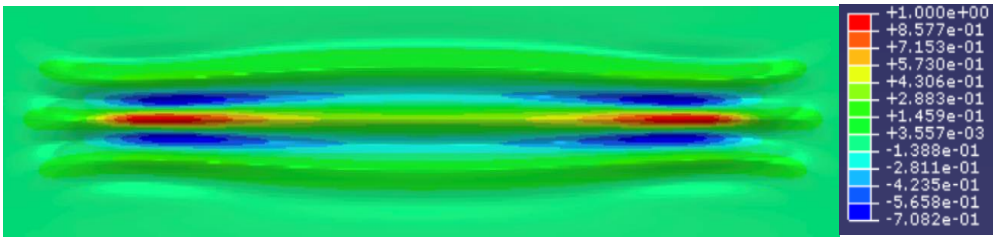

Figure 3.1: The first eigenmode for clamped-ends rectangular sheets with 1% pre-stretch, obtained from eigenvalue analysis for different aspect ratios for aspect ratios: (a) α = 1.35; (b) α = 2; (c) α = 2.5 and (d) α = 5.

It should be pointed out that the results from the eigenvalue analysis, including both the eigenmodes and the corresponding eigenvalues, depend sensitively on the width-to-thickness ratio (β) of the sheet as well as the applied pre-stretch. For the present study, the eigenmodes at a small pre-stretch ($\leq$ 1%) are used as geometric imperfections in the

post-buckling analysis (Section 3.3), while the eigenvalues can be used to estimate the critical strain for onset of buckling. With a pre-strain (ε_{pre}) and an eigenvalue (λ) associated with an incremental strain ($\varepsilon_0 \sim 0.5\%$), the critical strain is predicted as,

$$\varepsilon_{cr} = \varepsilon_{pre} + \lambda\varepsilon_0 \tag{3.12}$$

Eq. (3.12) assumes a linearized behavior from the pre-strain to the critical strain, which however does not necessarily apply for the hyperelastic sheet due to nonlinearity in both the material behavior and the kinematics. As shown in Figure 3.2a, the critical strain obtained by Eq. (3.12) depends on the pre-strain for the hyperelastic sheet. For comparison, the critical strain for a linear elastic sheet is found to be independent of the pre-strain. To accurately determine the critical strain for the hyperelastic sheet, we perform the eigenvalue analysis using increasingly large pre-strain until the first eigenvalue becomes sufficient small (Figure 3.12b). As shown in Figure 3.12a, as the pre-strain increases, the linear relation in (3.12) becomes less sensitive to the pre-strain and converges to the critical strain (~3.4% for $\alpha = 2.5$ and $\beta = 1000$). Following the same procedure, the critical strain for onset of buckling is determined as a function of the aspect ratios α and β, as shown in Figure 3.3.

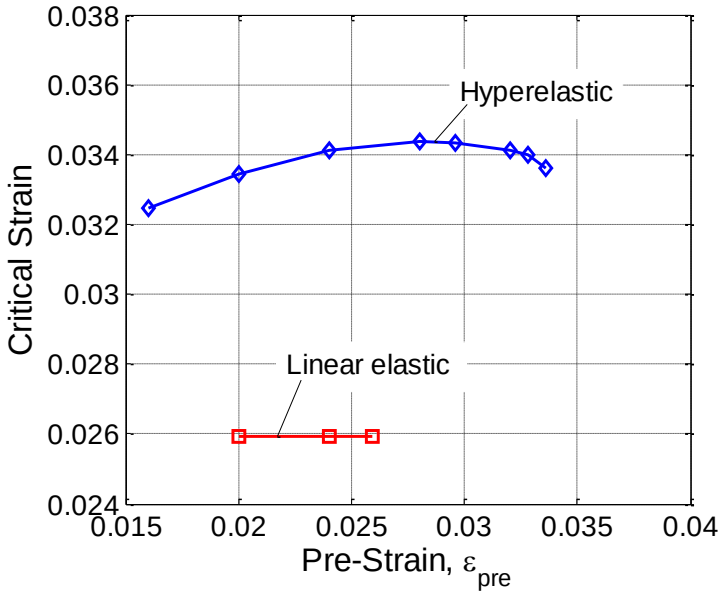

(a)

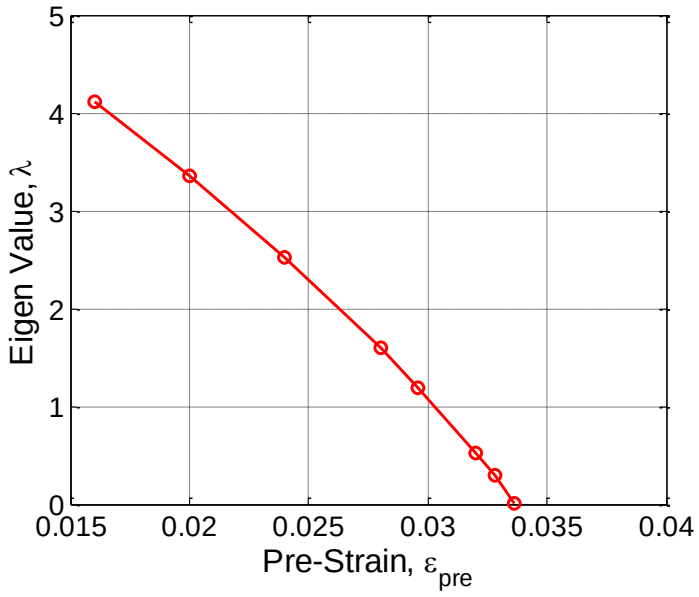

(b)

Figure 3.2: (a) Calculation of the critical strain for a hyperelastic sheet (α = 2.5 and β = 1000) by the eigenvalue analysis; (b) Change in eigen value as a function of pre-strain in a hyperelastic case.

Figure 3.3a shows the critical strain as a function of the in-plane aspect ratio (α) for β = 1000 and 2000. The shaded region for $\alpha < 1$ corresponds to the compression-free and hence wrinkle-free region as discussed in Chapter 2 (Figure 2.1). For $\alpha > 1$, the critical strain first decreases and then increases with increasing α, with a minimum critical strain at $\alpha \sim 2$. The dependence of the critical strain on the aspect ratio α is consistent with the magnitude of the transverse compressive stress shown in Figure 2.8, where the maximum compressive stress is predicted for the sheet with $\alpha = 2$. For $1 < \alpha < 2$, the critical strain increases rapidly as the aspect ratio approaches 1, and no buckling modes are obtained for $\alpha \leq 1.35$ with β = 1000. The critical aspect ratio is slightly different for β = 2000. For $\alpha > 2$, the critical strain increases with increasing α, but saturates at a constant level when $\alpha >> 1$. For a given aspect ratio α, the critical strain for onset of wrinkling decreases as β increases (e.g, by decreasing the sheet thickness), as shown in Figure 3.3b for α = 2.5. As expected, for an infinitely thin sheet ($\beta \rightarrow \infty$), the critical strain for wrinkling approaches zero, as is often assumed in the tension-field and other similar theories (Stein and Hedgepeth, 1961; Mansfield, 1970; Wu, 1978; Pipkin, 1986; Steigmann, 1990; Alder, et al., 2000; Coman, 2007).

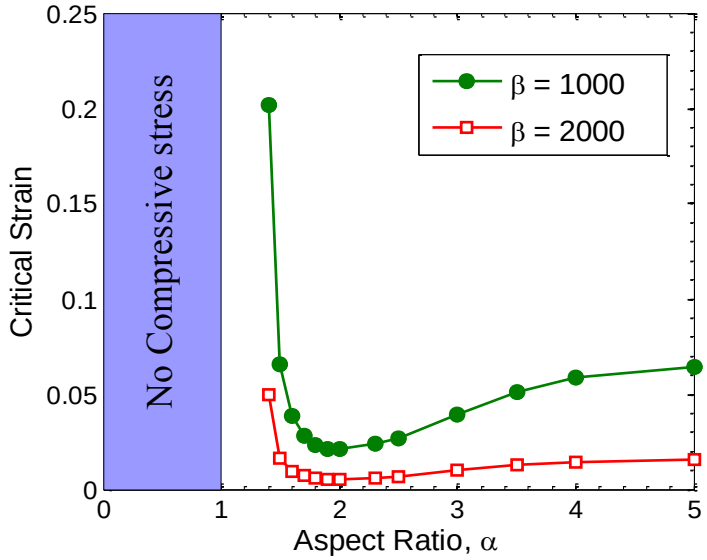

(a)

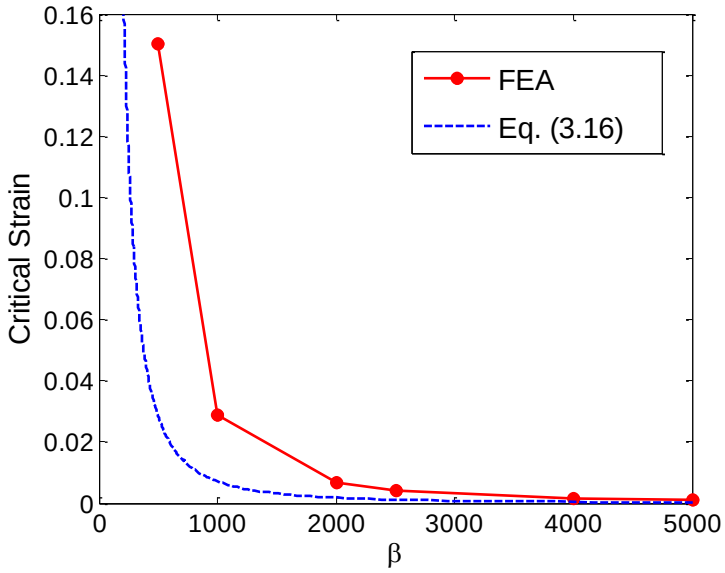

(b)

Figure 3.3: Critical strain obtained through a buckling eigenvalue analysis: (a) as a function of the in-plane aspect ratio (α) for β = 1000 and 2000; (b) as a function of β for α = 2.5.

To estimate the critical stress for wrinkling, a simplified model was suggested by Friedl et al. (2000). Consider a simply supported rectangular plate subject to a uniform

biaxial stress with tension in the *x* direction and compression in the *y* direction (see the inset of Figure 3.4a). The stress magnitudes are assumed to be proportional, e.g.,

$$\frac{\sigma_y}{\sigma_x} = C < 0\,. \tag{3.13}$$

The critical longitudinal stress for buckling of such a plate is (Timoshenko and Gere, 1985)

$$\sigma_{x,c} = \frac{\pi^2 E}{12(1-\nu^2)}\left(\frac{t}{b}\right)^2\left[\frac{n^4\left(\frac{b}{a}\right)^4 + 2m^2n^2\left(\frac{b}{a}\right)^2 + m^4}{-Cm^2 - n^2\left(\frac{b}{a}\right)^2}\right], \tag{3.14}$$

where the material is assumed to be linear elastic with Young's modulus *E* and Poisson's ratio *v*, and *n* and *m* are the numbers of half waves in the *x* and *y* directions, respectively. The dimensions of the plate are: length *a*, width *b*, and thickness *t*. Since the strain is typically small up to the critical stress, the material is assumed to be linear elastic here. For $\sigma_x > 0$ and $C < 0$, the critical stress in (3.14) is minimized with $n = 1$ while *m* varies with the ratio *b*/*a*, as shown in Figure 3.4a.

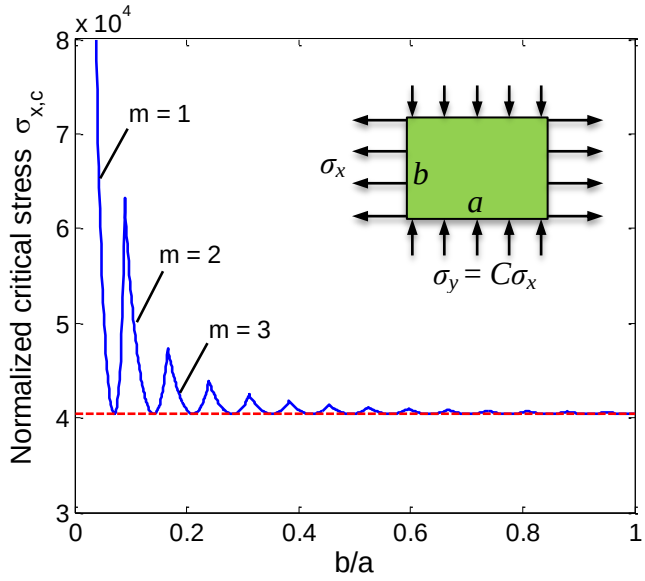

(a)

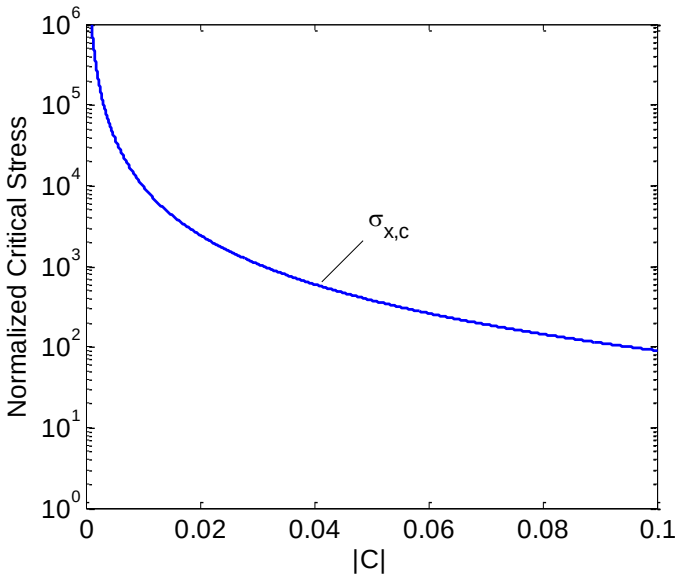

(b)

Figure 3.4: (a) The critical stress for a simply supported rectangular plate: (a) dependence on the ratio b/a for C = -0.01; (b) dependence on the ratio C for relatively large b/a. The stress magnitude is normalized by $\frac{\pi^2 E}{12(1-\nu^2)}\left(\frac{t}{a}\right)^2$. The dashed line in (a) indicates the minimum critical stress given by Eq. (3.15).

As an approximate model, Eq. (3.14) may be used to understand qualitatively the onset of stretch-induced wrinkling and the wrinkling modes as well as how they depend on the aspect ratio and the stretch. While Friedl et al. (2000) assumed the simply supported plate to have the same dimensions as the end-clamped sheet, we take the plate approximately to be part of the sheet where the transverse stress is compressive ($\sigma_y < 0$). Therefore, both the length and the width of the plate (a and b) vary with the aspect ratio of the original sheet and with the applied strain. The aspect ratio of the plate (b/a) may be estimated from the stress patterns in Figures 2.2 – 2.7 as a function of the aspect ratio. In addition, the stress ratio C also depends on the aspect ratio and the strain in general. The stress ratio C may be estimated from Figure 2.8a as a function of the nominal strain for each aspect ratio.

Taking the stress ratio approximately to be a constant (C = -0.01), the critical stress as predicted by Eq. (3.14) is plotted in Figure 3.4a as a function of the aspect ratio b/a. The number of half waves in the transverse direction (m) increases as b/a increases, qualitatively consistent with the eigenmodes shown in Figure 3.1. Note that the aspect ratio b/a for the region of compressive transverse stress in the end-clamped sheet is larger for α = 1.35 (Figure 2.4) than for α = 2 (Figure 2.5). As a result, the number of wrinkles in the eigenmode for α = 1.35 (Figure 3.1a) is greater than for α = 2 (Figure 3.1b). For a rectangular sheet of high aspect ratio ($\alpha > 3.7$), as the stretch-induced compressive stress splits into two regions, the ratio b/a for each region becomes independent of the aspect ratio α. However, as shown in Figure 3.1d for α = 5, the wrinkles extend beyond the

region of compressive stress, which apparently violates the boundary condition assumed in the simplified model.

For each *m*, the critical stress in Eq. (3.3) is minimized for a particular ratio *b*/*a*. It can be shown that the minimum critical stress is independent of *m*, as indicated by the horizontal dashed line in Figure 3.3a. For relatively large *b*/*a* (~1), the critical stress for onset of wrinkling depends weakly on the aspect ratio, which is approximately equal to the minimum critical stress, namely

$$\sigma_{x,c} \approx \frac{\pi^2 E}{3(1-\nu^2)}\left(\frac{t}{a}\right)^2\left(\frac{1-C}{C^2}\right). \tag{3.15}$$

As shown in Figure 3.4b, the approximate critical stress in (3.15) increases as $|C|$ decreases. The corresponding critical compressive stress in the transverse direction ($\sigma_{y,c} = C\sigma_{x,c}$) increases as well. To compare with the critical strain by the finite element eigenvalue analysis, we assume $b/a \sim W_0/L_0$ and $t/b \sim t_0/W_0$ in Eq. (3.15) so that

$$\varepsilon_{cr} \approx \frac{\pi^2}{3(1-\nu^2)}\left(\frac{1}{\alpha\beta}\right)^2\left(\frac{1-C}{C^2}\right). \tag{3.16}$$

The approximate critical strain predicted by Eq. (3.16) is plotted in Figure 3.3b as the dashed line (with α = 2.5 and C = -0.01), which shows similar trend as predicted by FEA. However, the dependence of the critical strain on α is more complicated as shown in Figure 3.3a, which may be captured qualitatively by taking the ratio C to be a function of α in Eq. (3.16).

As suggested by Figure 2.8a, the stress ratio C in the end-clamped rectangular sheet decreases with the nominal strain for each aspect ratio. By comparing the critical

compressive stress ($\sigma_{y,c}$) with the stretch-induced compressive stress (σ_y), we may predict qualitatively that stretch-induced wrinkles form at a critical nominal strain (ε_{c1}) when $\sigma_y = \sigma_{y,c}$. Subsequently, as the magnitude of σ_y increases and then decreases while the magnitude of $\sigma_{y,c}$ increases, a second critical nominal strain (ε_{c2}) may be predicted, beyond which the stretch-induced compressive stress drops below the critical stress. Therefore, stretch-induced wrinkles are expected only in between the two critical strains ($\varepsilon_{c1} < \varepsilon < \varepsilon_{c2}$). Such a behavior is confirmed by the post-buckling analysis in Section 3.3.

As predicted by Eq. (3.15), the critical stress decreases as the sheet thickness (t_0) decreases. On the other hand, the stretch-induced compressive stress as shown in Figure 2.8 is independent of the sheet thickness. By comparing the critical stress with the maximum magnitude of the stretch-induced compressive stress in Figure 2.8b, we classify the sheet thickness into three types, as indicated by three dashed lines for the critical stresses in Figure 3.5. First, for a thick sheet (t_{03}), the critical stress is greater than the stretch-induced compressive stress for all aspect ratios. Thus, the thick sheet would not wrinkle upon stretching, regardless of the in-plane aspect ratio. Second, for a thin sheet (t_{02}), the stretch-induced compressive stress is greater than the critical stress for aspect ratios within a window ($\alpha_1 < \alpha < \alpha_2$). Third, for a very thin sheet (t_{01}), the stretch-induced compressive stress is greater than the critical stress for all aspect ratios beyond a critical value ($\alpha > \alpha_1$). The qualitative predictions based on the simplified model are confirmed by the post-buckling analysis for the cases of a thin sheet ($\beta = 1000$) and a very thin sheet ($\beta = 2000$) in Section 3.3.

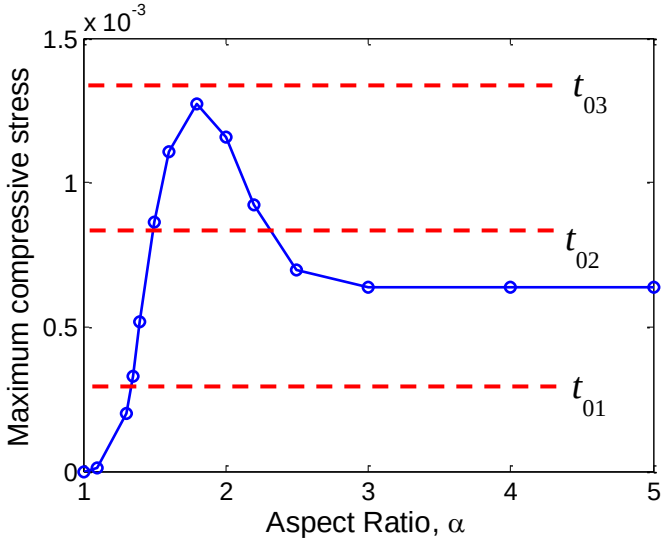

Figure 3.5: Maximum magnitude of the stretch-induced compressive stress as a function of the aspect ratio. Dashed lines indicate the critical buckling stresses for different sheet thicknesses, $t_{03} > t_{02} > t_{01}$.

3.3 POST-BUCKLING ANALYSIS

To perform the post-buckling analysis a small geometrical imperfection is initially introduced in the sheet by using the eigenmodes obtained from the eigenvalue analysis in Section 3.2. The numerical results in general depend on the number of eigenmodes and their amplitudes used as the geometrical imperfection. For the purpose of convergence, a sufficiently large number of eigenmodes and sufficiently small amplitude must be used. In the present study, the first four eigenmodes are used for each sheet, and the amplitude of imperfection is about 1% of the sheet thickness. The RIKS method as implemented in ABAQUS is employed for the post-buckling analysis.

Figures 3.6 and 3.7 show the results from the post-buckling analysis for a rectangular sheet with $\alpha = 2.5$ and $\beta = 1000$. The evolution of stretch-induced wrinkles is

shown in Figure 3.6 as the contour plots of the out-of-plane displacement (u_z) when stretched to different nominal strain levels. The wrinkles are confined within the center region of the sheet, similar to the region where the transverse stress is compressive (Figure 2.6a). Although the compressive stress is present up to 95% nominal strain for α = 2.5 (Figure 2.1), the wrinkles are obtained only up to 30% nominal strain, beyond which the out-of-plane displacement is nearly zero everywhere. The out-of-plane displacement along the mid-section of the sheet ($x = L_0/2$) is plotted as the wrinkle profile in Figure 3.7a. It is seen that the wrinkle amplitude grows from ε = 5% to ε = 10%. Subsequently, as the nominal strain increases further, the wrinkle amplitude decreases and eventually all wrinkles are nearly flattened at ε = 30%. The wrinkle amplitude, defined as $A = [\max(u_z) - \min(u_z)]/2$ from the numerical results, is plotted as a function of the nominal strain in Figure 3.7b. The critical strain predicted by the eigenvalue analysis in Section 3.2 is marked for comparison. Evidently, the wrinkle amplitude does not grow appreciably until the critical strain (ε_{cr1}) is reached. Furthermore, the wrinkle amplitude reaches the maximum when $\varepsilon \sim 10\%$ and drops to zero at $\varepsilon \sim 30\%$ (ε_{cr2}) and beyond. Such a wrinkling behavior is in drastic contrast with the scaling analysis by Cerda and Mahadevan (2003), which predicted the wrinkle amplitude to increase monotonically with increasing strain, i.e., $A \sim (Lt)^{1/2} \varepsilon^{1/4}$; more discussion on the scaling analysis is presented in Section 3.4.

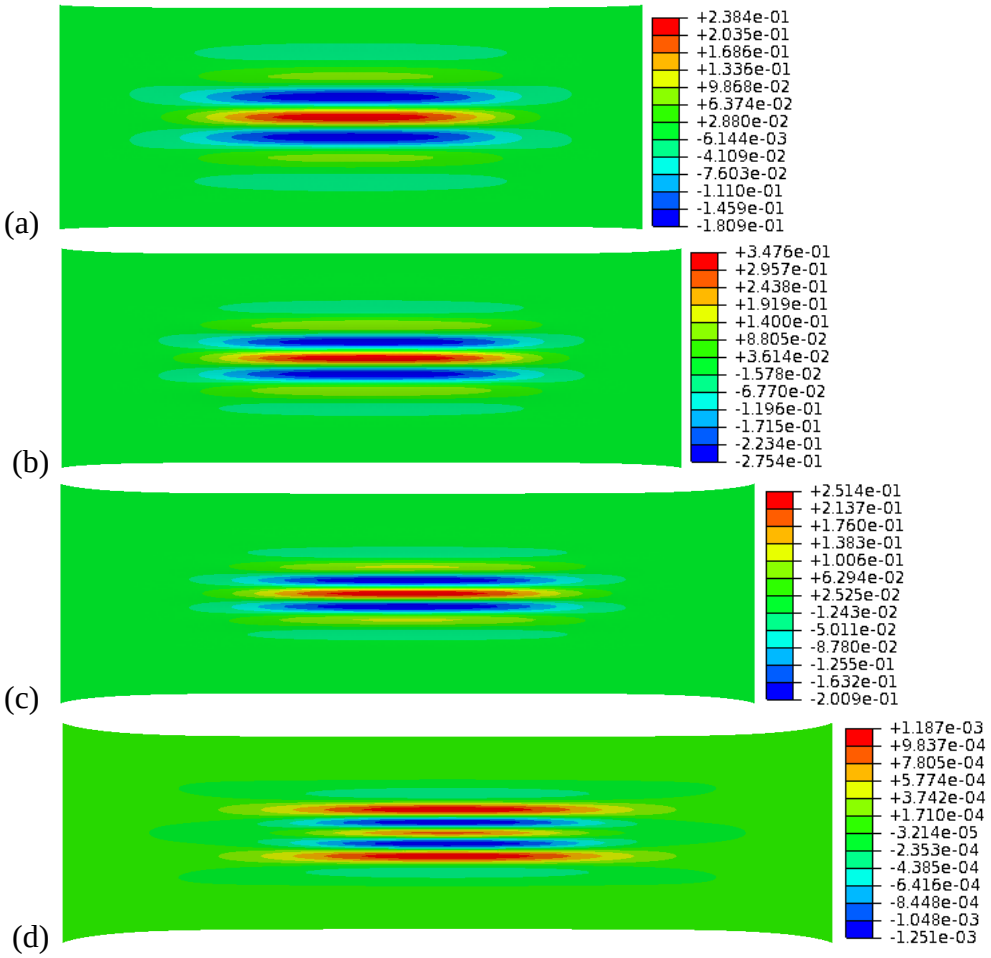

Figure 3.6: Evolution of stretch-induced wrinkles in an end-clamped rectangular sheet with α = 2.5 and β = 1000: (a) ε = 5%; (b) ε = 10%; (c) ε = 20%; (d) ε = 30%.

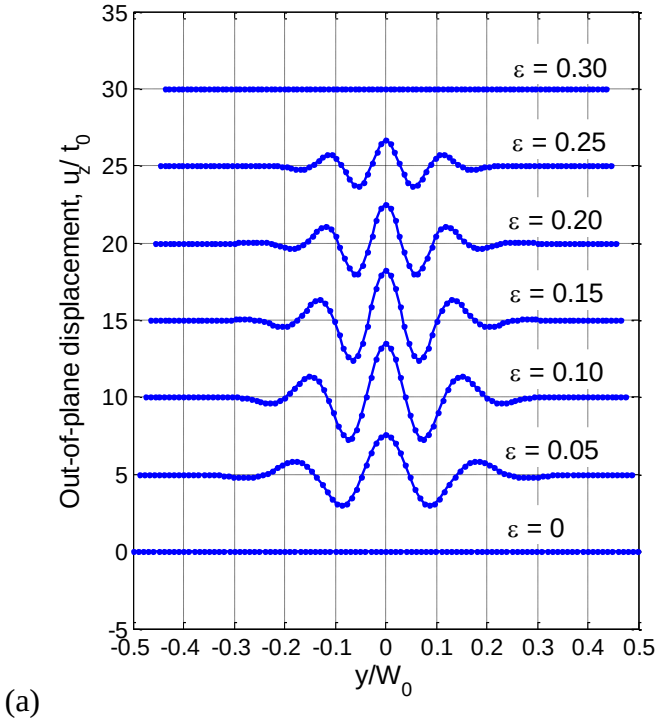

(a)

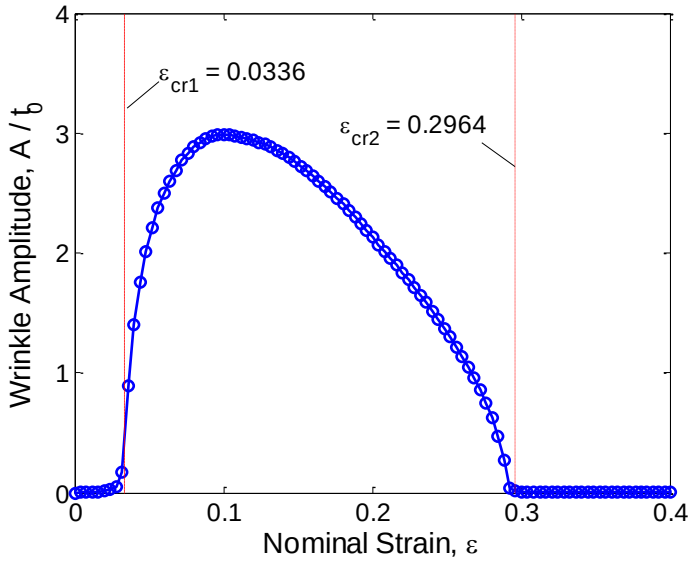

(b)

Figure 3.7: Simulated wrinkling behavior for an end-clamped rectangular sheets with α = 2.5 and β = 1000: (a) Out-of-plane displacement along the mid-section of the sheet under different nominal strains; (b) Wrinkle amplitude as a function of the nominal strain.

As shown in Figure 3.6, the wrinkles are largely confined in the central region of the sheet where transverse stress is compressive. However, the wrinkling region may not be exactly the region with the compressive stress. As shown by Stein and Hedgepeth (1961), for a stretched membrane with a hub subjected to torsion, the wrinkles could extend far beyond the compression region in a plate under same loading, which they attributed to the "over contraction" in the direction perpendicular to the wrinkling of the membrane. In the tension-field theory, the wrinkling region may be determined by replacing Poisson's ratio with an arbitrary function to result in a zero principal stress perpendicular to the wrinkles, rendering a different 2-D boundary value problem for the plate.

3.3.1 Effect of Geometry

Qualitatively, the stretch-induced wrinkling behavior simulated by the post-buckling analysis is similar for different aspect ratios (α and β). Quantitatively, however, the wrinkling response depends on both α and β, including the critical strain as shown in Figure 3.3 and the post-buckling behavior (e.g., the wrinkle amplitude and wavelength). First, to study the effect of the in-plane aspect ratio (α), we fix the sheet thickness (t_0) and width (W_0) so that β = 1000 while varying the sheet length (L_0) to change α. It is found that, for β = 1000, the stretch-induced wrinkle amplitude is negligibly small for the sheets with α smaller than 1.7 or larger than 3.5. Only when $1.7 < \alpha < 3.5$ is the stretch-induced compressive stress sufficiently large to cause wrinkling of the sheet. Figure 3.8 shows the wrinkle amplitude as a function of the nominal strain for different in-plane aspect ratios. For each aspect ratio, the lower and upper critical strains are determined from the post-

buckling analysis, defining a wrinkling region in the α-ε plane, as shown in Figure 3.9. As expected, the wrinkling region is within the region of stretch-induced compressive stress shown in Figure 2.1. In addition to the lower and upper critical strain, the strain with the maximum wrinkle amplitude is also shown in Figure 3.9, which is around 10% for all aspect ratios.

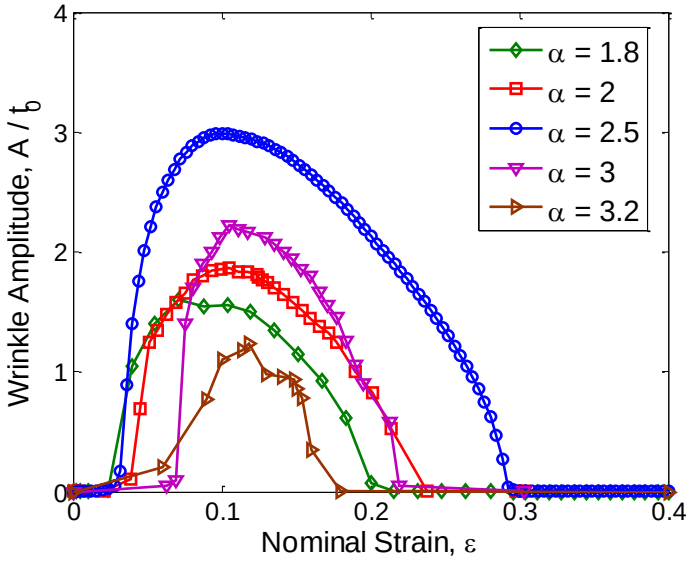

Figure 3.8: Stretch-induced wrinkle amplitude as a function of the nominal strain for the end-clamped rectangular sheets with different aspect ratios. The width-to-thickness ratio (β) is 1000 for all cases.

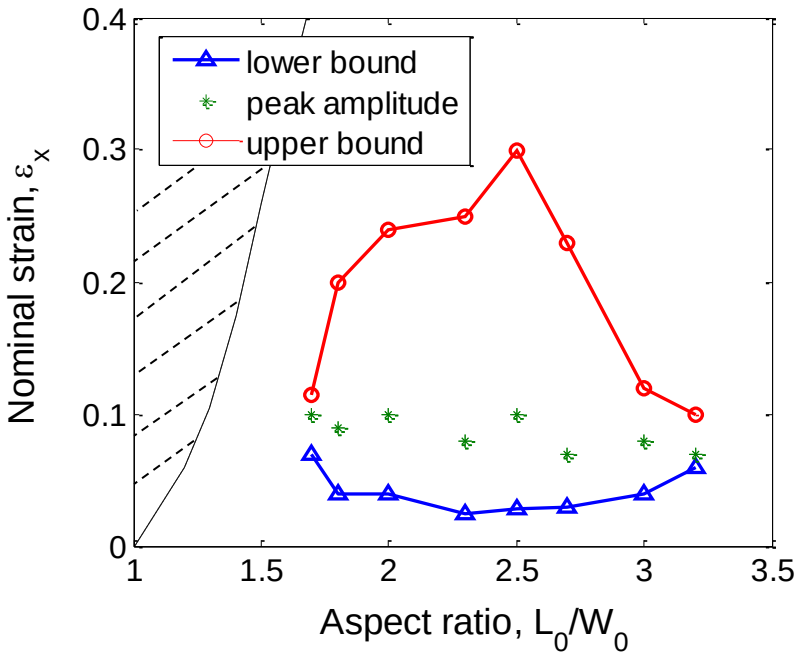

Figure 3.9: The wrinkling region in the α-ε plane for β = 1000. The dashed line is the boundary for the region with stretch-induced compressive stress.

Next, to study the effect of β, we fix the width and length of the sheet with α = 2.5 but vary the sheet thickness. Figure 3.10 shows the wrinkle amplitudes obtained by the post-buckling analysis for three sheets with β = 1000, 2000 and 5000. As predicted by the buckling eigenvalue analysis in Section 3.2, the critical strain for onset of wrinkling decreases with increasing β (Figure 3.3b). As a result, the wrinkle amplitude increases with increasing β. In all cases, the wrinkle amplitude first increases and then decreases with increasing strain. The upper critical strain at which the stretch-induced wrinkles are suppressed also increases with increasing β. Again, this is consistent with the evolution of stretch-induced compressive stress in the end-clamped sheet shown in Figure 2.8a.

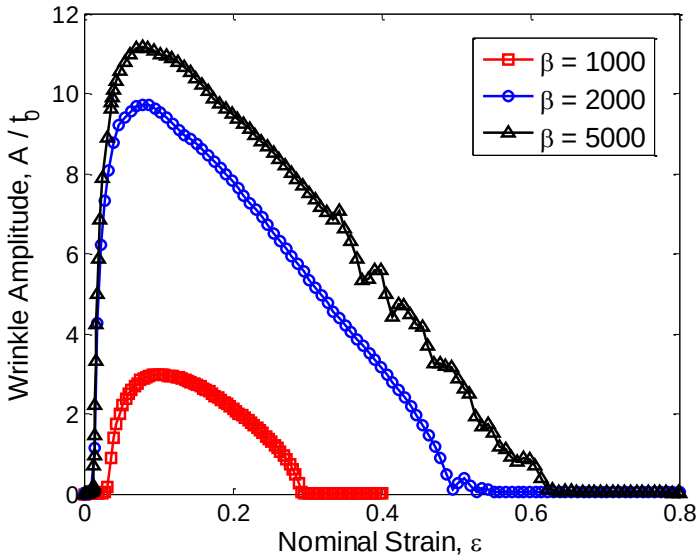

Figure 3.10: Stretch-induced wrinkle amplitude as a function of the nominal strain for the end-clamped rectangular sheets with different out-of-plane aspect ratios (β). The in-plane aspect ratio (α) is 2.5 for all cases.

Besides the critical strains and wrinkle amplitude, it is found that the number of wrinkles increases with increasing β. Figures 3.11 and 3.12 show the two cases with β = 2000 and 5000, respectively. In each case, it is observed that the number of wrinkles remains constant as the sheet is stretched. However, as the sheet width decreases due to Poisson's effect, the wrinkle wavelength decreases with increasing strain. As further discussed in Section 3.4, the wrinkle wavelength is in good agreement with the scaling analysis by Cerda and Mahadevan (2003).

(a)

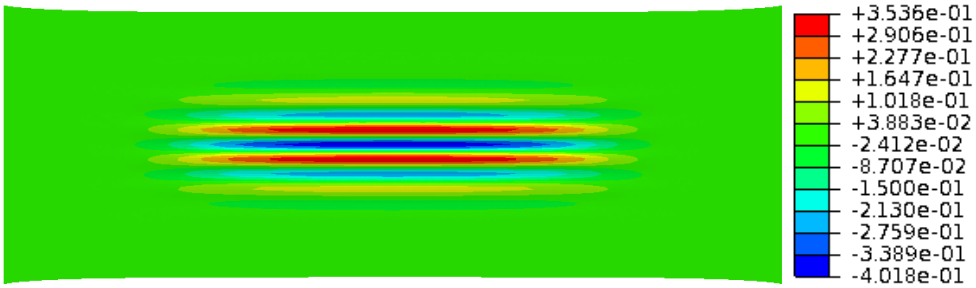

(b)

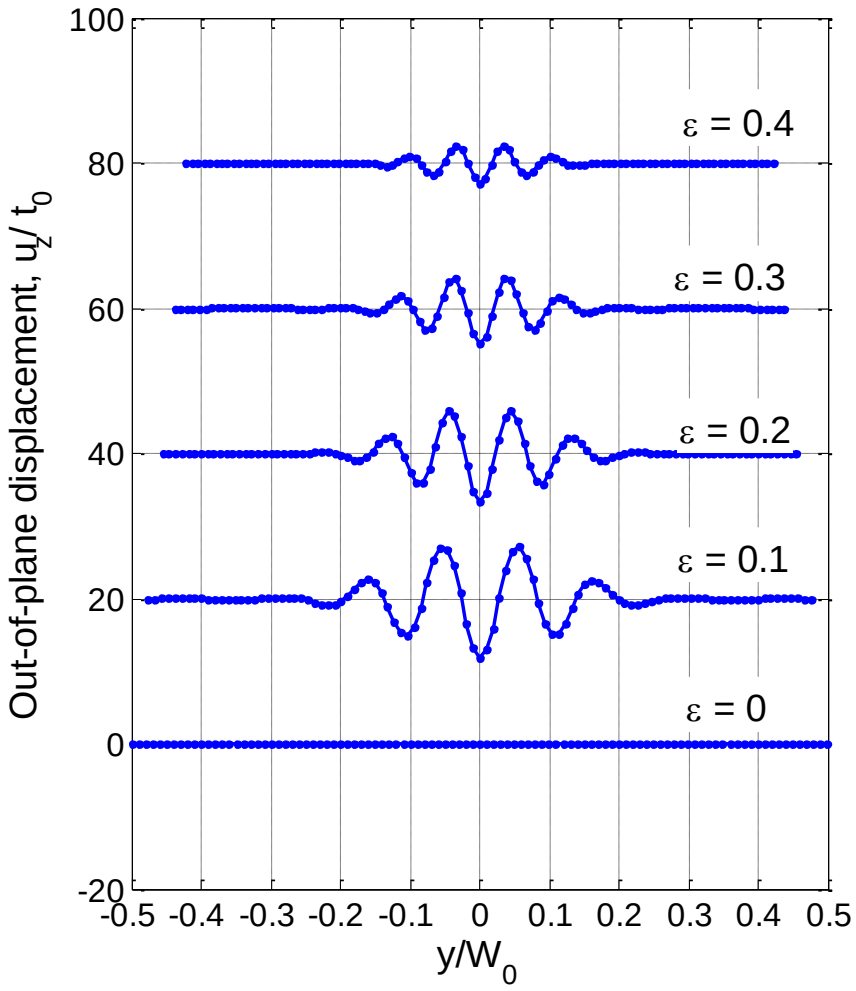

Figure 3.11: (a) Stretch-induce wrinkle pattern in an end-clamped rectangular sheet with α = 2.5 and β = 2000 at 10% nominal strain; (b) Out-of-plane displacement along the mid-section of the sheet with α = 2.5 and β = 2000 under increasing nominal strain.

(a)

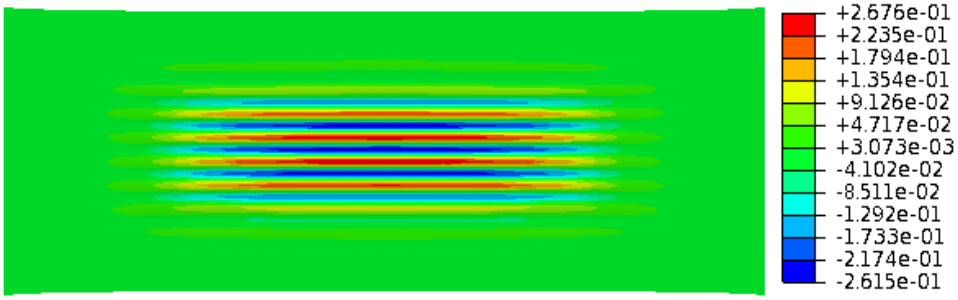

(b)

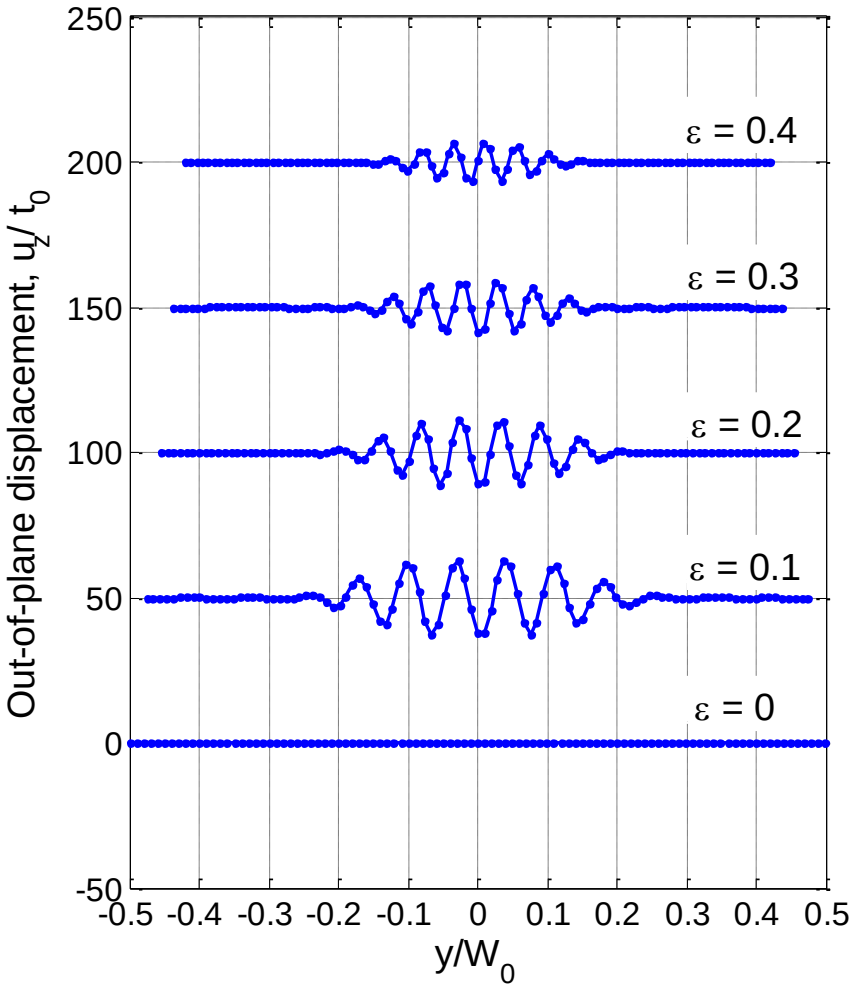

Figure 3.12: (a) Stretch-induce wrinkle pattern in an end-clamped rectangular sheet with α = 2.5 and β = 5000 at 10% nominal strain; (b) Out-of-plane displacement along the mid-section of the sheet with α = 2.5 and β = 5000 under increasing nominal strain.

Furthermore, by increasing β, the wrinkling region in the α-ε plane expands, as shown in Figure 3.13a. In comparison to the case of β = 1000 (Figure 3.9), the lower critical strain for onset of wrinkling is lower for β = 2000 and the upper critical strain is higher. In both cases, the wrinkling region in the α-ε plane is within the region of the stretch-induced compressive stress. Referring to the classification illustrated in Figure 3.5, the sheet with β = 1000 is thin and the sheet with β = 2000 is very thin. Therefore, for the latter case, stretch-induced wrinkling is predicted for $\alpha > 1.2$, with no upper bound for the aspect ratio of the sheet. Figure 3.13b shows the maximum wrinkle amplitude as a function of α for β = 1000 and 2000. We note in Figure 3.13a that both the lower and upper critical strains depend on the in-plane aspect ratio of the sheet for β = 1000. For β = 2000, the lower critical strain is nearly independent of the aspect ratio, while the upper critical strain first increases and then decreases, eventually becoming independent of the aspect ratio for $\alpha > 5$. The dependence of the upper critical strain on the aspect ratio is similar to that of the maximum compressive stress in Figure 2.8b, and the dependence of the maximum wrinkle amplitude for the very thin sheets (β = 2000) in Figure 3.13b is similar too.

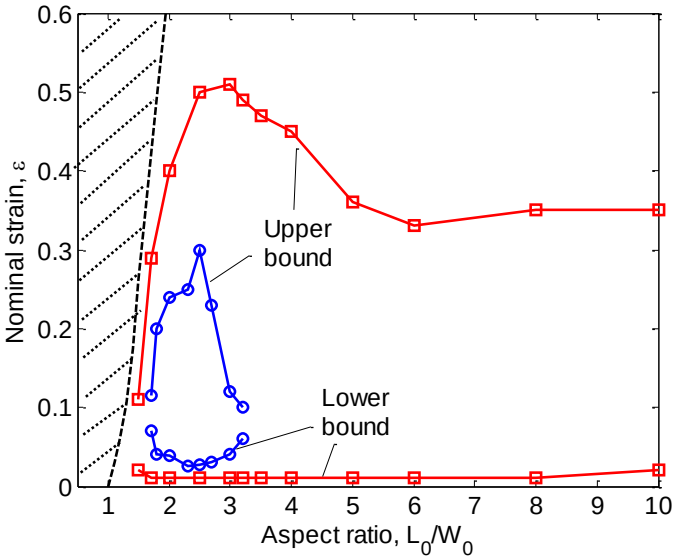

(a)

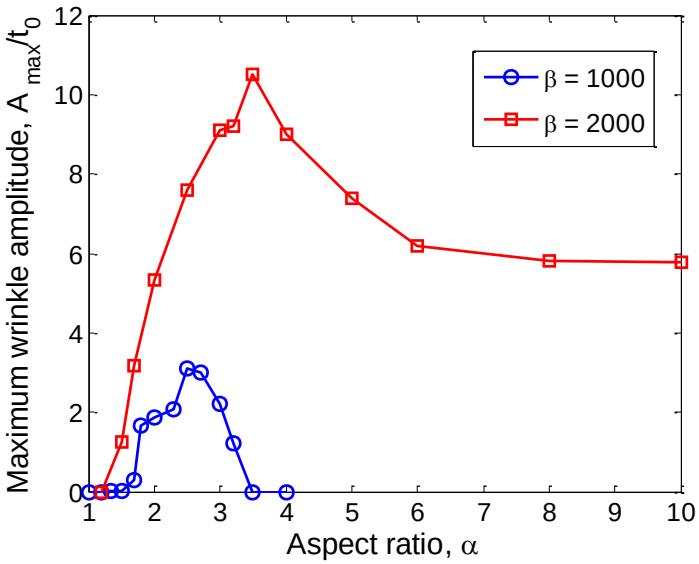

(b)

Figure 3.13: (a) Wrinkling regions in the α-ε plane for two different width-to-thickness ratios. The dashed line is the boundary for the region with stretch-induced compressive stress; (b) Maximum wrinkle amplitude as a function of in-plane aspect ratio (α).

3.3.2 Effect of Elastic Moduli

For the incompressible neo-Hookean model of the hyperelastic thin sheet, the material property is represented by one parameter only, that is, the initial shear modulus (μ). While the stretch-induced compressive stress is linearly proportional to the shear modulus, the wrinkling behavior (including both the amplitude and the wavelength) is found to be independent of the shear modulus. This can be understood from a dimensional consideration where the wrinkle amplitude and wavelength normalized by one of the sheet dimensions (e.g., the thickness) depend only on dimensionless parameters (e.g., α, β, and ε). However, if the material is compressible, Poisson's ratio of the material would play a role in the formation of stretch-induced wrinkles. In the limiting case when Poisson's ratio $\nu = 0$, we would have no stretch-induced compressive stresses in all cases and hence no stretch-induced wrinkles, regardless of the sheet geometry. By using a compressible neo-Hookean model, Figure 3.14 shows the effect of Poisson's ratio on stretch-induced wrinkling in end-clamped rectangular sheets with α = 2.5 and β = 1000. It can be seen that the wrinkle amplitude decreases drastically as Poisson's ratio decreases. For α = 2.5 and β = 1000, the wrinkle amplitude becomes negligibly small when Poisson's ratio is 0.3 or lower. Therefore, stretch-induced wrinkles in large-scale membranes and thin sheets may be reduced by using materials with relatively low Poisson's ratios.

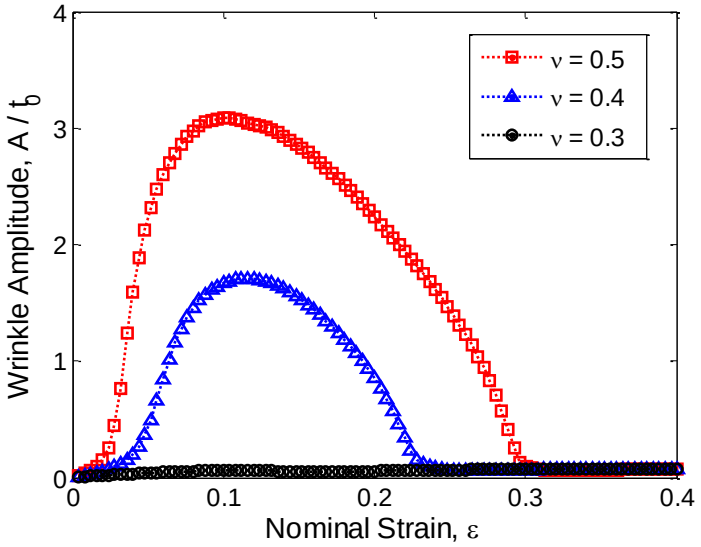

Figure 3.14: Stretch-induced wrinkle amplitude as a function of the nominal strain for the end-clamped rectangular sheets with different Poisson's ratios. The in-plane aspect ratio (α) is 2.5 and out-of-plane aspect ratio (β) is 1000.

3.4 COMPARISON WITH SCALING ANALYSIS

Figure 3.15 plots the normalized wrinkle wavelength (λ/W_0) versus $\alpha^{1/2}\beta^{-1/2}\varepsilon^{-1/4}$, comparing the numerical results with Eq. (3.15). Two sets of numerical results are presented, for β = 1000 (open symbols) and 2000 (filled symbols), respectively. For each set, the wavelengths are determined from the post-buckling analysis for three different in-plane aspect ratios (α = 2, 2.5, and 2.7) at different nominal strains. Evidently, the numerical results follow the prediction by the scaling analysis reasonably well; the latter is plotted as the dashed line with a slope depending on Poisson's ratio (taken to be 0.5 here). In their scaling analysis, Cerda and Mahadevan (2003) assumed a periodic wrinkle profile across the sheet width. However, as shown in

Figure 3.7a, Figure 3.11, and Figure 3.12, the sheet remains flat near the free edges and the wrinkling profiles are modulated by a long-wavelength mode.

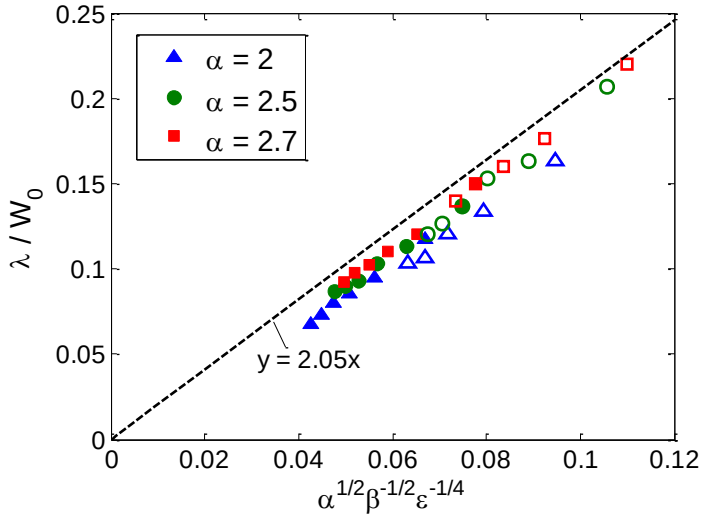

Figure 3.15: Normalized wrinkle wavelength from the post-buckling analysis, in comparison with the prediction by a scaling analysis (dashed line). The open symbols show numerical results for β = 1000, and the filled symbols for β = 2000.

The evolution of wrinkle amplitude from numerical simulations as shown in Figure 3.7b, Figure 3.8, and Figure 3.10 is in drastic contrast with the prediction by Eq. (3.11). First, it is noted that no critical strain is predicted by the scaling analysis. In other words, the stretch-induced wrinkles would appear upon stretching to any strain level. This may be considered approximately true for infinitely thin sheet ($\beta \to \infty$). As shown in Figure 3.3, the critical strain for onset of wrinkling depends on the two aspect ratios, α and β, but decreasing with increasing β. On the other hand, Puntel et al. (2011) predicted a sequence of critical strains for increasing number of wrinkles. For a rectangular sheet with α = 2.5 and β = 1000, the minimum critical strain predicted by their analysis would

be 4.5 x 10^{-6}, which however is significantly lower than the present numerical results (Figure 3.3). The discrepancy is most likely due to the different boundary conditions assumed by Puntel et al. (2011) in their analysis.

Moreover, Eq. (3.11) predicts that the wrinkle amplitude should increase monotonically with increasing strain, while the numerical simulations presented in this chapter show a non-monotonic behavior (Figure 3.7b, Figure 3.8, and Figure 3.10). Most strikingly, the wrinkle amplitudes in all numerical simulations decrease with increasing strain roughly when $\varepsilon > 10\%$ and eventually become zero beyond the upper critical strain. Similar behavior was observed by Zheng (2009) and confirmed experimentally in Chapter 4. By a dimensional consideration (see Appendix A for more details), the wrinkle amplitude may be written as

$$A/t_0 = f(\varepsilon, \alpha, \beta, \nu) \tag{3.17}$$

which is generally more complicated than the scaling relation in Eq. (3.11). By using a different geometric constraint, Puntel et al. (2011) modified the scaling relation to include a multiplicative factor that depends on the strain and Poisson's ratio. However, the exact dependence on strain was not given explicitly, and the scaling with the sheet geometry (length, width, and thickness) remains the same as that by Cerda and Mahadevan (2003). As shown in Figure 3.8, for the same width and thickness, the wrinkle amplitude first increases with the length and then decreases, with the maximum amplitude observed for $\alpha = 2.5$. In other words, the wrinkle amplitude does not increase monotonically with increasing length (L_0) of the sheet, again, in contrast with the scaling relation in Eq. (3.11). We note that such a behavior may not be attributed simply to the nonlinear elastic

material model used in the present study. The results are qualitatively similar if a linear elastic material model is used. It may thus be concluded that, while the scaling analysis offers a satisfactory prediction of the wrinkle wavelength, its prediction for the wrinkle amplitude is largely erroneous.

3.5 SUMMARY

In this chapter, the buckling and post-buckling analysis of end-clamped rectangular thin sheets under stretching are presented. It is found that stretch-induced wrinkling occurs due to the boundary constraint by the clamped ends and Poisson's effect. The critical conditions for onset of wrinkling are determined numerically in terms of the sheet geometry and the applied nominal strain. The evolution of wrinkle patterns are simulated by post-buckling analysis and compared to the previous predictions by a scaling analysis. The results suggests that stretch-induced wrinkling in thin sheets may be suppressed (1) by increasing the sheet thickness; (2) by choosing appropriate in-plane aspect ratio α; (3) by stretching beyond the upper critical strain; and (4) by choosing a material with a small Poisson's ratio.

CHAPTER 4

Wrinkling in Polyethylene Sheets: Experimental Measurements

4.1 INTRODUCTION

To date not much experimental data has been reported on stretch-induced wrinkling in thin sheets. The scaling analysis by Cerda et al. (2003) predict that the wrinkle wavelength should decrease with stretch and this was confirmed by the experimental results reported in the paper. However, no experimental results were reported for the amplitude of wrinkles. Zheng (2009) predicted that the wrinkle amplitude will vary non-monotonically with strain, similar to the predictions of the hyperelastic model as shown in Chapter 3, but their experimental study was inconclusive. In this chapter, an experimental study is conducted on wrinkling in polyethylene sheets stretched with clamped-ends. To quantify these wrinkles, a non-contact technique is used. First we briefly explain the 3-D Digital Image Correlation (DIC) technique used to measure wrinkles, and then the experimental setup and procedure are explained. Next, the results obtained from stretching of polyethylene sheets under clamped-ends are discussed. The results from standard uniaxial tension test and relaxation tests, performed to characterize the material response are also described. Finally, the variation of wrinkling amplitude with strain is described.

4.2 3D-DIGITAL IMAGE CORRELATION

This technique is a combination of stereo-vision technique and DIC. Stereovision technique is used to recover a 3D geometry of the scene. DIC technique relates the

changes in the 3D geometry in comparison to a reference state and extracts the deformation in terms of the displacements and displacement gradients over the field of observation. 3D-DIC technique has various applications in material testing, component dimensioning, strain computation, and FE models verification. This technique is used in the present study to record the deformation in the polyethylene sheets under stretching. Detailed information about this technique can be found in Luo et al. (1993) and Sutton et al. (2009).

In this technique, a stereoscopic setup of two cameras, C_1 & C_2 is required as shown schematically in Figure 4.1. A speckle pattern is required on the surface of target geometry, which is viewed through the two cameras. The cameras are placed facing the target geometry such that each captures an image of the target at the same time. Here we define a set of coordinate systems to understand the computational procedure used in the imaging process. The global coordinate system is marked as GCS in Figure 4.1 with X, Y and Z axes. Two other coordinate systems located at C_1 and C_2, are the camera coordinate systems (CCS) with coordinate axes (x_1, y_1) & (x_2, y_2) respectively. Note that, the images taken by the two cameras are only 2-D projections of the target. Suppose, W (X, Y, Z) is any point to be measured and w_{c1} (x_1, y_1) and w_{c2} (x_2, y_2) are its stereo projections in the image planes of cameras C_1 and C_2, respectively. To extract the actual coordinates of a point in GCS from the CCS, the following two steps are followed.

First, the two points 'w_{c1}' and 'w_{c2}' are matched to verify that they belong to a same physical point, 'W'. The matching process is based on the correlation score of two images that are available from each camera. The correlation is done by measuring the

similarity of a fixed window in the first image to a shifting window in the second image. This window is called a facet and its size is defined in terms of number of image pixels. Second, a calibration procedure is performed, in which a target of known geometry is shown to the two cameras simultaneously in different orientations. With this process, the relative position and orientation of the two cameras is calculated. In addition to this, the intrinsic parameters of the cameras such as focal length and lens distortion are also computed through calibration. Once the calibration is completed, the setup is able to generate 3D coordinates of the target in the GCS.

Next, the displacements and displacement gradients are computed through another algorithm. First, a sequence of pairs of stereo images at different points of time (or loading stages) is generated. With a pair of images taken at any time (or load step), the corresponding 3D geometry of the target is calculated. The 3D coordinates of the target available for each time or load step are compared to the reference state and the displacements and displacement gradients are calculated. It should be noted that once the setup is calibrated, the experiments are to be carried out without altering the setup.

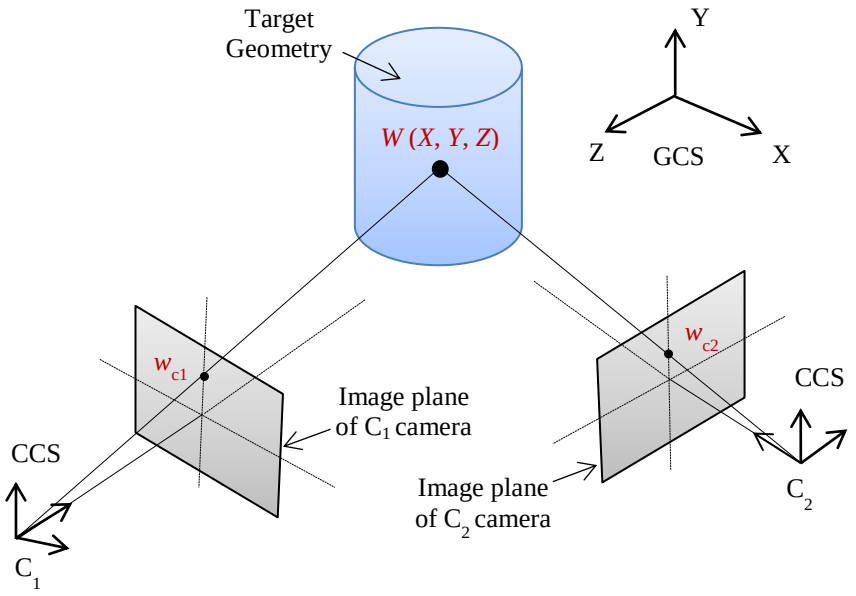

Figure 4.1: Schematic diagram of a 3D-DIC setup with two cameras C_1 and C_2 facing the specimen. *'W'* is an arbitrary point on the specimen, and w_{c1}, w_{c2} are its projections on the image planes of camera C_1 and C_2, respectively.

4.3 EXPERIMENTAL PROCEDURE

4.3.1 Specimen Preparation

The material used in this study is a commercial grade polyethylene. The molecular weight of the polyethylene is not clear as no attempt was made to identify it. The polyethylene is available in the form of a thin sheet with a nominal thickness (t_0) of 100 μm. The width of each sheet specimen subjected to stretching is kept constant at W_0 = 100 mm and lengths used are L_0 = 250 mm and L_0 = 200 mm. Due to the presence of residual stresses some undulations and creases are typically observed in the sheet (Figure 4.2a). Each specimen is heat-treated in order to achieve a relatively flat shape. The sheet is placed in-between two plexiglass plates and kept at a temperature of 75°C for ~24

hours followed by slow cooling of the specimen in the furnace. This process provides a relatively flat sheet surface as shown in Figure 4.2b.

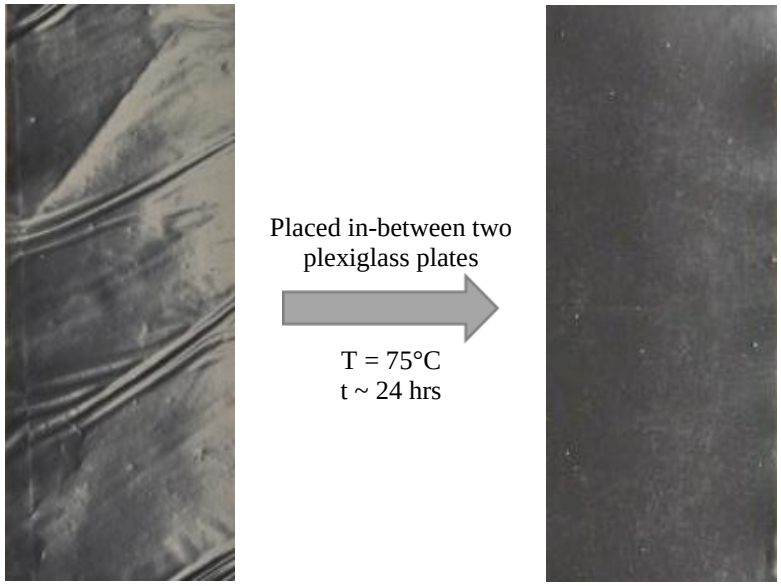

Figure 4.2: An optical image of polyethylene sheet specimen, (a) before heat treatment; (b) after heat treatment.

Next, a speckle pattern is made on each specimen manually, using a white paint marker. Such a pattern as shown in the Figure 4.3 is found to be sufficient to record the displacements and strains up to a stretch (L/L_0) of 1.4. The speckle pattern is formed only at the center of each specimen covering whole specimen width (W_0 = 100 mm) and a height of approximately 15 mm. Figure 4.3a shows a full sheet specimen and Figure 4.3b shows the area of the sheet covered with the speckle pattern. This field-of-view is dictated by the need to measure the wrinkle amplitude at high resolution over the entire width of the specimen. After forming the speckle pattern, the specimen is clamped to the

rigid grips at the two ends. To clamp the sheet at the two ends, a special jig is used. Using the jig, the sheet is attached to the clamps at either end ensuring correct alignment of the sheet with respect to the clamps and the loading direction. A description of clamping the sheet at two ends is given in Appendix B.

(a) (b)

Figure 4.3: (a) A full polyethylene sheet specimen with speckle pattern; (b) A close-up view of the speckle pattern made on a polyethylene sheet specimen using a 0.7 mm tip white paint marker.

4.3.2 Experimental Setup and Test Procedure

Two CCD cameras are used for the experiments each with a resolution of 1624 X 1236 pixels with a 50 mm lens. The shutter speed and aperture of these cameras can be varied between 0-2000 ms and f/2.8-f/32 respectively. Figure 4.4a shows a schematic diagram of the experimental setup used and the relative distance and positioning of the cameras. The two cameras are placed approximately at a distance of 1.3 m away from the specimen with a relative distance of 0.45 m from each other (a top-view of the setup is also shown inset in Figure 4.4a). A commercial 3D-DIC software package, ARAMIS is used in this study. The calibration is done using a calibration panel that has two scale bars

and a set of reference points as shown in Figure 4.4b. During the calibration process, the calibration panel is imaged in 13 different orientations by the two cameras. With this calibration process it was determined that the measuring volume (Height/Width/Depth) achieved is 195/150/135 mm. The camera angle (2α) computed through the calibration process is 19.5° (see top-view in Figure 4.4a). The facet size of 15 x 15 pixels and step size of 13 x 13 pixels is found to be sufficient in these experiments to record the out-of-plane deformation. The shutter time used for the experiments is ~10 ms with an aperture of approximately f/5.6. With this setup, each specimen of is found to have 8-10 pixels/mm along its width. In addition to this, two lamps, each of 250 W, placed approximately 2 m away from the specimen, are used while taking images. The field of view of the two cameras is adjusted in such a way that the speckle pattern always stays in the field of view when the sheet is stretched, as schematically shown in Figure 4.4a. To hold the clamped specimen in the Intron machine, a pinned support is used at the two ends (see Appendix A for details). By using this type of support, the clamps are free to rotate with respect to the pins at the two ends.

After installing the clamped polyethylene sheet specimen on the Instron machine, a pre-stretch ($\leq 0.1\%$) is applied to avoid any initial slack in the sheet. The Instron machine is controlled by another computer program to control the displacement of the upper cross head. After installing the specimen, the upper clamp is moved upwards while the two cameras simultaneously take images of the specimen at specified time intervals. With in-plane aspect ratio (α) of 2.5 and out-of-plane aspect ratio (β) of 1000, the sheet is stretched upto 40% strain at strain rates of 0.0169 s^{-1} or 0.00169 s^{-1}. Based on the

deformation of the speckle pattern, which is viewed through the cameras, the strains and displacements are calculated. However, beyond 40% strain, the speckle pattern is found to be insufficient to measure the deformation using DIC.

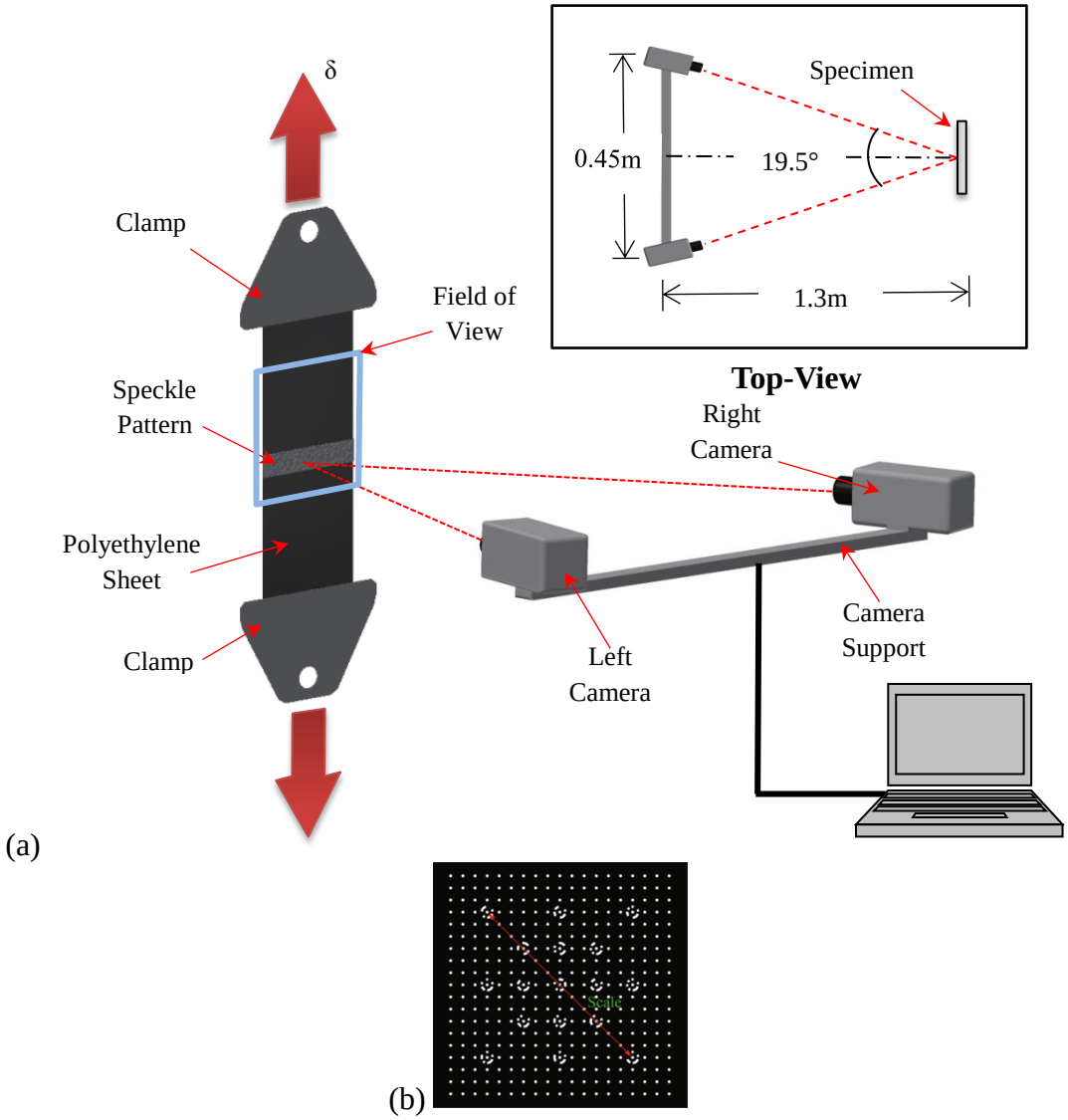

Figure 4.4: (a) Schematic diagram showing the 3D-DIC setup used to perform stretching tests on a clamped sheet; (b) Calibration panel used for the calibration process.

4.4 RESULTS

4.1 Uniaxial Tension Tests

To determine the constitutive model for polyethylene, we performed standard uniaxial tension tests using narrow strips of polyethylene with L_0 = 150 mm, W_0 = 10 mm, and t_0 = 0.1 mm. From the results of the hyperelastic analysis described in Section 3.3, wrinkles are not expected to form in these specimens. Figure 4.5a shows the nominal stress-strain curves measured at three different strain rates with a constant strain rate loading and unloading history. The stress-strain behavior appears to be characteristically viscoplastic, with nonlinear rate-dependent loading and unloading as well as a residual strain at the end of the unloading. Even though Figure 4.5a indicates presence of residual strain upon unloading, but this strain is recovered rather quickly, suggesting that the underlying process is viscoelastic rather than viscoplastic.

In order to explore the viscoelasticity further, relaxation tests were performed at different strain levels as shown in Figure 4.5b. Here, the polyethylene strip was first stretched at a strain rate of 0.0169 s^{-1} to a specific strain level and then held at this strain level while the relaxation of the nominal stress was measured. In Figure 4.5b the stress is normalized by the peak stress at each strain level. The normalized stress relaxation curves are similar to typical viscoelastic relaxation in polymers; however, the fact that they do not collapse onto a single curve indicates that nonlinear viscoelasticity may be important.

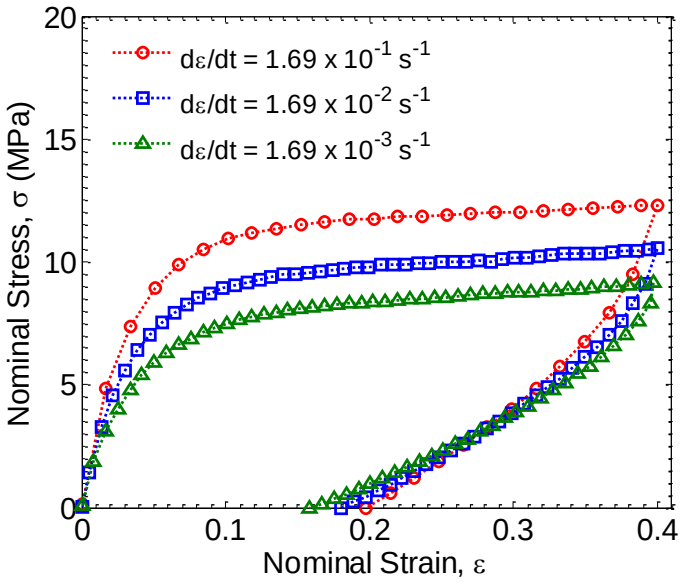

(a)

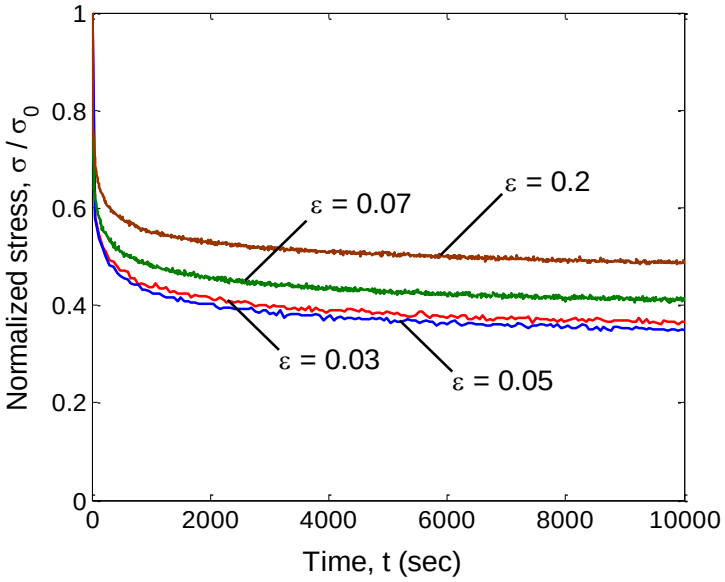

(b)

Figure 4.5: (a) Nominal stress-strain diagrams for polyethylene under uniaxial tension at different strain rates; (b) Normalized stress relaxation curves at different strain levels.

4.2 Clamped-ends Stretching

Figure 4.6 shows optical images and the wrinkle profiles of the polyethylene sheet stretched to different nominal strain levels. Referring to Figure 1.8a, the nominal strain is defined as $\varepsilon = \delta/L_0$, where $\delta = L - L_0$ is the end displacement. The optical image shows only a part of the sheet specimen, showing the speckle pattern at the mid-section of the sheet. The wrinkle profiles were obtained from the out-of-plane displacement (u_z) measured by the 3D-DIC technique along one line across the width of the sheet. It is noticed that the sheet was not perfectly flat at zero strain even after the heat treatment. However, these initial undulations were partly flattened out once a small tensile strain was applied. Subsequently, stretch-induced wrinkles form near the center of the sheet, with a profile that appears to be largely independent of the initial undulations. Similar wrinkle profiles were obtained for two different strain rates ($d\varepsilon/dt$ = 0.00169 s^{-1} and 0.0169 s^{-1}); Figure 4.7 shows the wrinkle profile for sheet when stretched at 0.0169 s^{-1}.

a. Number of Wrinkles

From all the wrinkle profiles shown in Figures 4.6 & 4.7, it is observed that the number of wrinkles across the width of the specimen remains unchanged with increasing strain; only the amplitude changes. This behavior is in line with the hyperelastic model predictions in Chapter 3, but in contradiction to the results reported by Puntel et al. (2011) and Kim et al. (2012).

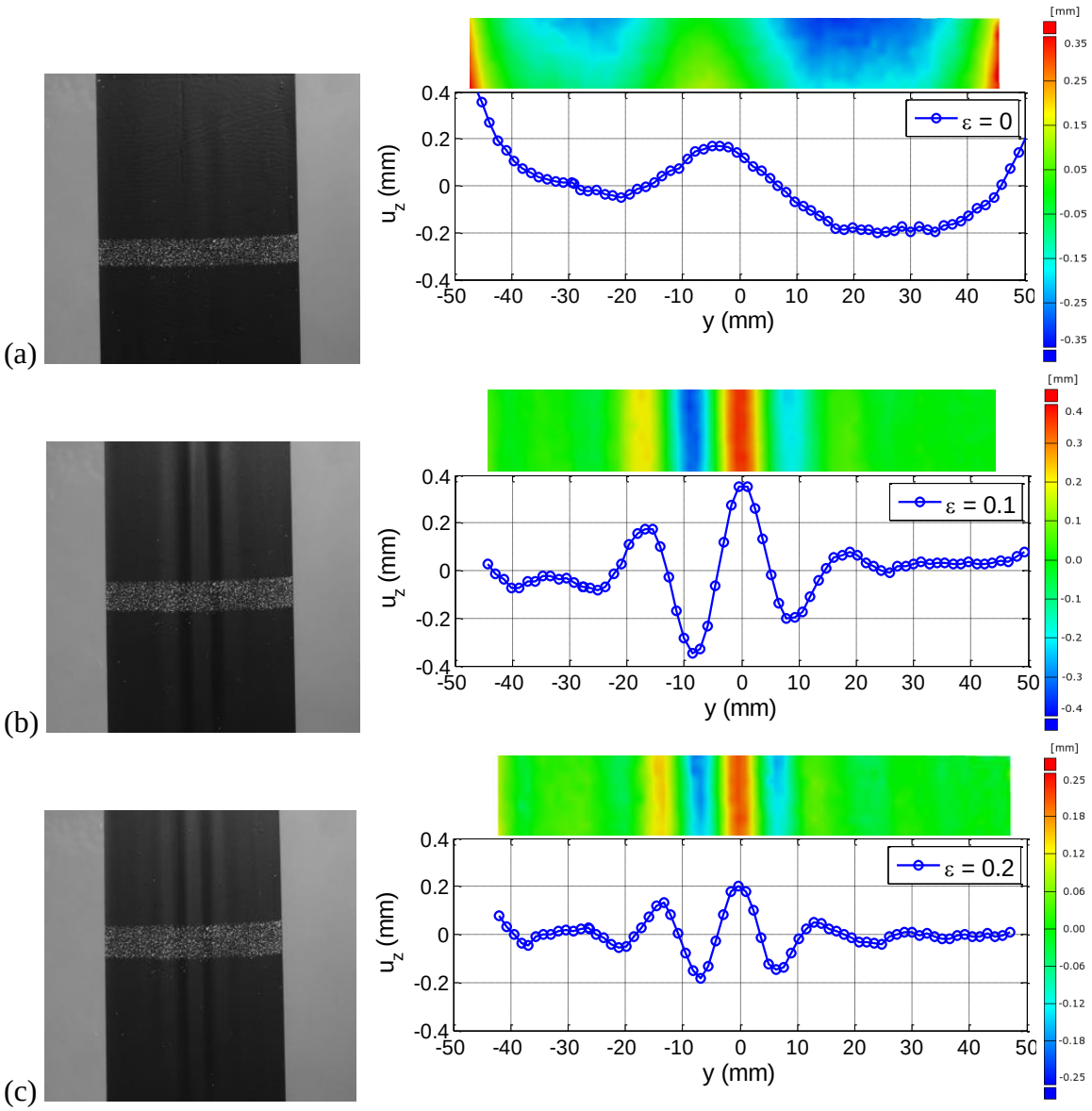

Figure 4.6: Shape of wrinkles in a clamped polyethylene sheet with in-plane (α) and out-of-plane (β) aspect ratio of 2.5 and 1000, respectively, as a function of nominal strain when stretched at strain rate of $d\varepsilon/dt$ = 0.00169 s^{-1}. The nominal strain is, (a) ε = 0%; (b) ε = 10%; (c) ε = 20%; (d) ε = 30%; (e) ε = 40%. In each figure, on the left are the optical images of the sheet at the corresponding strains, while the colored contour shows the out-of-plane deformation of the sheet marked with the speckle pattern.

(d)

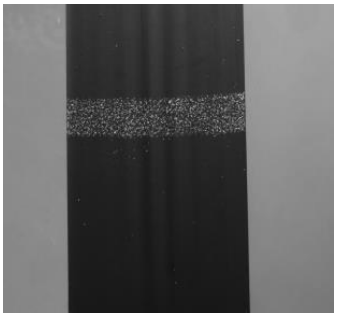

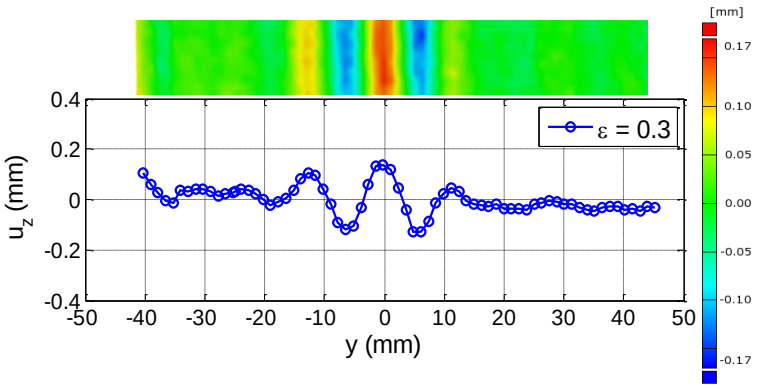

(e)

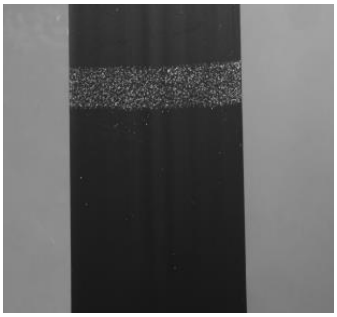

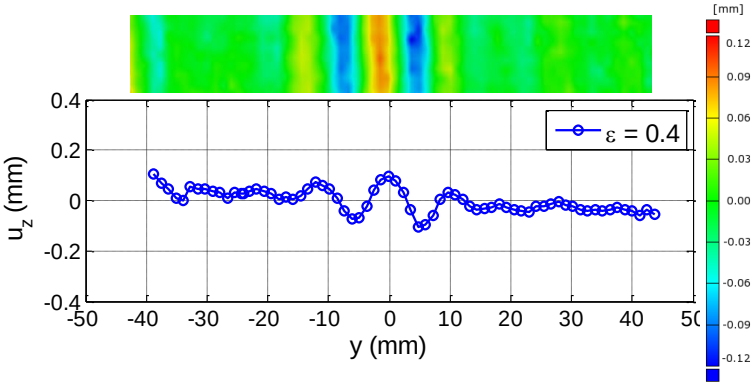

Figure 4.6: cont.

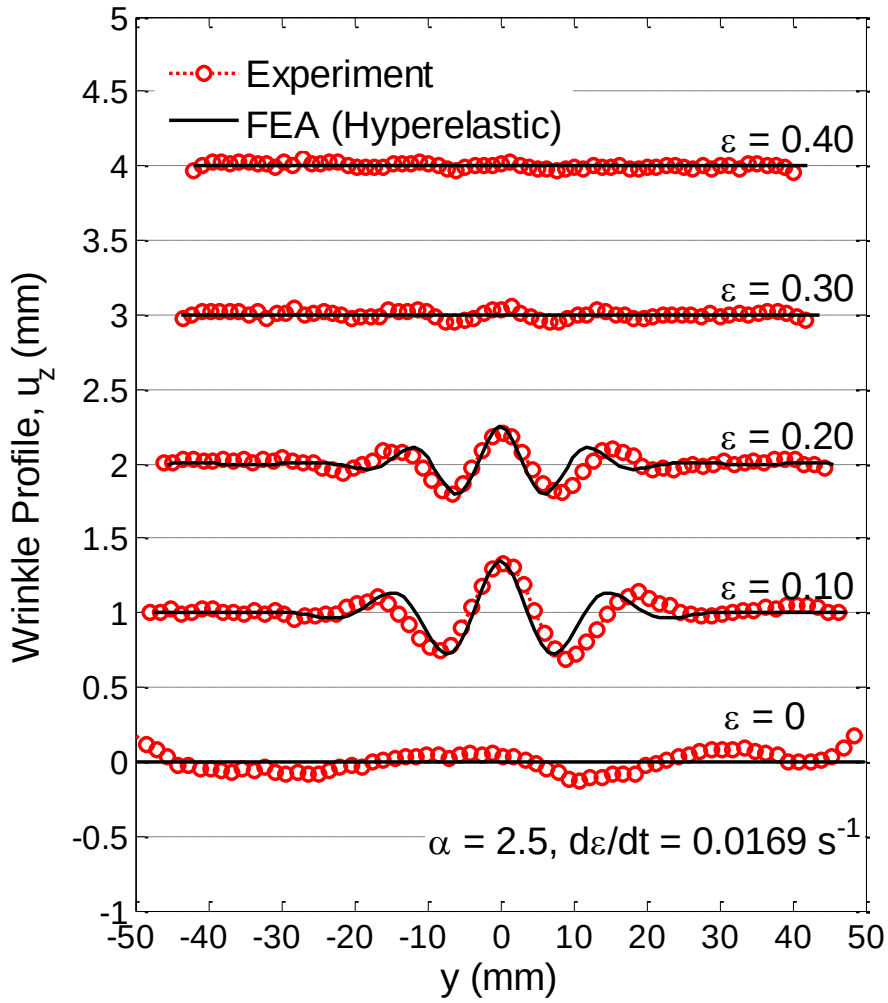

Figure 4.7: Wrinkle profile in a polyethylene sheet at the mid-section when stretched with clamped ends with in-plane (α) and out-of-plane (β) aspect ratio of 2.5 and 1000, respectively, and strain rate of $d\varepsilon/dt$ = 0.0169 s^{-1}, in comparison to a non-linear elastic material response found numerically.

b. Wrinkle Amplitude

The wrinkle amplitude is defined as $A = [\max(u_z) - \min(u_z)]/2$ and plotted as a function of the nominal strain in Figure 4.8 for two different strain rates. Since the

framing rate of the larger strain-rate has one-tenth of the total images of the test at the smaller strain rate. However, the trends in the wrinkle amplitude variation with the nominal strain are similar. First, due to the initial wrinkles, the amplitude decreases, but then around $\varepsilon \sim 0.04$, '*A'* begins to increase sharply. Due to the initial undulations, the critical strain for onset of stretch-induced wrinkling cannot be determined accurately. Approximately, the critical strain may be estimated as the strain when the wrinkle amplitude starts increasing, which is around 3-5%, and compares closely with the previous predictions of finite element analyses (Zheng, 2009; Nayyar et al., 2011). Beyond the onset of wrinkling, the amplitude increases sharply with strain and attains a peak at $\varepsilon \sim 0.12$ before decreasing gradually but not vanishing as $\varepsilon \rightarrow 0.4$. A slight rate dependence can be observed with the amplitude decreasing with increasing strain-rate,

Figure 4.9 shows the wrinkle response in a sheet with in-plane aspect ratio, $\alpha = 2$. Figures 4.9a and 4.9b shows the wrinkle profile of the sheet when stretched at a strain rate of 0.00169 s^{-1} and 0.0169 s^{-1}. Figure 4.9c, plots the amplitude as a function of nominal strain. It is observed that the wrinkle response in this case is qualitatively similar to the previous case ($\alpha = 2.5$). In all these experimental results (for $\alpha = 2.5$ and $\alpha = 2$), the wrinkle amplitude first increased with the nominal strain after flattening of the initial undulations, reached a peak at around 10% strain and then decreased with further increasing strain. Note that in this type of instability, in which the applied load is tensile, the force-displacement curve does not show any critical point that represents the onset of buckling. Figure 4.10 shows the load-displacement curves for an end-clamped stretching of a sheet with in-plane aspect ratio, $\alpha = 2.5$ corresponding to the two cases shown in

Figure 4.8. As seen from this figure, the load-elongation curve increases monotonically through the onset of wrinkling. For comparison, we plot in Figures 4.8 and 4.9 the wrinkle amplitude predicted by the post-buckling finite element simulation of a hyperelastic sheet in the previous chapter. The experimental data agree qualitatively with the numerical simulations, but a few discrepancies are noticeable. First, due to the initial undulations in the specimens, the critical strain for the onset of wrinkling predicted in the simulations could not be clearly identified in the experiments. Second, the numerical simulation underestimates the peak wrinkle amplitude; this becomes even more pronounced for the case when $\alpha = 2$. Thirdly, the wrinkle amplitude reaches its peak at relatively smaller strains in numerical simulations. Finally and most remarkably, contrary to the numerical simulations, the wrinkle amplitude did not go down to zero at large strains in the experiments. The numerical simulations predicted that the stretch-induced wrinkling is completely eliminated beyond a moderately large strain (~ 30% for $\alpha = 2.5$, ~27% for $\alpha = 2$) for a hyperelastic thin sheet. However, in the experiments the wrinkles remained observable up to 40% strain, the largest strain level that was examined. Furthermore, the residual wrinkle amplitude appears to be rate dependent.

Overall, the wrinkle response with strain is found to be qualitatively similar to that predicted in the previous chapter with the hyperelastic model and by Zheng (2009). The discrepancies between the experiments and the simulations must arise from the material model used in the simulations, for example, polyethylene exhibits nonlinear strain rate dependent response (modeled either with a viscoelastic or viscoplastic model) that has not been taken into account. We will examine this in the next chapter.

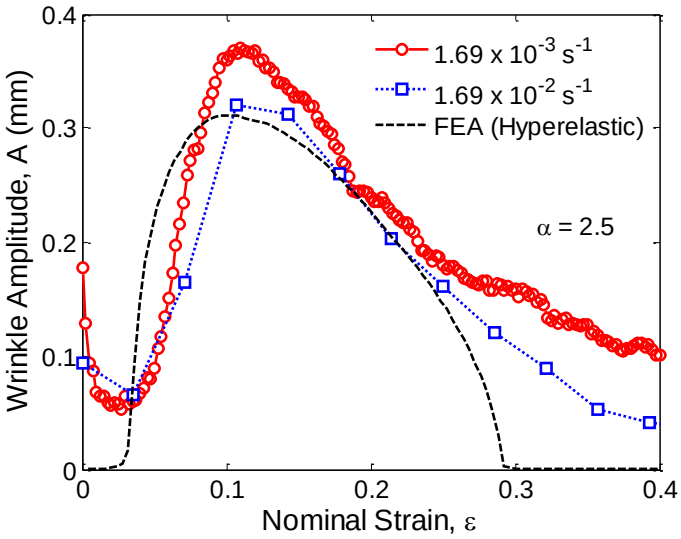

Figure 4.8: Amplitude-strain response at different strain rates in comparison to a non-linear elastic material response found numerically (Chapter 3) under clamped-ends stretching response of a polyethylene sheet with in-plane, α = 2.5.

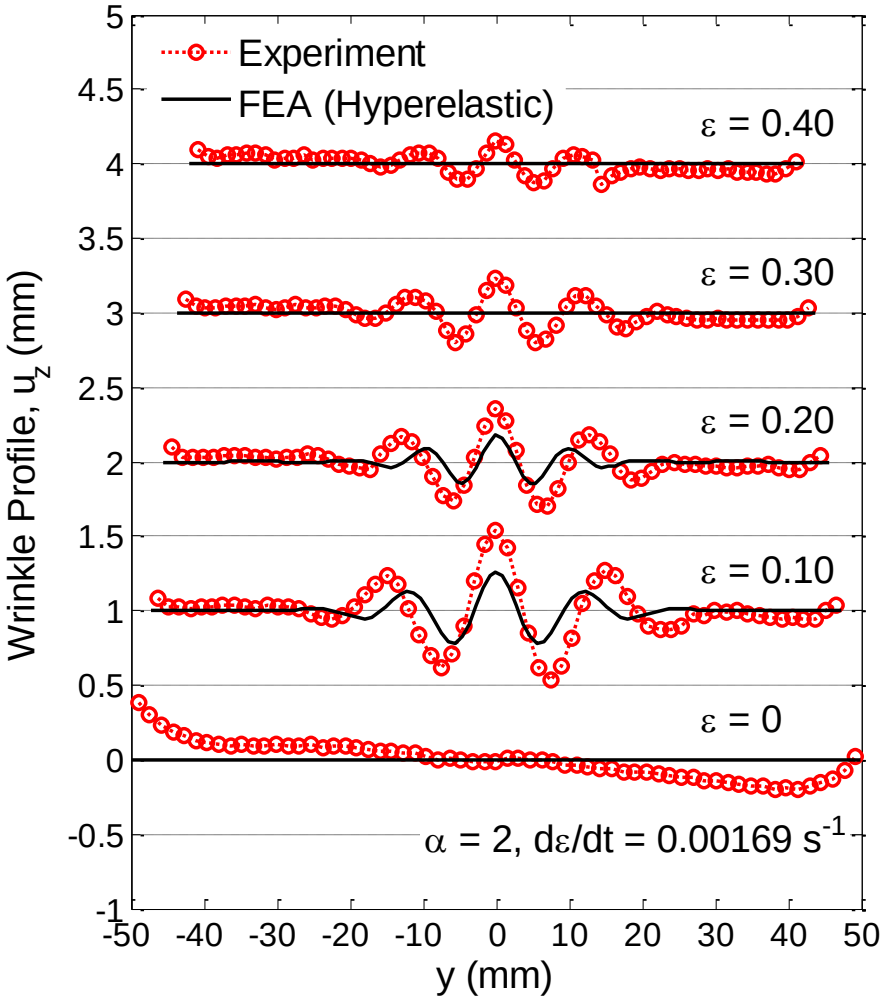

(a)

Figure 4.9: Wrinkle profile in a polyethylene sheet at the mid-section when stretched with clamped ends with in-plane (α) and out-of-plane (β) aspect ratio of 2 and 1000 respectively at strain rate of: (a) $d\varepsilon/dt$ = 0.00169 s^{-1}; (b) $d\varepsilon/dt$ = 0.0169 s^{-1}; (c) Amplitude-strain response at different strain rates for a polyethylene sheet with in-plane aspect ratio, α = 2. For comparison, the response of a non-linear elastic material found numerically is also shown.

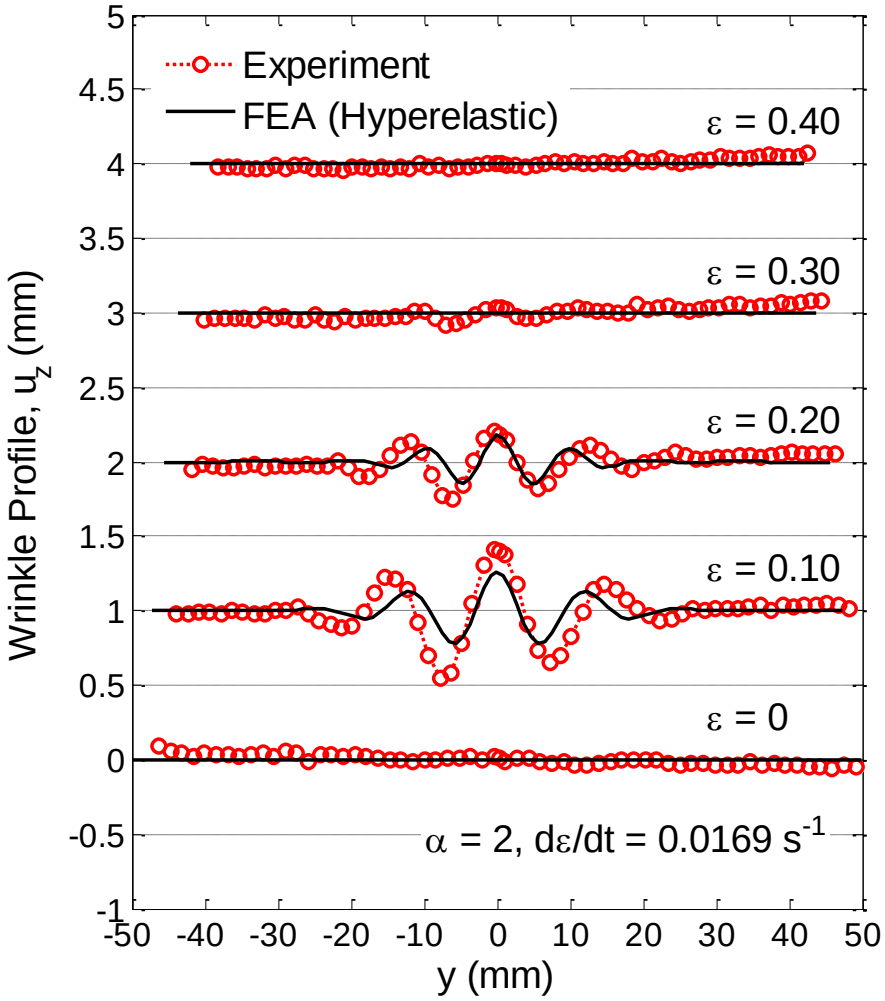

(b)

Figure 4.9: cont.

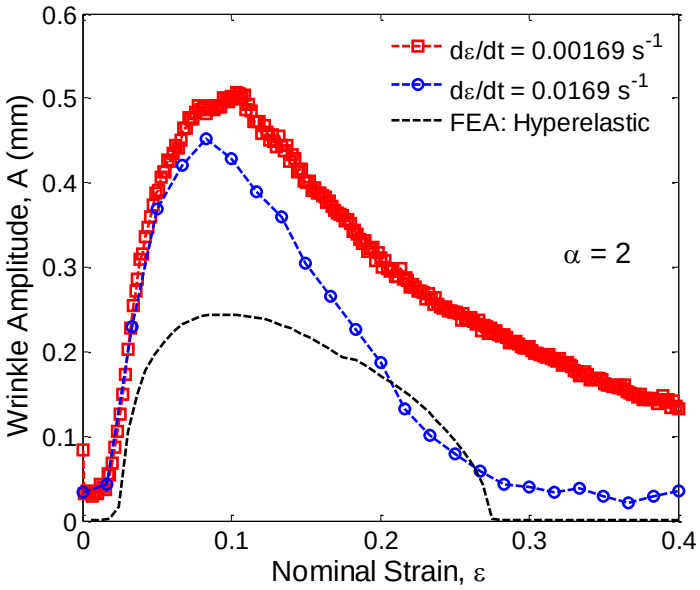

(c)

Figure 4.9: cont.

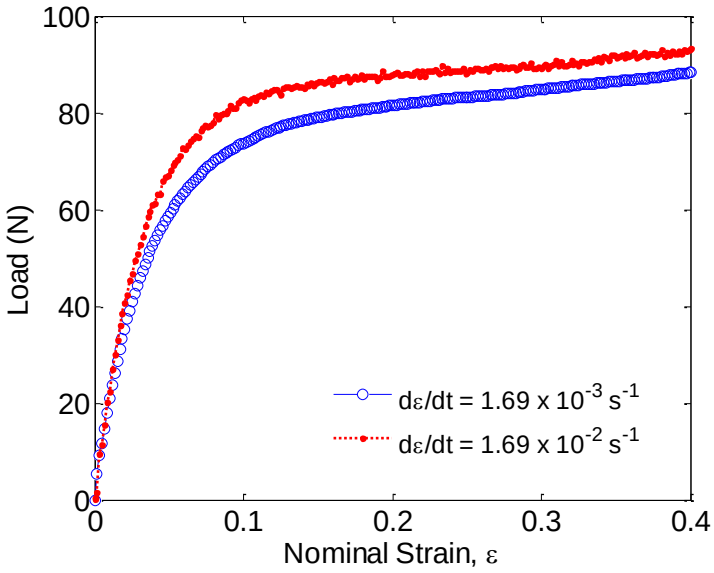

Figure 4.10: Nominal force-displacement relation at different strain rates for a clamped-ended stretching response of a polyethylene sheet with in-plane (α) and out-of-plane (β) aspect ratio of 2.5 and 1000, respectively.

For comparison, the amplitude-strain response at two different strain rates for the two aspect ratios, α = 2 and α = 2.5, are shown together in Figure 4.11. It is noticed that for both the aspect ratios, the residual wrinkle amplitude that occurs at relatively large strains, is larger at slower strain rates. Also, the peak wrinkle amplitude is higher at the slower strain rates.

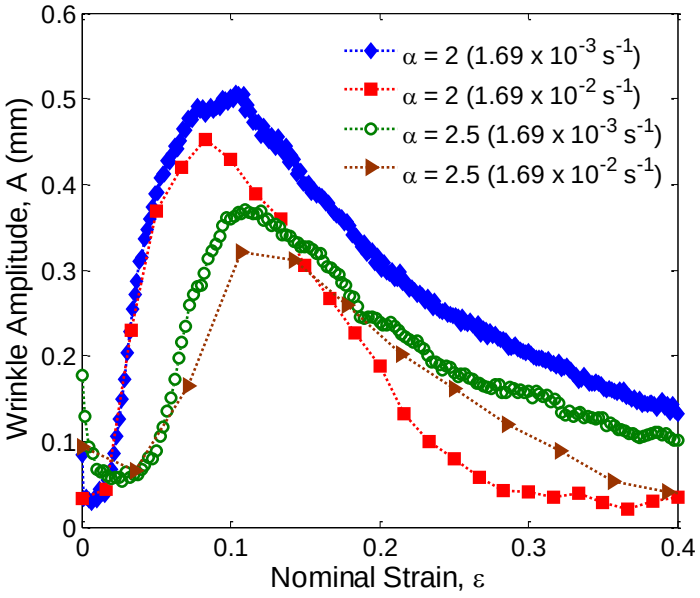

Figure 4.11: Comparison of amplitude-strain response for the two aspect ratios, α = 2 and α = 2.5, when stretched at two different strain rates.

c. Wrinkle Wavelength

The wavelength of the wrinkle profile was determined by measuring the distance between the two consecutive troughs around the central peak from Figures. 4.6, 4.7, 4.9a and 4.9b at different strain levels. These are plotted in Figure 4.12. The scaling analysis by Cerda and Mahadevan (2003) as discussed in Chapter 3, is also shown in this figure and is seen to work reasonably well for the experimental data obtained using

polyethylene sheets. The strain rate dependence of the material used does not appear to influence the wavelength. Also, it should be noted that scaling relation is derived for linear elastic materials. Nevertheless, the agreement is quite good.

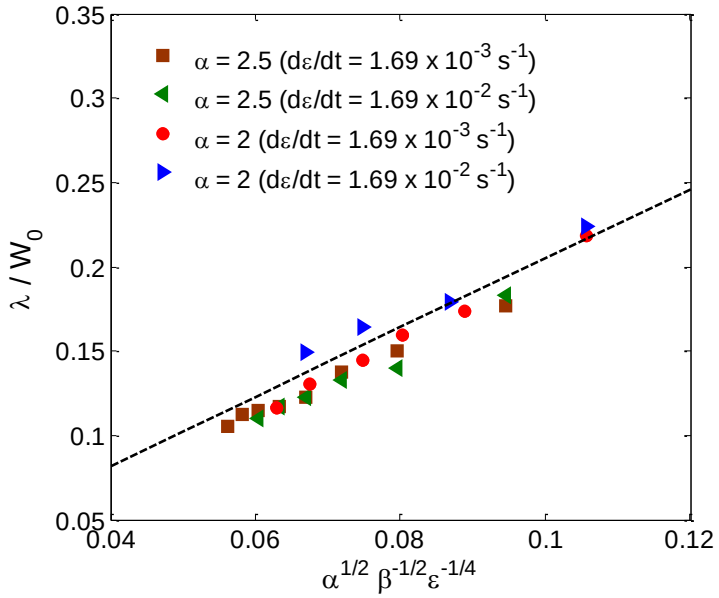

Figure 4.12: Normalized wrinkle wavelength from the experimental data, in comparison with the prediction by a scaling analysis (dashed line).

4.3 Relaxation with Wrinkling

The time-dependent mechanical properties of polyethylene must lead to time-dependent wrinkling behavior of the stretched polyethylene sheets. Another way to examine the strain rate dependent wrinkling discussed in the previous section is to examine the relaxation behavior of the wrinkling. In each test the sheet with in-plane aspect ratio, α = 2.5 was stretched to a specific strain level, ε = 0.08. 0.10, 0.15 and 0.20, at a strain rate of 0.000169 s^{-1} and then held fixed. While the nominal strain is held constant, the sheet is allowed to relax and the stress relaxation is monitored from these

tests. The wrinkle amplitudes are shown in Figures 4.13 – 4.16. The average strains in the x and y directions along the mid-section ($x = L_0/2$) as measured by DIC are also indicated in these figures. It is found that the average strain remains unchanged when the applied nominal strain is held constant. The stress distribution, however, is non-uniform in the wrinkled state and hence relaxes in a complex fashion. Therefore, it is anticipated that the wrinkle amplitude will also exhibit a complex response. This is seen in the results displayed in Figures 4.13 - 4.16. When the strain level during the relaxation experiment is $\varepsilon = 0.08$, the wrinkle amplitude increases initially during the relaxation phase of the experiment while in all the experiments with $\varepsilon \geq 0.10$, the wrinkle amplitude decreases during relaxation. In both cases, the wrinkle amplitude settles down to a steady value after 2000 s of relaxation indicating that the behavior suggests an approach to equilibrium response. This can be further motivated by examining Figures 4.8 and 4.9c where the amplitude of wrinkling during constant strain rate experiment is below the hyperelastic (equilibrium) amplitude when $\varepsilon < \varepsilon_{peak}$ and above the hyperelastic response when $\varepsilon > \varepsilon_{peak}$. This response needs to be examined further through a more appropriate viscoelastic or viscoplastc material model.

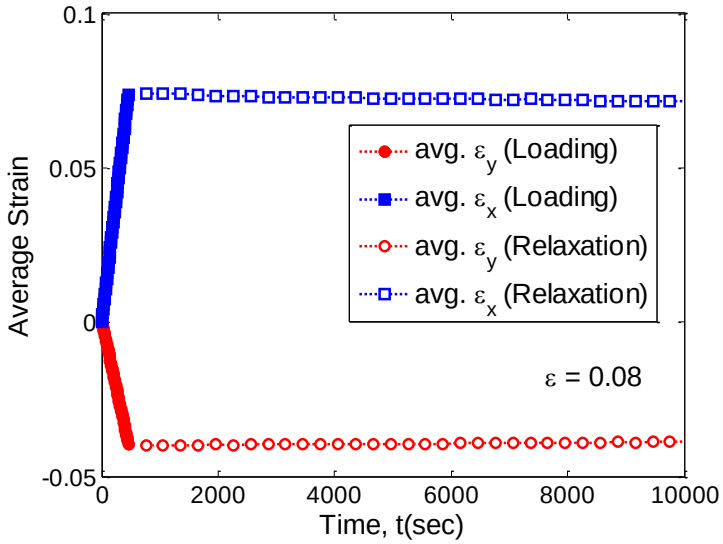

(a)

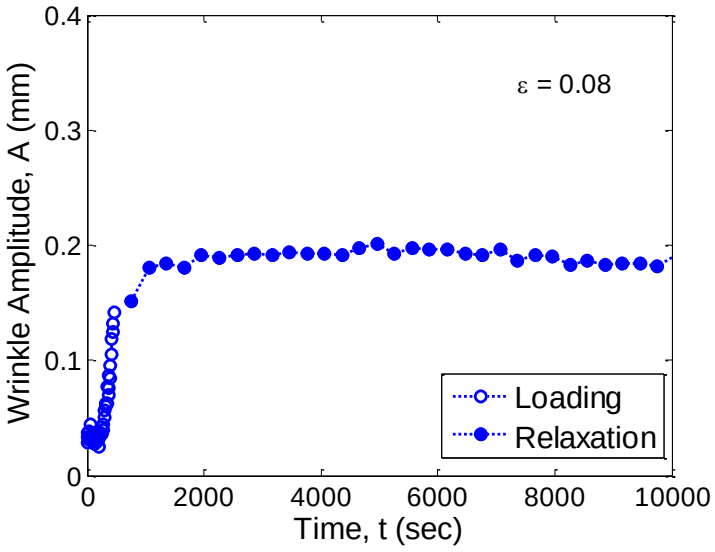

(b)

Figure 4.13: Response of a wrinkled sheet with in-plane aspect ratio, α = 2.5, when the sheet is stretched and relaxation is performed at 8% nominal strain: (a) average strains (ε_x and ε_y) as a function of time, along the mid-section of the sheet ($x = L_0/2$); (b) wrinkle amplitude as a function of time.

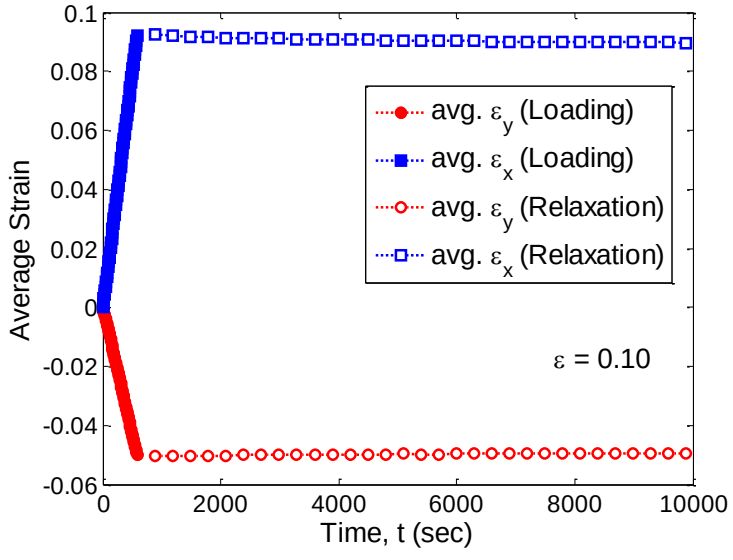

(a)

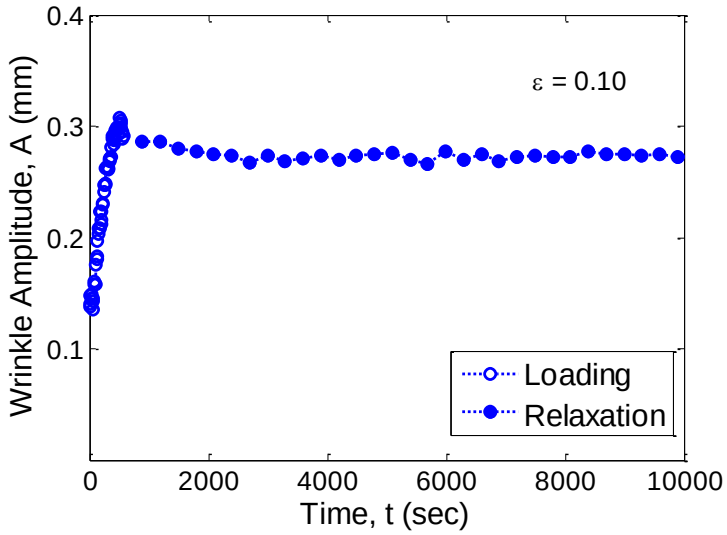

(b)

Figure 4.14: Response of a wrinkled sheet with in-plane aspect ratio, α = 2.5, when the sheet is stretched and relaxation is performed at 10% nominal strain: (a) average strains (ε_x and ε_y) as a function of time, along the mid-section of the sheet ($x = L_0/2$); (b) wrinkle amplitude as a function of time.

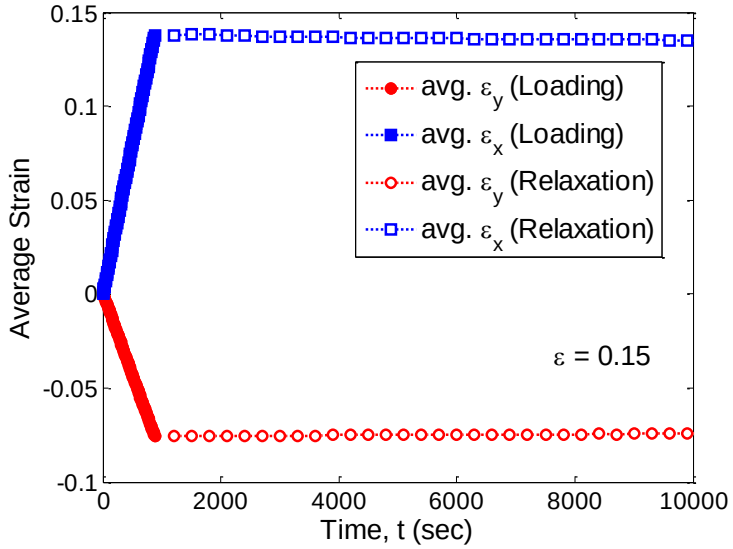

(a)

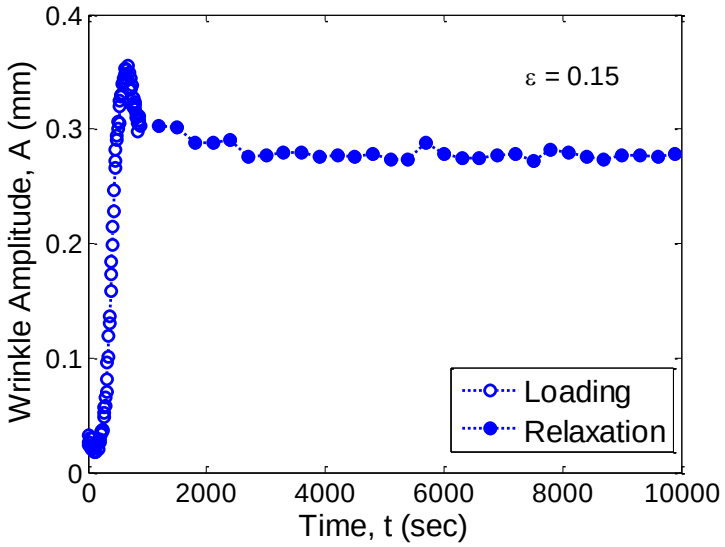

(b)

Figure 4.15: Response of a wrinkled sheet with in-plane aspect ratio, α = 2.5, when the sheet is stretched and relaxation is performed at 15% nominal strain: (a) average strains (ε_x and ε_y) as a function of time, along the mid-section of the sheet ($x = L_0/2$); (b) wrinkle amplitude as a function of time.

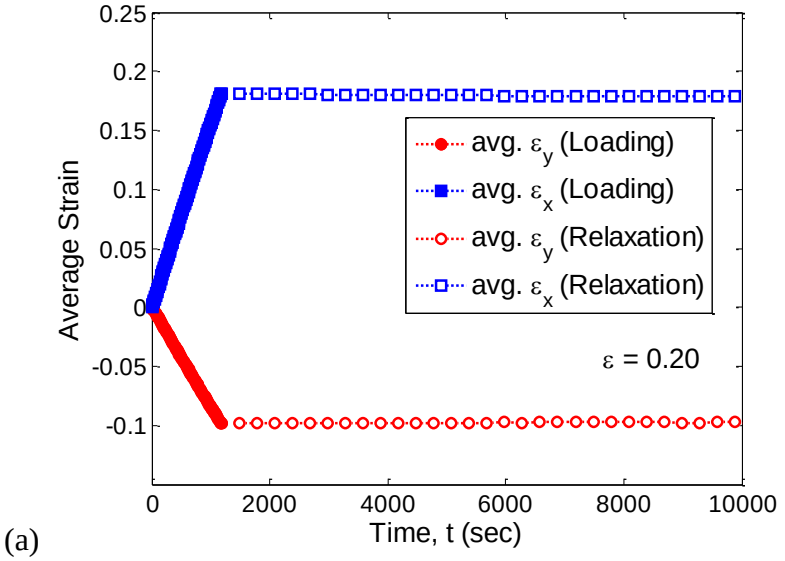

(a)

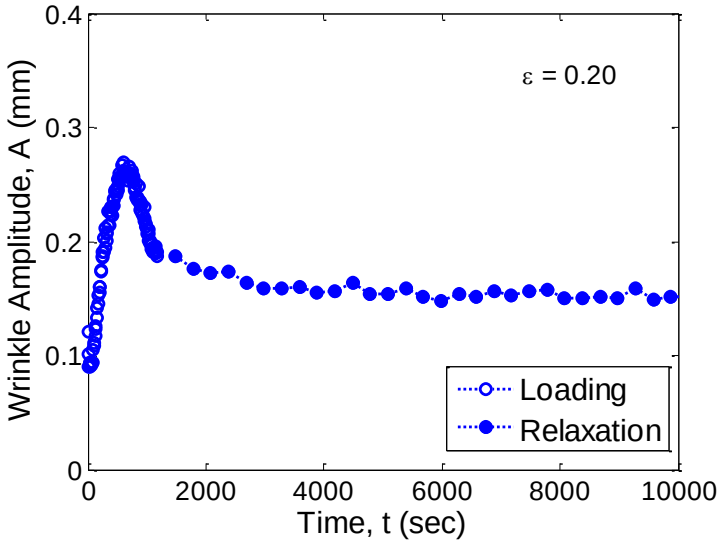

(b)

Figure 4.16: Response of a wrinkled sheet with in-plane aspect ratio, α = 2.5, when the sheet is stretched and relaxation is performed at 20% nominal strain: (a) average strains (ε_x and ε_y) as a function of time, along the mid-section of the sheet ($x = L_0/2$); (b) wrinkle amplitude as a function of time.

4.5 SUMMARY

In this chapter, the stretch-induced wrinkling with clamped ends has been investigated experimentally. The material properties were identified through uniaxial tension experiments at constant strain rate and through relaxation experiments. Wrinkling experiments were performed at two different strain rates and two aspect ratios (α = 2 and α = 2.5). The relaxation response of wrinkled specimen was also examined. It was verified that wavelength scaling relation given by Cerda and Mahadevan (2003) predicts the wrinkle wavelength reasonably well. On the other hand, the wrinkle amplitude scaling relation was found to be in contradiction with the experimental results. It was also found that there are some discrepancies between the non-linear elastic results and experimental results especially at large strains ($\geq$ 20%). The need for a nonlinear viscoelastic or viscoplastic modeling of the response was also established; this will be considered in the next chapter.

CHAPTER 5

Nonlinear Viscoelastic Wrinkling Analysis

5.1 INTRODUCTION

While the experimental measurements in Chapter 4 agree fairly well with the numerical simulations in Chapter 3, discrepancies are noticeable especially at large strains. One of the factors that may cause the discrepancy is the constitutive model of the material used in the simulations. While most previous studies have assumed the sheet material to be elastic [Segedin et al., 1988; Friedl et al., 2000; Cerda et al., 2002; Zheng, 2009; Puntel et al., 2011; Healey et al., 2013], the polyethylene sheet used in the experiments is viscoelastic in nature. In this chapter, stretch-induced wrinkling is studied for viscoelastic thin sheets, in comparison with the experiments presented in Chapter 4. Numerical simulations are performed using ABAQUS with two different viscoelastic constitutive models, the hyper-viscoelastic (HVE) model and the parallel network (PN) nonlinear viscoelastic model. While qualitatively similar results are obtained from both models, the PN model is better suited to capture the rate dependence in the stress and wrinkling behaviors of the polyethylene thin sheets.

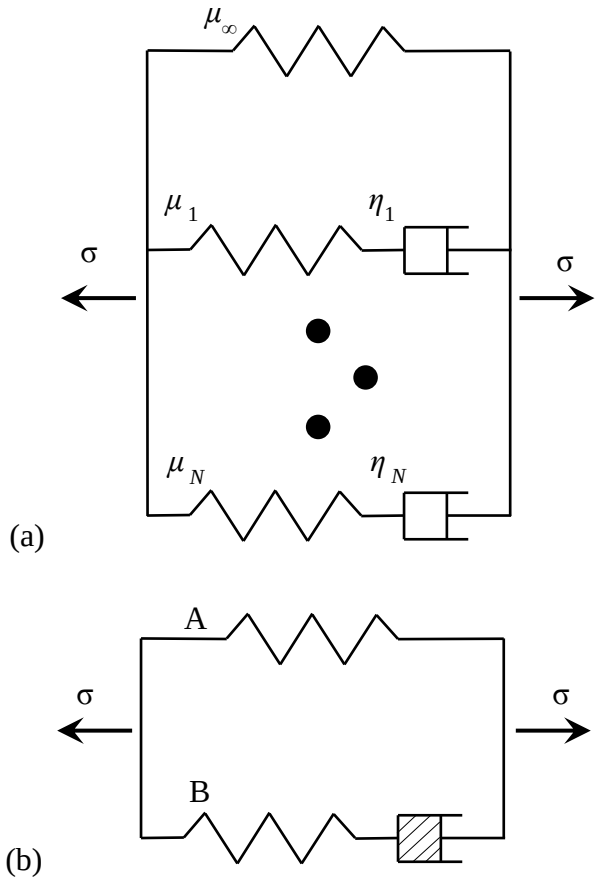

Figure 5.1: Two viscoelastic models represented by mechanical analogs: (a) a hyper-viscoelastic model; (b) a parallel network nonlinear viscoelastic model.

5.2 CONSTITUTIVE MODELS

In this section, we describe the viscoelastic constitutive models used in this chapter. First, a hyper-viscoelastic (HVE) model is described, which is a generalized Maxwell model that incorporates nonlinear geometry associated with large deformation. This model can be represented by a mechanical analog as shown in Figure 5.1(a). In general, the model can have any number of viscoelastic branches parallel to an elastic branch, and each viscoelastic branch defines a time scale, $\tau_i = \eta_i/E_i$ ($i = 1, \ldots N$). The second model

is a parallel network (PN) nonlinear viscoelastic model, which can be represented schematically as shown in Figure 5.1(b). The two branches of the mechanical analog represent two parallel networks of the polymer: network 'A' is hyperelastic and network 'B' is nonlinear viscoelastic. More than one viscoelastic network may be used if necessary.

5.2.1 Hyper-viscoelastic model

The finite-strain viscoelastic model implemented in ABAQUS is a time domain generalization of the hyperelastic constitutive model, hence called hyper-viscoelasticity (HVE). It is also a generalization of linear viscoelasticity to finite deformation, where the instantaneous stress is computed using a hyperelastic strain energy potential function. The standard push-forward transformation is used in the finite-strain formulation to map the stress in the configuration at time t_1 into the configuration at another time t_2. This generalization yields an intrinsically linear viscoelastic behavior in the sense that the dimensionless stress relaxation function is independent of the magnitude of the deformation. In the present study, the incompressible neo-Hookean model is used for the hyperelastic instantaneous stress. For uniaxial tension, the instantaneous Cauchy stress is

$$\sigma_0 = \mu_0 \left(\lambda^2 - \frac{1}{\lambda}\right) \tag{5.1}$$

where μ_0 is the instantaneous shear modulus and $\lambda = 1 + \varepsilon$ is the stretch corresponding to the nominal strain ε. Using the hereditary integral formulation for linear viscoelasticity and applying the standard push-forward operator (Simo, 1987), one obtains the stress in the current configuration:

$$\sigma(t) = \sigma_0(t) + \int_0^t \frac{2\dot{\mu}(s)}{9\mu_0}\left(\bar{\lambda} + \frac{2}{\bar{\lambda}^2}\right)\sigma_0(t-s)ds \tag{5.2}$$

where $\bar{\lambda} = \lambda(t-s)/\lambda(t)$, $\dot{\mu}(t) = d\mu/dt$, and $\mu(t)$ is the time-dependent shear relaxation modulus. Here we have assumed the material to be incompressible. The relaxation modulus is assumed to take the form of a Prony series,

$$\mu(t) = \mu_0 \left(1 - \sum_{i=1}^{N} g_i \left(1 - e^{-\frac{t}{\tau_i}}\right)\right) \tag{5.3}$$

where the parameters μ_0, g_i, and τ_i (i = 1, … N) can be determined by fitting the measured relaxation curves such as those in Figure 4.5b. For stress relaxation at a constant strain, Eq. (5.2) becomes

$$\sigma(t) = \sigma_0 \left(1 - \frac{2}{3}\sum_{i=1}^{N} g_i \left(1 - e^{-\frac{t}{\tau_i}}\right)\right) \tag{5.4}$$

It is found that, with a single viscoelastic branch in Fig. 5.1(a), the HVE model can be used to fit the uniaxial stress-strain response (not for unloading) of polyethylene for each strain rate, as shown in Fig. 5.2. Table 5.1 lists the material parameters obtained by fitting, where the instantaneous shear modulus (μ_0) and the long-term shear modulus, $\mu_\infty = \mu_0 \left(1 - g_1\right)$ are kept constant for the three different strain rates. The time scale τ is varied to fit the uniaxial stress-strain data. As the strain rate increases, the associated time scale decreases and the stress increases. Therefore, the HVE model may be used to simulate the stress-strain behavior of polyethylene at a particular strain rate, but the strain rate dependence has to be accounted for by varying the viscoelastic time scale.

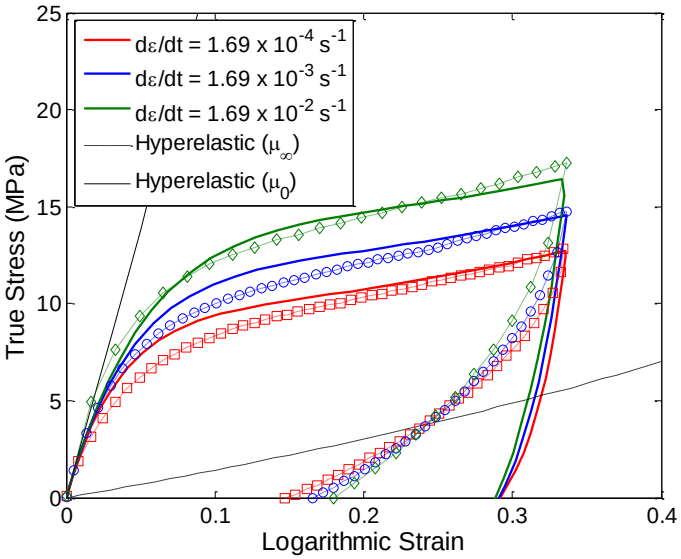

Figure 5.2: Fitting of the uniaxial stress-strain response of polyethylene using the HVE model with different viscoelastic time scales for different strain rates as listed in Table 5.1. The lines represent the simulated results in comparison with the expereimental data represented by the symbols.

Table 5-1: Parameters used to fit the uniaxial stress-strain response of polyethylene at different strain rates with a single viscoelastic branch in the HVE model.

Strain rate $\dot{\varepsilon}$ (s^{-1})	Shear moduli		Relaxation time scale	
	μ_0 (MPa)	μ_∞ (MPa)	τ (s)	$\dot{\varepsilon}\tau$
1.69 x 10^{-4}	90	4.5	200	0.0338
1.69 x 10^{-3}	90	4.5	25	0.0423
1.69 x 10^{-2}	90	4.5	3	0.0507

It is noticed that the nonlinear stress relaxation behavior observed in Figure 4.5(b) cannot be captured by the HVE model. Figure 5.3(a) compares the simulated relaxation response using the three set of parameters (Table 5.1) with the experimental data for stress relaxation at 3% nominal strain. Evidently, a single viscoelastic branch is

insufficient to capture the relaxation behavior over a long time. It is possible to fit the relaxation response by using more than one viscoelastic branches (hence more than one time scale) in the HVE model as shown in Fig. 5.3(b). Here we have used a Prony series for the relaxation modulus in Eq. (5.3) with five viscoelastic branches and the parameters as shown in Table 5.2. Note that the time scales used here include the three time scales in Table 5.1 and in addition, one shorter and one longer time scale. Similar fitting can be obtained for the other stress relaxation curves in Fig. 4.5(b), but each with a different set of parameters. In general, it is unlikely that all the relaxation curves could be fitted by using the HVE model with a single set of parameters in the Prony series, due to the intrinsically nonlinear viscoelastic behavior of polyethylene. Equation (5.4) predicts that the normalized stress relaxation $\sigma(t)/\sigma_0$ would be independent of the imposed nominal strain, a characteristic of linear viscoelasticity. Moreover, the HVE model with five viscoelastic branches does not produce the uniaxial stress-strain response observed in experiments, as shown in Figure 5.3(c). Therefore it is concluded that the rate-dependent stress-strain behavior of polyethylene cannot be modeled by the HVE model in general. Approximately, for a specific strain rate, the stress-strain behavior under monotonic loading (without unloading) may be simulated by using a single time scale in the HVE model (see Fig. 5.2).

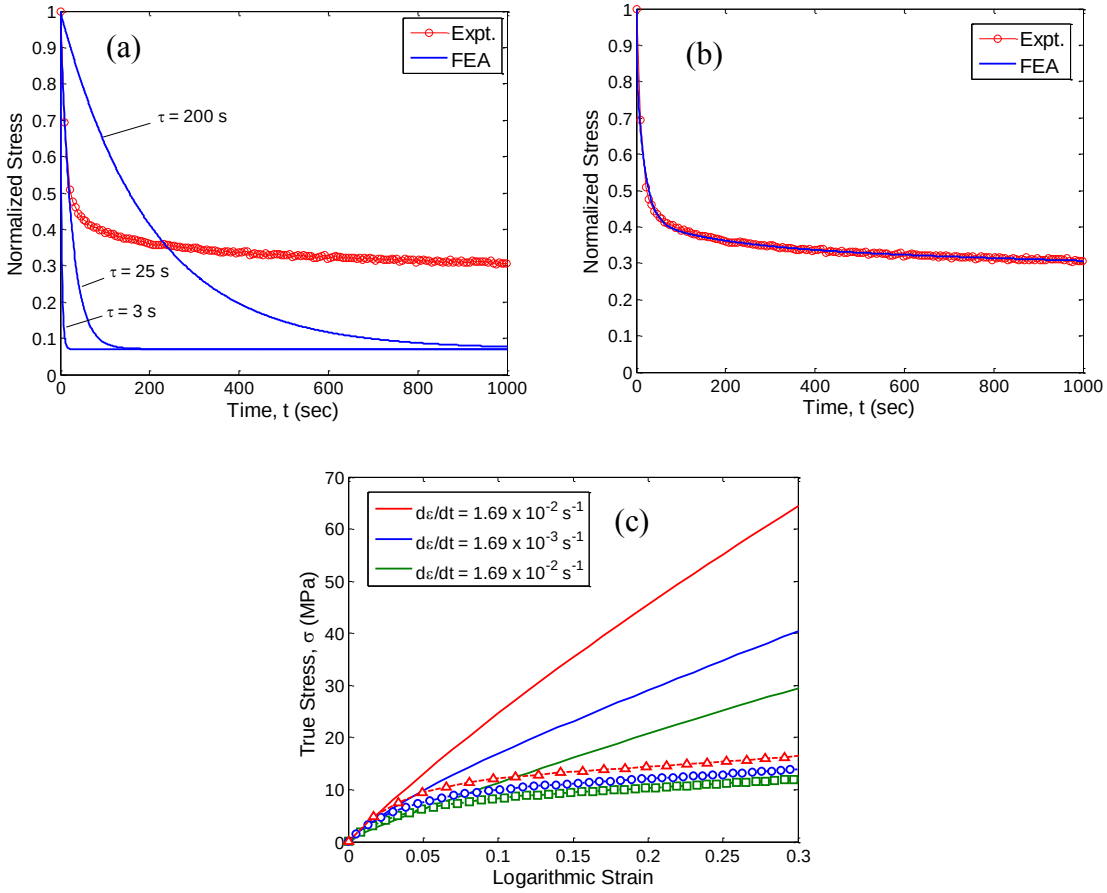

Figure 5.3: Comparison of normalized stress relaxation of polyethylene at 3% nominal strain between measurements and the simulated responses using the HVE model, with one viscoelastic branch in (a) and five viscoelastic branches in (b). (c) Comparison of uniaxial stress-strain behavior at different strain rates between measurements and simulated responses using the HVE model with five viscoelastic branches.

Table 5-2: Parameters used to fit the stress relaxation response of polyethylene with five viscoelastic branches in the HVE model.

Shear moduli		Relaxation time scale (s)	
μ_0 (MPa)	90		
g_1	0.00093	τ_1	0.3
g_2	0.1547	τ_2	3
g_3	0.4259	τ_3	25
g_4	0.0805	τ_4	200
g_5	0.337	τ_5	7164

5.2.2 Parallel network nonlinear viscoelastic model

The second viscoelastic material model used in the present study is a parallel network (PN) model as illustrated in Figure 5.1(b), with an intrinsically nonlinear viscoelastic network. In this model, the total Cauchy stress is the sum of the stresses in the networks 'A' and 'B':

$$\boldsymbol{\sigma} = \boldsymbol{\sigma}_A + \boldsymbol{\sigma}_B \tag{5.5}$$

Under a global deformation gradient $\boldsymbol{F}$, the deformation gradients for the parallel networks are equal: $\boldsymbol{F}_A = \boldsymbol{F}_B = \boldsymbol{F}$. While the network A is completely elastic, the viscoelastic deformation in the network B is modeled by the multiplicative split of the total deformation gradient into elastic ($\boldsymbol{F}_B^e$) and creep ($\boldsymbol{F}_B^{cr}$) parts, namely

$$\boldsymbol{F}_B = \boldsymbol{F}_B^e \boldsymbol{F}_B^{cr} \tag{5.6}$$

For large deformation, the elastic response of each network is specified by using a hyperelastic material model. For an incompressible Neo-Hookean model, the Cauchy stress under uniaxial tension can be written as,

$$\sigma = \mu\left(\lambda^2 - \frac{1}{\lambda}\right) \tag{5.7}$$

where μ is the initial shear modulus and λ is the elastic stretch. For the parallel network model, the total Cauchy stress under uniaxial tension is

$$\sigma = \mu_A\left(\lambda_A^2 - \frac{1}{\lambda_A}\right) + \mu_B\left({\lambda_B^e}^2 - \frac{1}{\lambda_B^e}\right) \tag{5.8}$$

where $\lambda_A = \lambda$, $\lambda_B^e = \lambda/\lambda_B^{cr}$, μ_A and μ_B are the elastic shear modulus of networks A and B, respectively.

The viscous part of the network B is constitutively described by the flow rule,

$$\boldsymbol{D}_B^{cr} = \dot{\bar{\varepsilon}}^{cr} \frac{\partial G^{cr}(\boldsymbol{\sigma}_B)}{\partial \boldsymbol{\sigma}_B} \tag{5.9}$$

where $\boldsymbol{D}_B^{cr}$ is the symmetric part of the velocity gradient expressed in the current configuration ($\boldsymbol{D}_B^{cr} = \frac{1}{2}\left(\boldsymbol{L}_B^{cr} + \boldsymbol{L}_B^{cr^T}\right)$ and $\boldsymbol{L}_B^{cr} = \boldsymbol{F}_B^e \dot{\boldsymbol{F}}_B^{cr} \boldsymbol{F}_B^{cr^{-1}} \boldsymbol{F}_B^{e^{-1}}$), $\dot{\bar{\varepsilon}}^{cr}$ is the equivalent creep stain rate, and G^{cr} is the creep potential. In this model, the creep potential is assumed to be the equivalent deviatoric Cauchy stress:

$$G^{cr}(\boldsymbol{\sigma_B}) = \bar{q}_B = \sqrt{\frac{3}{2}\boldsymbol{s}_B : \boldsymbol{s}_B} \tag{5.10}$$

where $\boldsymbol{s}_B = \boldsymbol{\sigma_B} - \frac{1}{3} tr(\sigma_B)\boldsymbol{I}$. Inserting (5.10) into (5.9), the flow rule takes the form

$$\boldsymbol{D}_B^{cr} = \frac{3\dot{\bar{\varepsilon}}^{cr}}{2\bar{q}_B}\boldsymbol{s}_B \tag{5.11}$$

The equivalent creep stain rate $\dot{\bar{\varepsilon}}^{cr}$ is described by a power-law strain hardening model:

$$\dot{\bar{\varepsilon}}^{cr} = (B\bar{q}_B^n[(m+1)\bar{\varepsilon}^{cr}]^m)^{\frac{1}{m+1}} \tag{5.12}$$

where $\bar{\varepsilon}^{cr}$ is the equivalent creep strain, and B, m and n are the material parameters ($-1 < m \leq 0$ and B, $n > 0$). Following the small-strain creep formulation, the equivalent creep strain rate is defined as

$$\dot{\bar{\varepsilon}}^{cr} = \sqrt{\frac{2}{3}\boldsymbol{D}_B^{cr} : \boldsymbol{D}_B^{cr}} \tag{5.13}$$

and the equivalent creep strain is then obtained by integrating (5.13) with respect to time.

For the case of uniaxial tension, the flow rule in Eq. (5.11) can be reduced to a scalar form:

$$\frac{\dot{\lambda}_B^{cr}}{\lambda_B^{cr}} = \dot{\bar{\varepsilon}}^{cr} = (B\sigma_B^n[(m+1)\bar{\varepsilon}^{cr}]^m)^{\frac{1}{m+1}} \tag{5.14}$$

By integrating the first part of Eq. (5.14), we obtain the equivalent creep strain in terms of the axial stretch: $\bar{\varepsilon}^{cr} = ln(\lambda_B^{cr})$. The rate equation in (5.14) can then be re-written as

$$\dot{\lambda}_B^{cr} = \lambda_B^{cr}(B\sigma_B^n[(m+1)ln(\lambda_B^{cr})]^m)^{\frac{1}{m+1}} = \bar{B}\lambda_B^{cr}[ln(\lambda_B^{cr})]^{\frac{m}{m+1}}\left[\frac{\sigma_B}{\mu_B}\right]^{\frac{n}{m+1}} \quad (5.15)$$

where $\sigma_B = \mu_B\left(\left(\frac{\lambda}{\lambda_B^{cr}}\right)^2 - \frac{\lambda_B^{cr}}{\lambda}\right)$ and $\bar{B} = (B\mu_B^n(m+1)^m)^{\frac{1}{m+1}}$. Thus, by integrating Eq. (5.15), λ_B^{cr} can be obtained as a function of time, with the initial condition, λ_B^{cr} = 1 at *t* = 0. By Eq. (5.8), the total stress is obtained as a function of time for the case of uniaxial tension:

$$\sigma = \mu_A\left(\lambda^2 - \frac{1}{\lambda}\right) + \mu_B\left(\left(\frac{\lambda}{\lambda_B^{cr}}\right)^2 - \frac{\lambda_B^{cr}}{\lambda}\right) \quad (5.16)$$

where $\lambda = \lambda(t)$ represents the loading history (displacement control).

Consider two limiting cases using the PN model. First, when the applied strain rate $\dot{\lambda} \to \infty$, the creep strain approaches zero ($\lambda_B^{cr} \to 1$), and Eq. (5.16) becomes

$$\sigma = (\mu_A + \mu_B)\left(\lambda^2 - \frac{1}{\lambda}\right) \quad (5.17)$$

which corresponds to the elastic limit with the instantaneous shear modulus $\mu_0 = \mu_A + \mu_B$. Second, when the strain rate $\dot{\lambda} \to 0$, the creep strain in network B approaches the total strain ($\lambda_B^{cr} \to \lambda$), and Eq. (5.16) becomes

$$\sigma = \mu_A\left(\lambda_A^2 - \frac{1}{\lambda_A}\right) \quad (5.18)$$

which corresponds to the long term elastic limit ($\mu_\infty = \mu_A$). For a uniaxial tension test with a finite strain rate, the viscoelastic stress-strain behavior by the PN model is bound by the two elastic limits with nonlinear rate dependence.

To find the material parameters in the PN model (μ_A, μ_B, B, m and n), the stress-strain curves of polyethylene measured by the uniaxial tension tests are used. First, the instantaneous elastic modulus of the PN model can be obtained by measuring the slope of the stress-strain curves at the early stage. As shown in Figure 5.4, the initial slope ($\varepsilon \rightarrow 0$) of the stress-strain curves yields the instantaneous modulus, $\mu_0 = \mu_A + \mu_B = 90$ MPa. Next, we estimate the long-term elastic modulus by the slope at relative large strains (> 20%), which yields $\mu_A = 4.5$ MPa. Note that both the instantaneous and long-term elastic moduli are the same as those in Table 5.1 for the HVE model. The other parameters in the PN model are associated with the nonlinear viscoelastic response and are determined by fitting the numerical results with the experimental measurements as shown in Figure 5.4. A three-dimensional (3D) finite-element model in ABAQUS is used to simulate the stress-strain behavior. By an iterative approach, the viscoelastic parameters are obtained as listed in Table 5.3. It is noted that the PN model predicts nearly linear unloading, differing significantly from the experimental measurements.

Table 5-3: Material parameters used to fit the uniaxial tension stress-strain response of polyethylene with the PN nonlinear viscoelastic model.

μ_A	4.5 MPa
μ_B	85.5 MPa
B	1.3×10^{-7} MPa^{-n} $s^{-(m+1)}$
n	5.12
m	-0.465

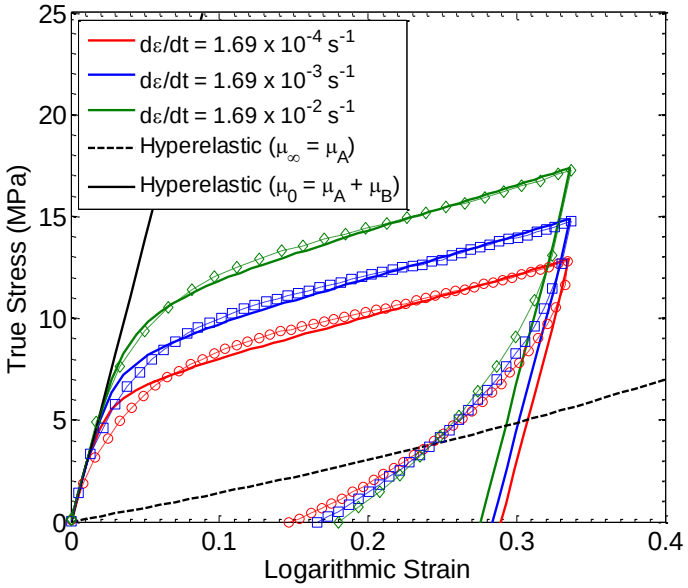

Figure 5.4: Comparison of uniaxial stress-strain behavior of polyethylene measured at different strain rates with the parallel network nonlinear viscoelastic model using the parameters in Table 5.3.

To simulate the stress relaxation response under uniaxial tension, we consider a constant total stretch, $\lambda = \lambda_0$, and calculate the axial stress, σ, as a function of time from Eq. (5.16). At t = 0, we have $\lambda = \lambda_0$ and $\lambda_B^{cr} = 1$ so that $\sigma = \sigma_0 = (\mu_A + \mu_B)\left(\lambda_0^2 - \frac{1}{\lambda_0}\right)$. As $t \to \infty$, we have $\lambda = \lambda_0$ and $\lambda_B^{cr} \to \lambda_0$ so that $\sigma = \sigma_\infty = \mu_A\left(\lambda_0^2 - \frac{1}{\lambda_0}\right)$. In between, the nonlinear viscoelastic relaxation depends on the applied stretch, which can be obtained by numerical integration of (5.15) and (5.16). Figure 5.5 shows the relaxation response simulated using the material parameters in Table 5.3, in comparison with the relaxation response of the HVE model. As discussed earlier, the normalized stress relaxation of the HVE model is independent of the applied strain, whereas the PN model predicts a

nonlinear viscoelastic behavior with the normalized stress relaxation depending on the applied strain.

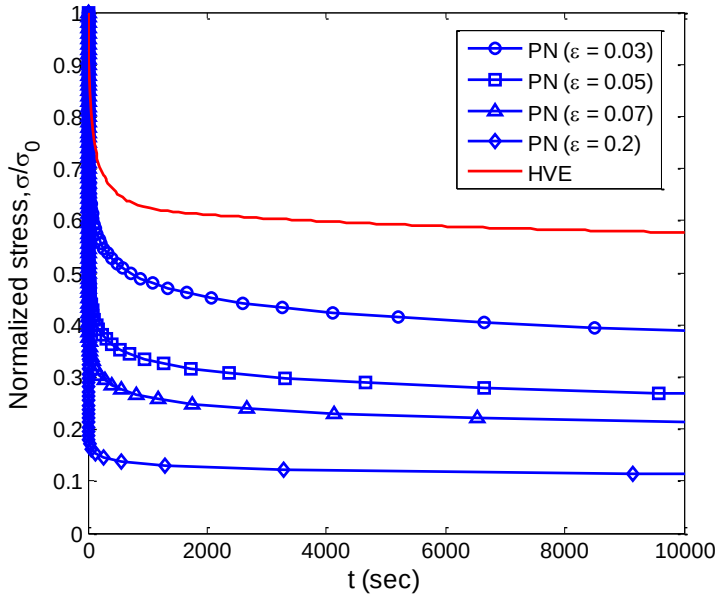

Figure 5.5: Comparison of normalized stress relaxation between the HVE model and the PN model.

In experiments, however, the strain was not applied instantaneously. Instead, the polyethylene strip specimen was first stretched at a strain rate of 0.0169 s^{-1} to a specific strain and then held at this strain level for the stress relaxation measurements as shown in Figure 4.5(b). As a result, the stress at the beginning of the relaxation test was lower than the instantaneous elastic stress. A 3D finite element model is employed to simulate the relaxation tests including both the stretching and holding stages. Figure 5.6 shows the simulated relaxation responses, in comparison with the relaxation tests performed on polyethylene at different strain levels. Using the parameters in Table 5.3 for the PN model, the simulated stress relaxation curves are in reasonable agreement with the

experimental measurements. Therefore, the viscoelastic behavior of polyethylene under both the constant strain rate and stress relaxation conditions can be simulated using the PN model with the same set of material parameters. In other words, the nonlinear viscoelastic behavior of polyethylene can be reasonably captured by the PN model except for unloading. For the present study on stretch-induced wrinkling, the effect of unloading is considered to be negligible.

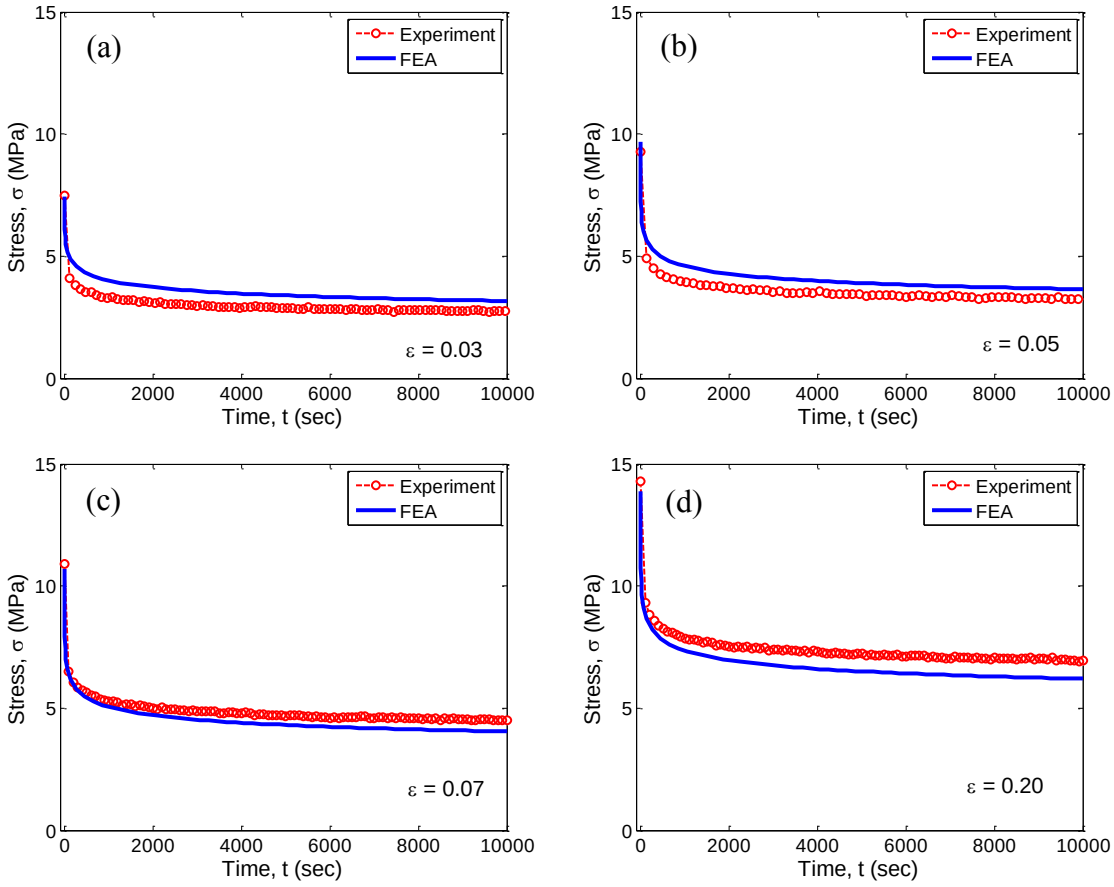

Figure 5.6: Comparison of uniaxial stress relaxation tests performed on polyethylene at different strain levels with numerical simulations using the parallel network nonlinear viscoelastic model.

5.3 STRESS ANALYSIS

As discussed in Chapter 2, previous studies have shown that for a thin elastic sheet subject to uniaxial stretch with clamped ends, compressive stresses develop in the transverse direction due to Poisson's effect and the specific boundary conditions (Friedl et al., 2000; Nayyar et al., 2011). The critical condition for onset of stretch-induced wrinkling depends on both the magnitude and the distribution of compressive stresses. With the non-uniform stress distribution, the effect of viscoelasticity on the development of compressive stresses is nontrivial. In this section, stress analyses performed using both hyper-viscoelastic and PN nonlinear viscoelastic models are discussed. For the specific implementation of these models in ABAQUS, the stress analysis using hyper-viscoelastic model can be performed with the 2D plane-stress elements, whereas 3D elements are required for the PN nonlinear viscoelastic model. From the stress analysis, it is found that the distributions of compressive stress in a viscoelastic thin sheet with clamped-ends are qualitatively similar to those discussed in Section 2.2 for a hyperelastic thin sheet, but the magnitude of the compressive stress depends on the strain rate due to the viscoelastic effect.

5.3.1 Stress Analysis with HVE model

A two-dimensional (2D) finite element analysis is performed using the hyper-viscoelastic material model and quasi-static procedure in ABAQUS/Standard, where the sheet is modeled by quadrilateral plane-stress elements (CPS4R) assuming no wrinkles. Figure 5.7 shows the distribution of transverse compressive stress (σ_y) at 10% nominal strain for a rectangular sheet with the length-to-width ratio α = 2.5, when stretched at a

strain rate $\dot{\varepsilon} = 1.69 \times 10^{-2}$ s^{-1}. The overall stress distribution pattern is similar to that for a hyperelastic sheet in Chapter 2 (Fig. 2.6).

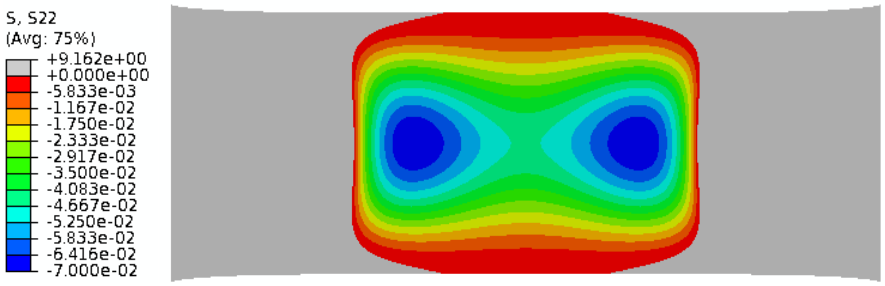

Figure 5.7: Contour of transverse compressive stress (σ_y) at 10% nominal strain for a rectangular sheet with the length-to-width ratio α = 2.5, when stretched at a strain rate of 0.0169 s^{-1}.

The maximum compressive stress in the sheet is plotted in Figure 5.8 as a function of the nominal strain for three different strain rates, which shows the non-monotonic change in the stress magnitude, qualitatively similar to the hyperelastic case (Fig. 2.8a). The time scales in Table 5.1 are used here for the three different strain rates, as discussed in Section 5.2.1. For comparison, the maximum compressive stresses are plotted for two hyperelastic sheets with the initial shear modulus equal to the instantaneous and equilibrium moduli, μ_0 and μ_∞, respectively. For the hyper-viscoelastic sheet, while the overall behavior is qualitatively similar, the stress magnitude increases with increasing strain rates, bounded by the two hyperelastic limits, which is expected as a result of viscoelastic stress relaxation.

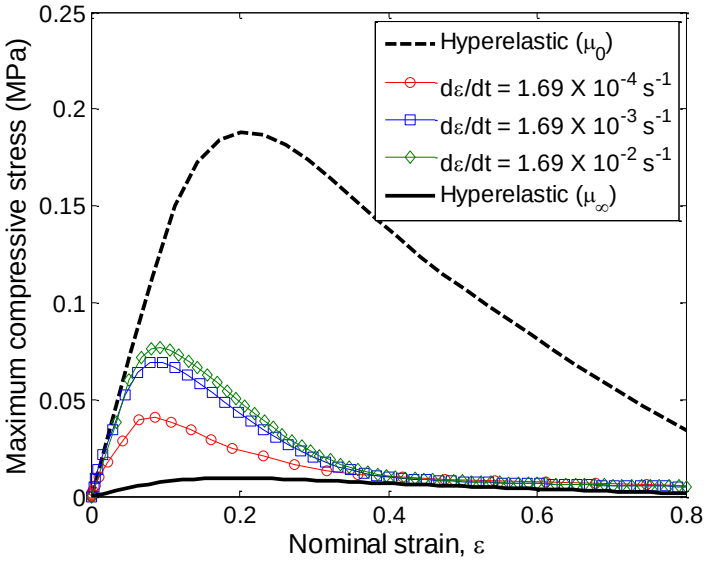

Figure 5.8: Maximum compressive stress in a hyper-viscoelastic thin sheet (α = 2.5 and β = 1000) subject to uniaxial stretch with clamped ends, in comparison with two hyperelastic limits.

5.3.2 Stress analysis with PN nonlinear viscoelastic model

To perform the stress analysis of an end-clamped sheet using the PN nonlinear viscoelastic material model, a 3D FEA model is required in ABAQUS. Referring to Fig. 1.8, the sheet dimensions in the model are: L_0 = 250 mm, W_0 = 100 mm, and t_0 = 0.1 mm. For computational efficiency, a quarter model is used with one layer of C3D8R elements and the material is assumed to be nearly incompressible (with a bulk modulus K = 20,000 MPa and $K/\mu_0 \sim 200$). Each element has in-plane dimension of 1 mm × 1 mm and thickness of 0.1 mm. The mesh used here is first checked by using hyperelastic material properties in comparison with the results from the 2D plane-stress model.

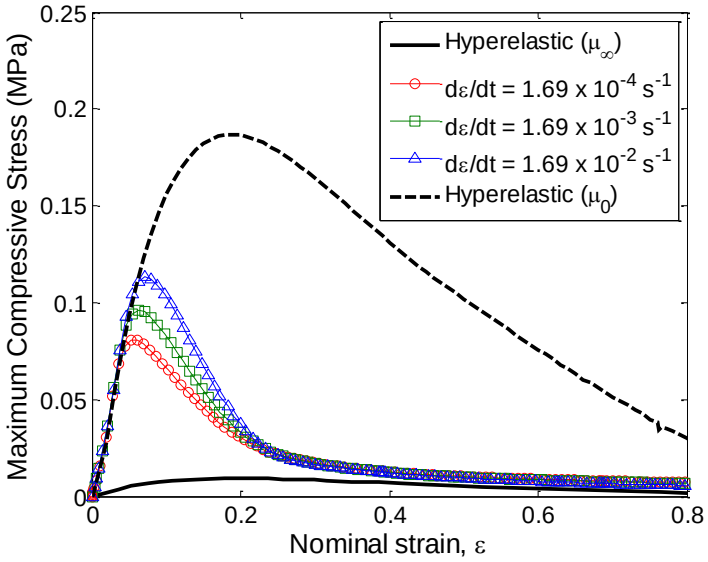

Figure 5.9: Maximum transverse compressive stress in a PN nonlinear viscoelastic thin sheet subject to uniaxial stretch with clamped ends for aspect ratios α = 2.5 and β = 1000, obtained from a three-dimensional stress analysis.

With the PN nonlinear viscoelastic model, the stress distribution is found to be qualitatively similar to that discussed for both hyperelastic and hyper-viscoelastic sheets as shown in Figure 5.7. As shown in Fig. 5.9, the magnitude of the maximum compressive stress changes non-monotonically with the nominal strain. Similar to Fig. 5.8, the stress magnitude increases with increasing strain rate, and it is bounded by the two hyperelastic limits corresponding to the instantaneous and equilibrium shear moduli, μ_0 and μ_∞, respectively. Unlike the HVE model, the rate dependence in the PN model is predicted by using a single set of material parameters as listed in Table 5.3. The stress magnitude by the PN model is slightly higher than by the HVE model. In both viscoelastic models, we note that the maximum compressive stress first follows the hyperelastic limit with the instantaneous shear modulus (μ_0) at relatively small strain and

then approaches the hyperelastic limit with the equilibrium shear modulus (μ_∞) at larger strain. The effect of viscoelasticity is most significant for intermediate strain levels.

5.4 POST-BUCKLING ANALYSIS

To simulate stretch-induced wrinkling in the viscoelastic thin sheets, we perform buckling and post-buckling analyses using the HVE and PN material models in ABAQUS. Similar to the analyses in Chapter 3, an eigenvalue buckling analysis is conducted first to obtain relevant eigenmodes, which are then used as the initial imperfections for the quasi-static post-buckling analysis. The amplitude of the initial imperfection is around 1% of the sheet thickness.

5.4.1. Post-Buckling Analysis with HVE model

Similar to the hyperelastic thin sheets (Chapter 3), post-buckling analyses are performed for hyper-viscoelastic thin sheets using the shell elements (S4R) in ABAQUS. Figure 5.10 shows the simulated wrinkle pattern for a hyper-viscoelastic thin sheet stretched to 10% nominal strain at the strain rate 1.69×10^{-2} s^{-1}. The dimensions of the sheet are same as the polyethylene sheet used in the experiments, with L_0 = 250 mm, W_0 = 100 mm, and t_0 = 0.1 mm. The wrinkle pattern is similar to Figure 1.8b as well as the pattern in a hyperelastic thin sheet shown in Fig. 3.6.

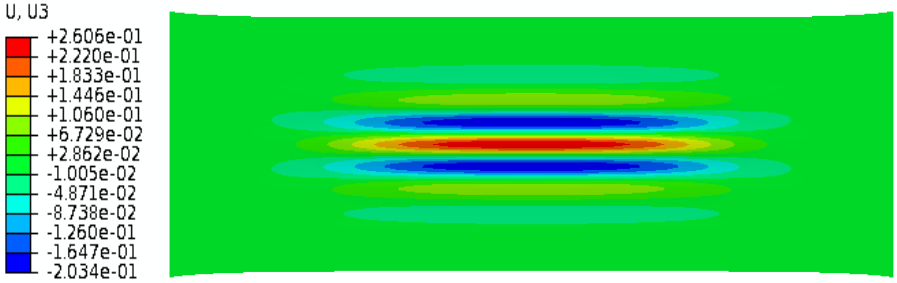

Figure 5.10: Simulated wrinkle pattern for a hyper-viscoelastic thin sheet (α = 2.5 and β = 1000) stretched to 10% nominal strain at the strain rate 1.69 x 10^{-2} s^{-1}.

Figure 5.11 plots the wrinkle amplitude as a function of the nominal strain for the hyper-viscoelastic sheet stretched at different strain rates, in comparison with the results for a hyperelastic sheet. The material parameters for the HVE model are listed in Table 5.1, with different time scales for different strain rates. Recall that the wrinkle amplitude for a hyperelastic sheet is independent of its shear modulus, as discussed in Chapter 3. For the HVE model, the wrinkle amplitude depends on the viscoelastic time scale and increases with increasing strain rate (shorter time scale), consistent with increasing compressive stress shown in Fig. 5.8. Theoretically it may be expected that the wrinkling behavior in a hyper-viscoelastic sheet approaches the same hyperelastic limit at both low and high strain rates. However, for the three strain rates considered in the present study, we only see that the wrinkle amplitude approaches the hyperelastic case when strain rate increases. More interestingly, while the wrinkle amplitude was predicted to vanish in the hyperelastic sheet beyond about 30% strain (Chapter 3), the wrinkle amplitude in the hyper-viscoelastic sheet remains non-zero up to a much larger strain (up to 80%). This

behavior agrees qualitatively with the experimental results for the polyethylene sheet (Figure 4.8), but the reason for such a behavior of wrinkle amplitude is not clear.

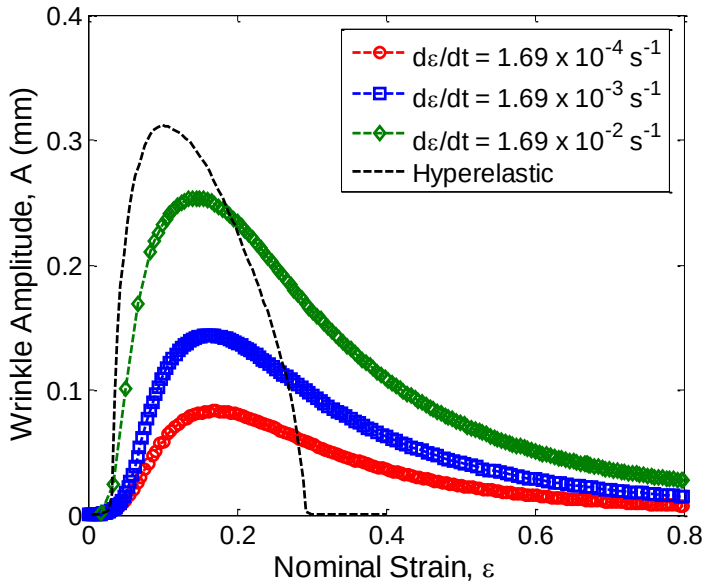

Figure 5.11: Amplitude of stretch-induced wrinkles in a hyper-viscoelastic thin sheet (α = 2.5 and β = 1000), obtained by the post-buckling analysis. The result for the hyperelastic limit is shown for comparison.

By dimensional analysis (see Appendix A), the wrinkle amplitude in a hyper-viscoelastic thin sheet may be written as

$$\frac{A}{h_0} = f\left(\varepsilon, \alpha, \beta, \dot{\varepsilon}\tau, \frac{\mu_\infty}{\mu_0}\right) \tag{5.19}$$

In comparison with Eq. (3.17) for the hyperelastic sheets, the normalized wrinkle amplitude depends on the viscoelastic parameters of the HVE model in addition to the nominal strain and aspect ratios. In particular, the strain-rate dependence results naturally from the viscoelastic time scale. As listed in Table 5.1, when the strain rate increases, the dimensionless group, $\dot{\varepsilon}\tau$, increases, and the corresponding wrinkle amplitude in Fig. 5.11

increases. Moreover, the wrinkle amplitude depends on the ratio between the two elastic moduli, μ_∞/μ_0, as shown in Figure 5.12. Here, the wrinkle amplitude is simulated for the hyper-viscoelastic sheet with the strain rate of 0.0169 s^{-1} and the corresponding time scale, τ = 3 sec. As the modulus ratio μ_∞/μ_0 increases, the wrinkle amplitude increases or decreases, depending on the level of nominal strain with a trend approaching the hyperelastic behavior. It is expected that the HVE model recovers the hyperelastic model when $\mu_\infty/\mu_0 = 1$. The viscoelastic branch in the HVE model lowers the wrinkle amplitude in the early stage but delays the suppression of wrinkling in the late stage. As the modulus ratio μ_∞/μ_0 decreases, more stress is carried by the viscoelastic branch, and hence the viscoelastic effect becomes more significant.

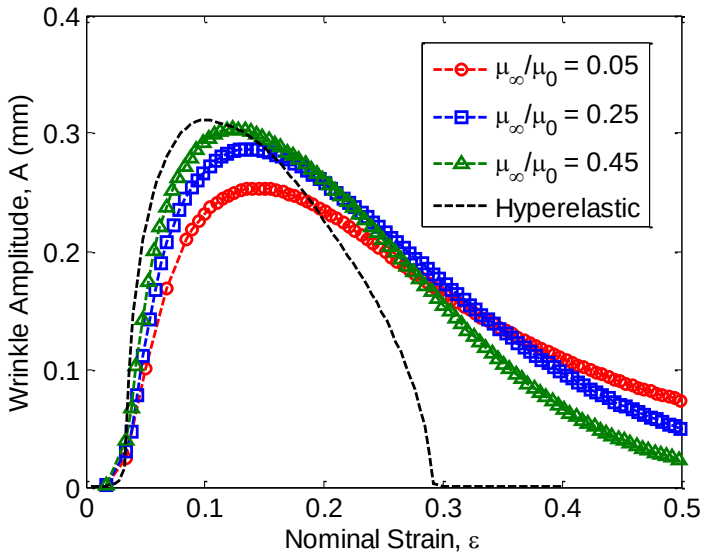

Figure 5.12: Effect of modulus ratio (μ_∞/μ_0) on the wrinkle amplitude simulated by using HVE model (μ_0 = 90 MPa and τ = 3 sec).

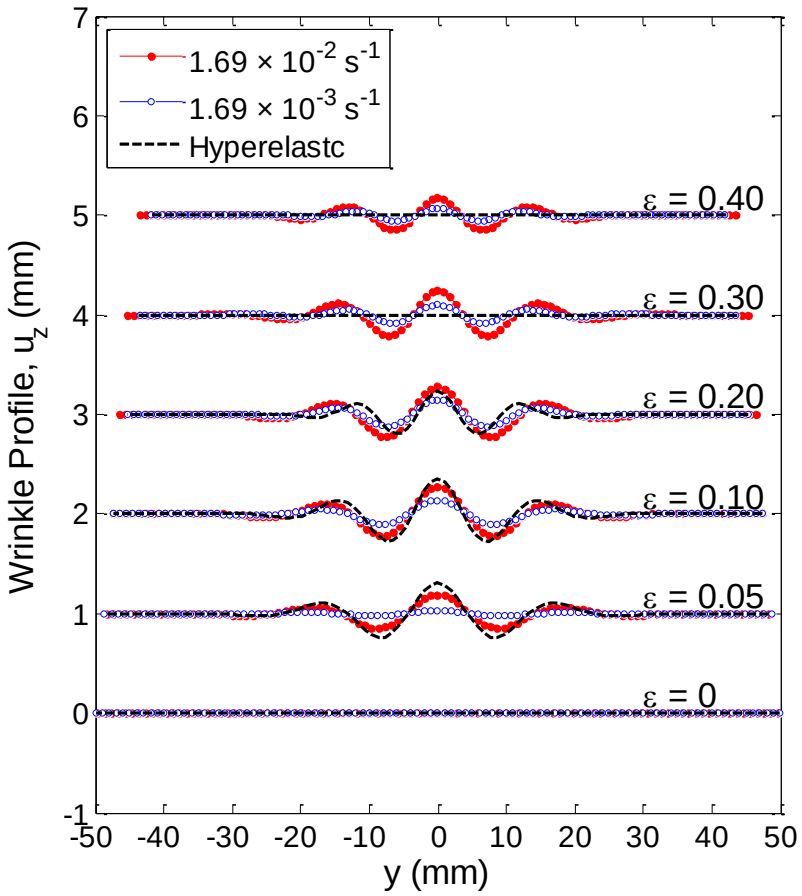

Figure 5.13: Comparision of wrinkle profiles between a hyper-viscoelastic sheet and a hyperelastic sheet.

It is found that, while the wrinkle amplitude (A) depends on the strain-rate for a hyper-viscoelastic thin sheet, the wrinkle profile is less sensitive to the strain rate, with the number of wrinkles depending mostly on the two aspect ratios (α and β). Figure 5.13 compares the wrinkle profiles for a HVE sheet when stretched at two different strain rates with a hyperelastic thin sheet. The wrinkle profiles in all cases are found to be similar, whereas the wrinkle amplitude changes with the strain and strain rate. This indicates that

the wrinkle profile depends primarily on the sheet geometry rather than the material behavior whereas the wrinkle amplitude depends on both geometry and material.

5.4.2. Post-Buckling Analysis with PN nonlinear viscoelastic model

To perform the post-buckling analysis for PN nonlinear viscoelastic sheets, a three-dimensional finite element model with C3D20R elements in ABAQUS is used and the material is assumed to be nearly incompressible (bulk modulus K = 20,000 MPa and ratio $K/\mu_B \sim 200$). The post-buckling analyses are performed for a thin sheet with the same dimensions as the polyethylene sheet used in the experiments, L_0 = 250 mm, W_0 = 100 mm, and t_0 = 0.1 mm. The mesh size is similar to that used for the stress analysis in Section 5.3.2, but with two layers of elements instead of one layer. The model is again verified for the hyperelastic thin sheets by comparing the wrinkling results with the corresponding shell model.

The post-buckling analyses show qualitatively similar results as for the HVE model. As shown in Figure 5.14, the wrinkle amplitude depends on the strain rate, but the rate dependence is not as strong as for the HVE model (Fig. 5.12). Here the rate dependence is predicted by the PN model using the single set of material parameters (Table 5.3). Similar to the HVE model, the PN model predicts non-zero wrinkle amplitude well beyond 30% nominal strain, in contrast to the hyperelastic sheet.

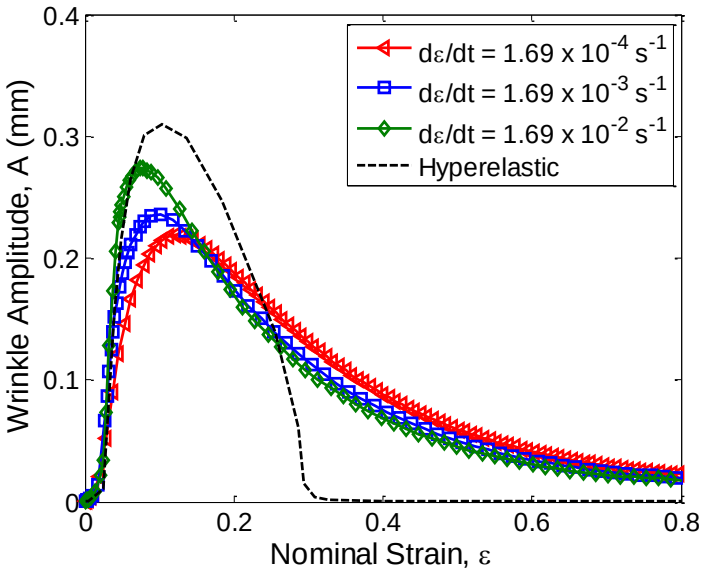

Figure 5.14: Amplitude of stretch-induced wrinkles in a PN nonlinear viscoelastic thin sheet with aspect ratios, α = 2.5 and β = 1000, obtained by the post-buckling analysis. The result for the hyperelastic limit is shown for comparison.

By dimensional analysis (see Appendix A), the normalized wrinkle amplitude in the PN nonlinear viscoelastic thin sheet can be written as a function of 7 dimensionless quantities:

$$\frac{A}{h_0} = f\left(\varepsilon, \alpha, \beta, \bar{\tau}\dot{\varepsilon}, \frac{\mu_A}{\mu_B}, n, m\right) \tag{5.20}$$

where $\bar{\tau} = \left(B\mu_B^n\right)^{-1/(m+1)}$ is a time scale. Using the values of material parameters listed in Table 5.3, the time scale $\bar{\tau} = 2.4 \times 10^{-6}$s. However, as suggested by Eq. (5.15), the relaxation time scale in the nonlinear viscoelastic model depends on the stress σ_B, which could vary both in time and in space. Nevertheless, with the time scale $\bar{\tau}$, the strain rate dependence of the wrinkling behavior is expected. In addition, the normalized wrinkle

amplitude depends on the two dimensionless parameters in the PN model, *n* and *m*. Similar to the HVE model, the wrinkle amplitude also depends on the modulus ratio, μ_A / μ_B or μ_∞ / μ_0, in the PN model, as shown in Figure 5.15. The dependence however is more complicated. As the modulus ratio μ_∞ / μ_0 is increased from 0.05 to 0.25, the wrinkle amplitude increases considerably, even greater than the hyperelastic model. As the modulus ratio μ_∞ / μ_0 is increased further to 0.45, the wrinkle amplitude decreases slightly, approaching the hyperelastic case.

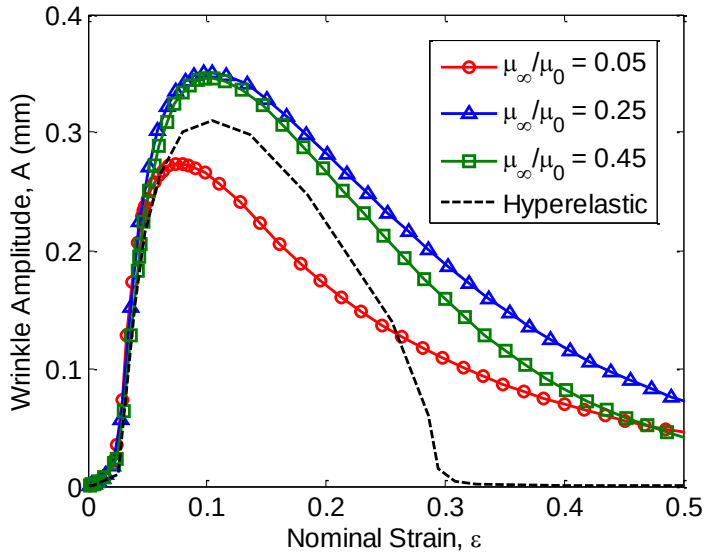

Figure 5.15: Effect of modulus ratio (μ_∞/μ_0) on the wrinkle amplitude simulated using PN nonlinear viscoelastic model.

5.5 COMPARISON AND DISCUSSION

5.5.1 Wrinkle Profile and Amplitude

In this section, we present a direct comparison between the experimental measurements and numerical simulations. As shown in Figures 5.16, the wrinkle profiles measured by the 3D-DIC method at different strain levels with a strain rate of 0.0169 s^{-1} are compared to the simulated profiles using the HVE model for the polyethylene sheet specimen with aspect ratio α = 2.5. Except for the initial undulation in the experiment, the number of wrinkles and the wrinkle amplitude obtained by the numerical simulation are in good agreement with the measurements up to ε = 20%, similar to the comparison with the hyperelastic model (Fig. 4.7). At ε = 30% and 40%, however, the HVE model overestimates the wrinkle amplitude.

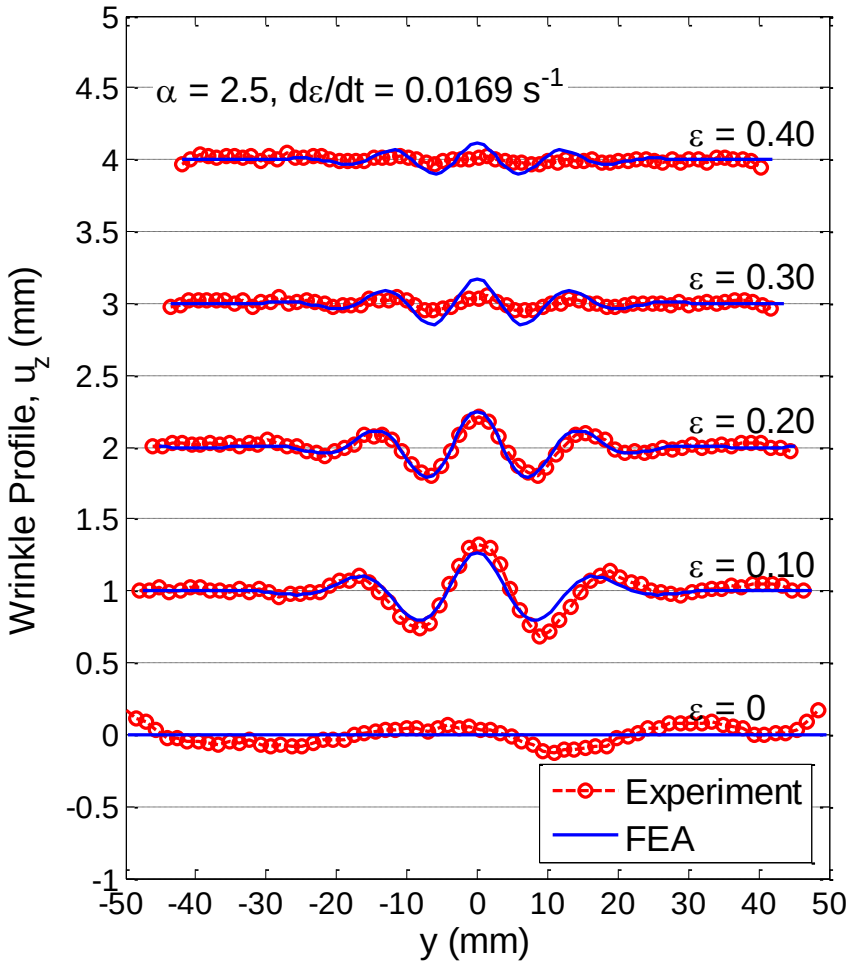

Figure 5.16: Comparison of wrinkle profiles between experiments and FEA simulations using the hyper-viscoelastic model, with strain rate $d\varepsilon/dt$ = 0.0169 s^{-1} and aspect ratio α = 2.5.

Figures 5.17 plots the wrinkle amplitude as a function of the nominal strain for polyethylene sheets with two different aspect ratios, α = 2.5 and 2, each with two different strain rates. The hyper-viscoelastic model compares slightly better with the experimental measurements. In particular, the wrinkle amplitude remains observable

beyond 30% nominal strain in both the experiments and the hyper-viscoelastic model. The overall agreement between the experiments and numerical simulations is slightly improved by using the hyper-viscoelastic material model, but the maximum wrinkle amplitudes are under-predicted by the simulations for both the aspect ratios, α = 2 and 2.5. For aspect ratio α = 2.5, the wrinkle amplitude shows better agreement at strain rate of 0.0169 s^{-1}, whereas for the strain rate of 0.00169 s^{-1}, the predicted wrinkle amplitude is considerably lower than the observed value. The discrepancies again suggest that the HVE model is not sufficient to capture the wrinkling behavior.

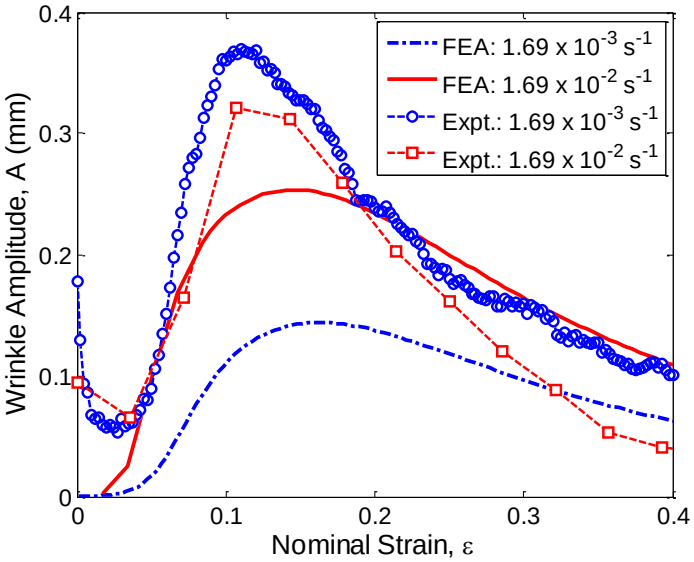

(a)

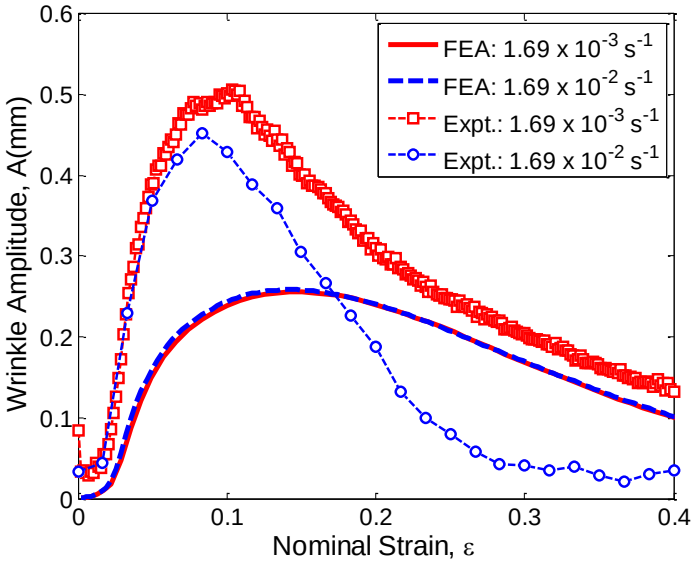

(b)

Figure 5.17: Comparison of wrinkle amplitudes between experiments and FEA simulations using the HVE model for two aspect ratios: (a) α = 2.5; (b) α = 2.

Next, we compare the numerical simulations using the PN nonlinear viscoelastic model with the experimental measurements. Figures 5.18 shows the wrinkle amplitude versus nominal strain for specimens with two aspect ratios: α = 2.5 and 2. In comparison with the previous models (hyperelastic and HVE), the PN model shows considerably improved the overall agreement with the experiments. The higher wrinkle amplitudes measured for the specimen with α = 2.5 (Figure 5.18a) might be due to the initial undulations (Fig. 5.19a) that occur as a result of misalignment of the clamps attached to the sheet. Under clamped-ends stretching, if only initial imperfection is increased in the simulations, the maximum wrinkle amplitude remains unaffected but the critical strain for the wrinkle initiation is not predicted well. Instead of showing the bifurcation point, the wrinkle-strain response shows a smooth transition to the wrinkled state as the sheet is stretched. For the specimen with α = 2, it can be noticed that the initial shape of sheet is relatively flat as shown in Figure 5.19b, and thus the amplitudes are in better agreement. A comparison of the wrinkle profiles is shown in Figure 5.19. Apparently, the PN model is better suited for simulating the wrinkling behavior of the polyethylene sheets.

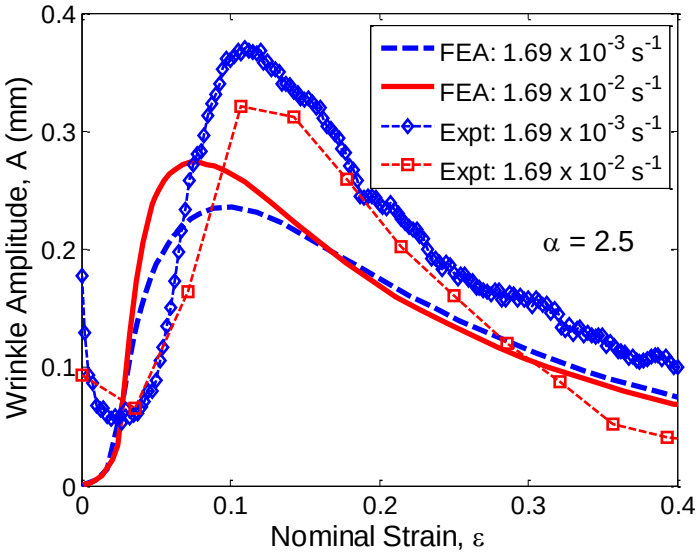

(a)

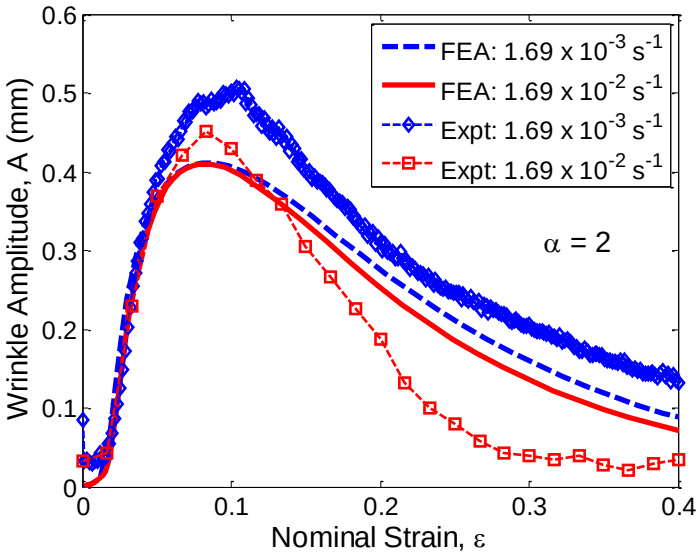

(b)

Figure 5.18: Comparison of wrinkle amplitudes between experiments and FEA simulations using the PN nonlinear viscoelastic model for two aspect ratios: (a) α = 2.5; (b) α = 2.

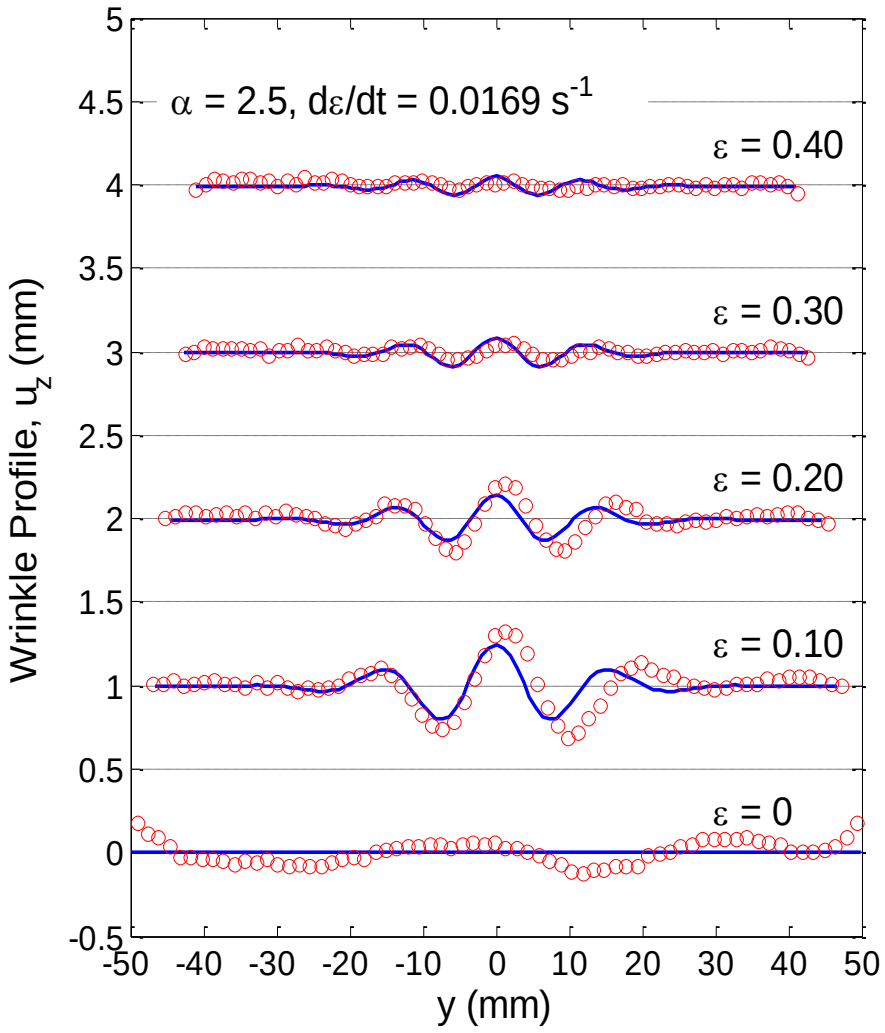

(a)

Figure 5.19: Comparison of wrinkle profile at different strain levels between experiments (markers) and FE simulations (lines) using PN nonlinear viscoelastic model for aspect ratio, α = 2.5 and strain rate of $d\varepsilon/dt$ = 0.0169 s^{-1}.

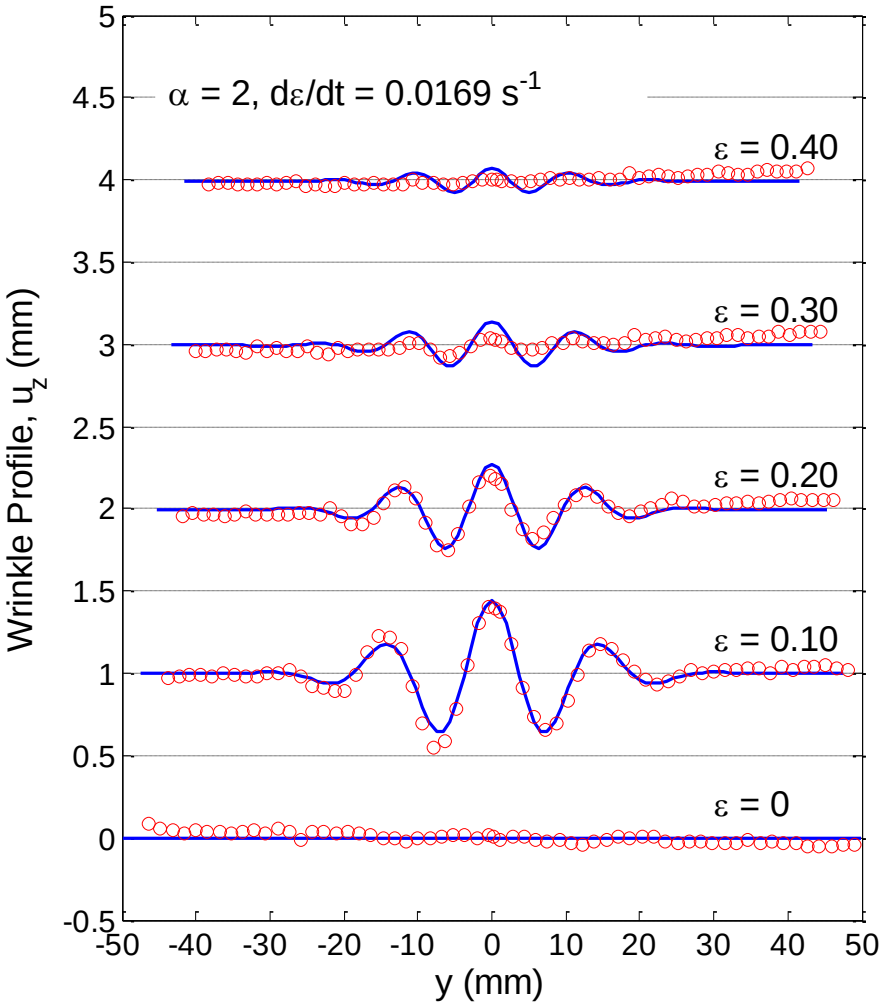

(b)

Figure 5.19: cont.

5.5.2 Wrinkle Wavelength

As discussed in Chapter 4, the measured wrinkle wavelengths are in good agreement with the scaling analysis by Cerda and Mahadevan (2003). As shown in Fig. 5.20, similar wrinkle wavelengths are predicted by the HVE and PN material models, suggesting that the wrinkle wavelength is insensitive to the constitutive behavior of the material. In other words, the wrinkle wavelength depends primarily on the geometry of the sheet, while the wrinkle amplitude is more sensitive to the mechanical properties of the material.

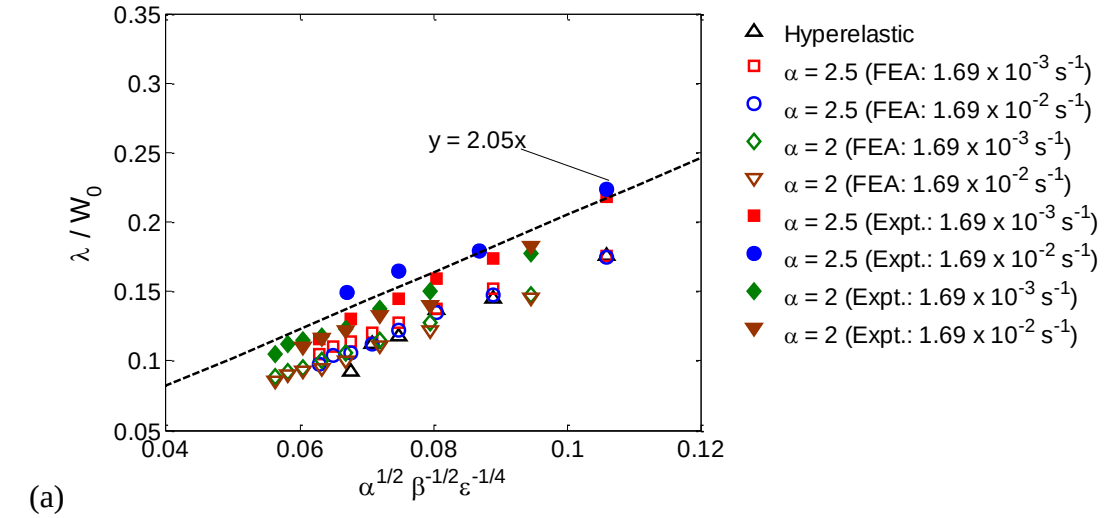

(a)

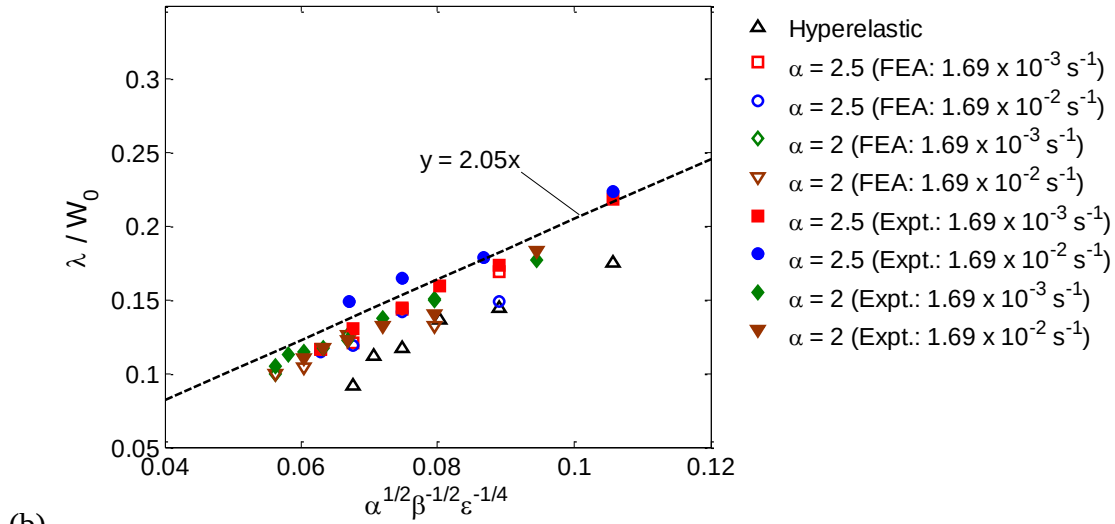

(b)

Figure 5.20: Normalized wrinkle wavelength in comparison with the scaling analysis (dashed line). The open symbols show the numerical results from FEA simulations, and the filled symbols show experimental results. Results are shown for two different aspect ratios, α = 2 & α = 2.5, stretched at two different strain rates for two viscoelastic models: (a) HVE model; (b) PN nonlinear viscoelastic model.

5.5.3 Wrinkle Relaxation

Section 4.3 describes the wrinkle relaxation behavior observed in the experiments. Using the HVE model and the PN nonlinear viscoelastic model, we simulate the relaxation experiments and compare with the measurements. The experiments were done on a polyethylene sheet with aspect ratio α = 2.5, which was stretched at a strain rate of 0.000169 s^{-1}. At this strain rate, the wrinkle amplitude predicted by the HVE model (Figure 5.12) is significantly smaller than the experimental measurements (Figures 4.13 - 4.16). When relaxation is allowed at a specific nominal strain, the wrinkle amplitude increases and approaches the elastic limit. Unlike the experiments, it takes a relatively long time to reach the equilibrium state, as shown in Figure 5.21. Such a wrinkling behavior may be expected for a simple viscoelastic sheet, but not for the polyethylene sheets used in the experiments.

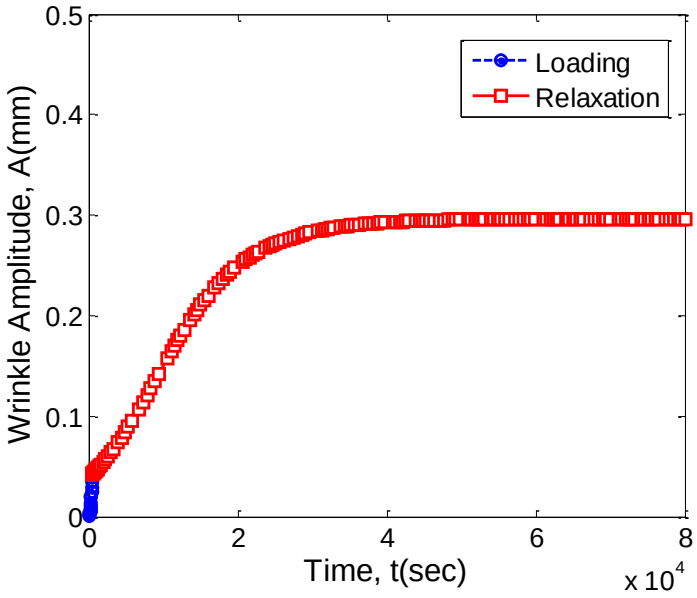

Figure 5.21: Simulated wrinkle amplitude using the HVE model when the sheet is first stretched with a strain rate of 0.000169 s^{-1} and then allowed to relax at 8% nominal strain.

Figure 5.22 shows the FEA results for the relaxation experiments for the PN nonlinear viscoelastic model when the nominal strain is held at 8%, 10%, 15% and 20%. Similar to the experiments, the PN model predicts that the wrinkle amplitude does not change significantly with time during the relaxation tests. However, experiments do indicate that a slight change in the wrinkle amplitude is governed by the corresponding hyperelastic wrinkle amplitude, but with the PN nonlinear viscoelastic model, no change is observed at all.

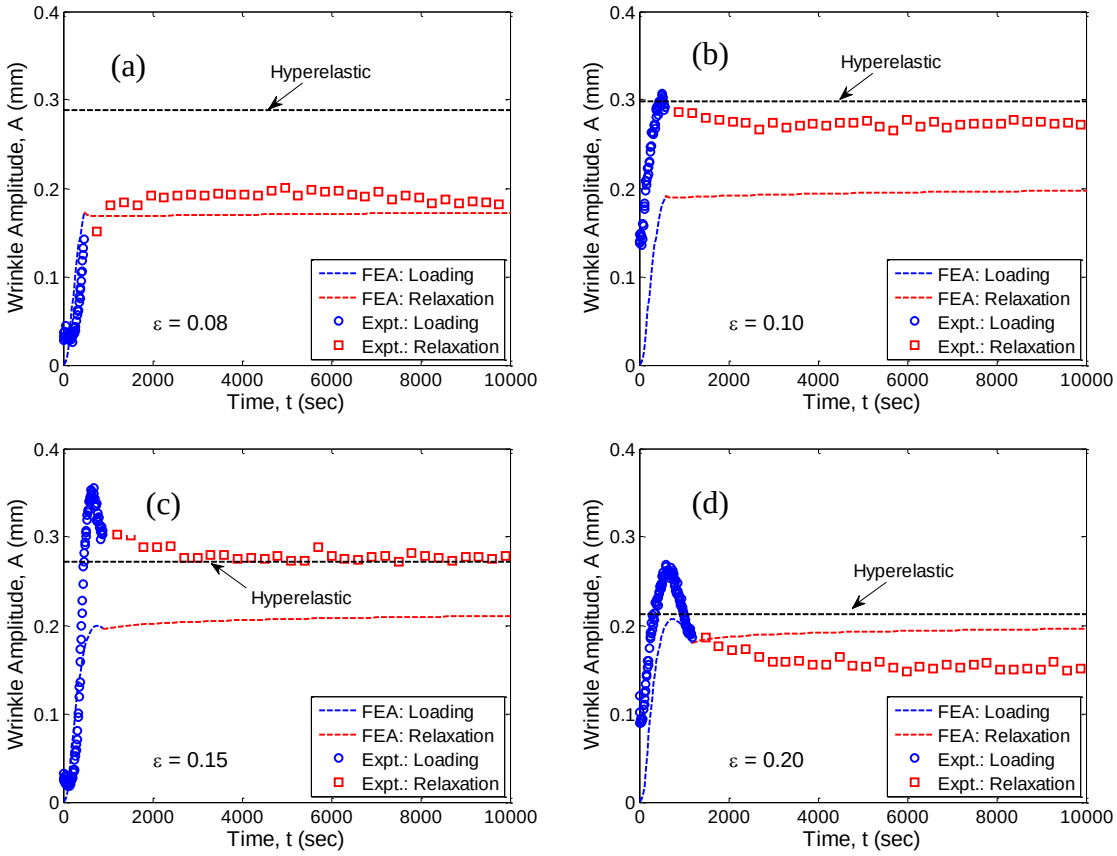

Figure 5.22: Comparison between experiments and FE simulations using PN nonlinear viscoelastic model of wrinkle amplitude response with time as sheet is stretched and allowed to relax at different nominal strains: (a) $\varepsilon = 0.08$; (b) $\varepsilon = 0.10$; (c) $\varepsilon = 0.15$; (d) $\varepsilon = 0.20$. For reference, the wrinkle amplitude in a hyperelastic sheet is also shown at the corresponding strain level.

5.5.4 Other factors

It is noted that, although the PN nonlinear viscoelastic model captures the constitutive behavior of polyethylene reasonably well, discrepancies between the stretch-induced wrinkling experiments and the FEA simulations remain for several reasons. First, the discrepancies at small strain levels may arise primarily due to the initial undulation of the specimen, especially for the wrinkle amplitude. In addition, it is important to align the

specimen precisely with the loading devices to avoid wrinkles induced by shearing or twisting. The clamping boundary condition at both ends of the specimen is also challenging as the thin sheet could partly slide out of the clamps at large strains. Other experimental uncertainties may result from the non-uniformity of the polyethylene sheets. It is found that the thickness of the polyethylene sheet specimen could vary spatially up to 10 μm with the nominal thickness of 100 μm. Figure 5.23 shows the effect of sheet thickness on the wrinkle amplitude, simulated using HVE model, in comparison to the experiment; clearly a $\pm$ 10 μm fluctuation in the sheet thickness could contribute to a factor of 3 difference in the peak wrinkling amplitude. Qualitatively similar effect is expected for the PN nonlinear viscoelastic model. With this in mind, the comparisons shown in Figures 5.16 and 5.17 should be considered to be acceptable.

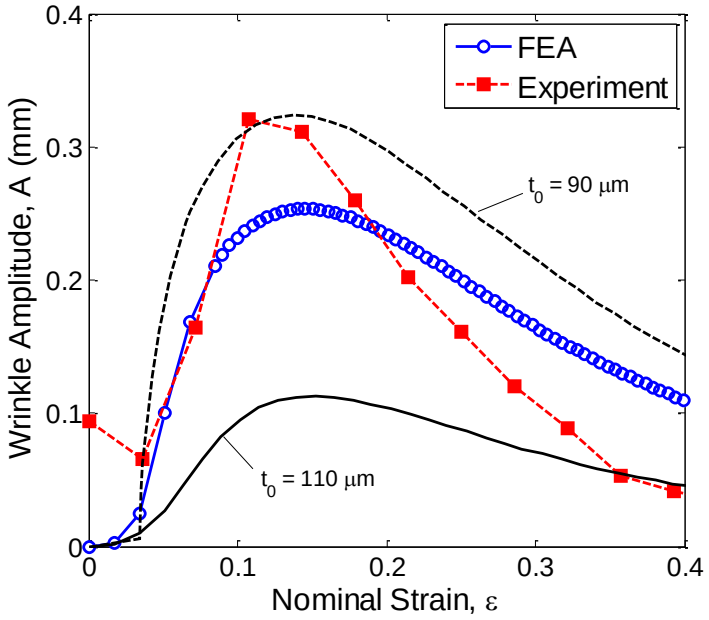

Figure 5.23: Effect of sheet thickness on wrinkle amplitude for a HVE sheet with aspect ratio, α = 2.5 when stretched at a strain rate of 0.0169 s^{-1}. The experimental data for a polyethylene sheet is shown for comparison.

5.6 SUMMARY

In this chapter, two viscoelastic material models were considered for finite element simulations of stretch-induced wrinkling in polyethylene thin sheets. The FEA results were compared with the experimental measurements presented in Chapter 4. In comparison to the hyper-viscoelastic (HVE) model, the parallel network nonlinear viscoelastic model is better suited for simulating the constitutive behavior of polyethylene, both for the uniaxial stress-strain response and the stress relaxation tests. Using both models, the stress analysis and wrinkling analysis were performed to elucidate the effects of viscoelasticity. In comparison with the experimental measurements for the polyethylene sheets, the PN model showed better agreement for the wrinkle amplitude. On the other hand, the wrinkle wavelength is insensitive to the material model.

CHAPTER 6

Wrinkling in Thin Inhomogeneous Sheets

6.1 INTRODUCTION

In this chapter, effect of inhomogeneous material on wrinkling instability is studied. During the course of experimental study on stretch-induced wrinkling, it was observed that inhomogeneous material properties affect the wrinkle behavior. Figure 5.16 showed wrinkles at a relatively small scale, where it was noticed that primary reason for wrinkling was the material defects. If the inclusion size is small enough, wrinkles are not affected at small strains however local wrinkling initiates at relatively large strains. Also, if the global wrinkle wavelength is relatively large as compared to the inclusion size, the wrinkle profile is not affected by inclusion. Figures 6.1a and 6.1b show formation of wrinkles in polyethylene and rubber sheets respectively. Under clamped-ends stretching condition, a different wrinkling pattern is observed from that predicted in chapter 3 and experimentally observed in Chapter 4. As shown in the figures, wrinkles mostly formed in a local region of the sheet and number of wrinkles is also higher as compared to the homogeneous sheet wrinkling (Figure 1.8b). It is suspected that some local region of the sheet has different material stiffness that resulted in such wrinkling pattern. Some studies have been conducted to study the effects of inhomogeneous material properties on wrinkling. Takei et al. (2011) showed the effect of reinforcement on a thin sheet stretched under clamped-ends as shown in Figure 6.1c. The sheet is made stiffer locally by attaching an adhesive tape on its surface. On stretching, the sheet shows a different

wrinkle pattern as compared to the homogeneous case (Figure 1.8b). Figure 6.1d shows wrinkling in a rubber balloon. In this case a defect is produced by adding glue on the surface of an inflated balloon [Cerda, 2005].

To study the effect of inhomogeneous material properties, we consider a model problem as schematically shown in Figure 6.2 similar to that considered in studying stretch-induced wrinkling (Chapter 1). The two opposite ends of the sheet are clamped and other two are traction free and then subjected to uniaxial stretch. The inhomogeneity is applied by changing the shear modulus (μ_2) in a local narrow region, referred as 'material 2' (Figure 6.2) and the rest of the sheet material referred as 'material 1'. Both 'material 1' and 'material 2' are assumed incompressible and hyperelastic (Neo-Hookean). A new parameter 'ρ' is introduced, which defines stiffness ratio of material 2 and material 1 ($\rho = \mu_2/\mu_1$). In the present study, shear modulus of material 1 is assumed to be 1 MPa and shear modulus of material 2 is varied. The overall in-plane (L_0/W_0) and out-of-plane (W_0/t_0) sheet aspect ratios are taken as 2.5 and 1000 respectively. Material 2 is defined at the center of the sheet as shown in Figure 6.2 such that ratio, $b/L_0 = 0.05$ and equal thickness is assumed for both the materials. In the following section, two-dimensional stress/strain distribution in an inhomogeneous thin sheet relative to a homogeneous sheet is discussed. Further the buckling eigen value problem for a thin inhomogeneous sheet is considered and wrinkling response is analyzed through the post-buckling analysis. The stress and wrinkling analyses are done using plane stress and shell mode respectively in ABAQUS.

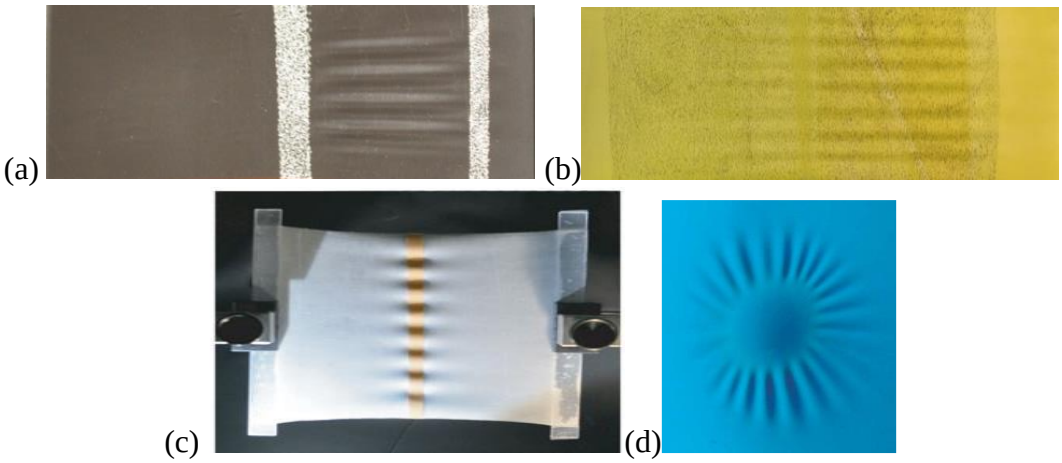

Figure 6.1: (a) A wrinkling pattern observed in an inhomogeneous polyethylene sheet under clamped-ends stretching; (b) A wrinkling pattern observed in an inhomogeneous rubber sheet under clamped-ends stretching; (c) A wrinkling pattern observed in a reinforced sheet under clamped-ends stretching [Takei et al., 2011]; (d) The wrinkling pattern obtained by the defect produced on the surface of an inflated balloon by adding a drop of glue [Cerda, 2005].

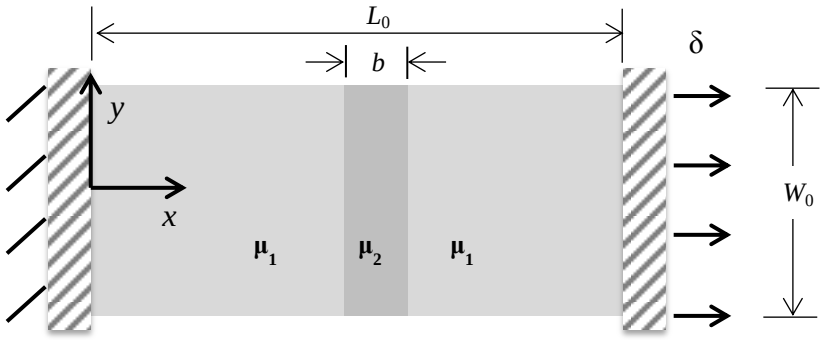

Figure 6.2: Schematic illustration of an inhomogeneous rectangular sheet with clamped-ends subjected to uniaxial stretch.

6.2 2-D ANALYSIS

A 2-D analysis is performed to study the stress/strain distribution in an inhomogeneous thin sheet relative to homogeneous sheet case under clamped-ends

stretching. Figure 6.3 schematically illustrates the effect of uniaxial stretch on an inhomogeneous sheet described in Figure 6.2. Qualitatively the deformation in an inhomogeneous sheet is similar to either Figure 6.3a or 6-3b depending on the stiffness ratio, where dotted line represents the initial geometry of the inhomogeneous sheet. Note that normal tractions are not marked in the figure while showing the direction of shear traction applied at the interfaces of two materials. When $\rho > 1$, i.e. material 2 is stiffer than material 1, the tractions on the model problem at the two interfaces can be replaced with the appropriate shear (normal tractions not shown in the Figure) as shown in Figure 6.3a. When displacement, δ is applied at the end, material 2 has higher stiffness and, it undergoes lower longitudinal strain and hence lesser transverse contraction. With $\rho < 1$, the deformation and the interface tractions can be approximately represented as shown in Figure 6.3b. In both cases, there is a mismatch at the interface of two materials, which results in shear traction. When, $\rho > 1$, the shear traction acting along the transverse direction on the two sides of the material 2, applies additional transverse compressive effect. For $\rho < 1$, this effect is opposite and the shear traction as shown in Figure 6.3b decreases the transverse compressive effect in material 2.

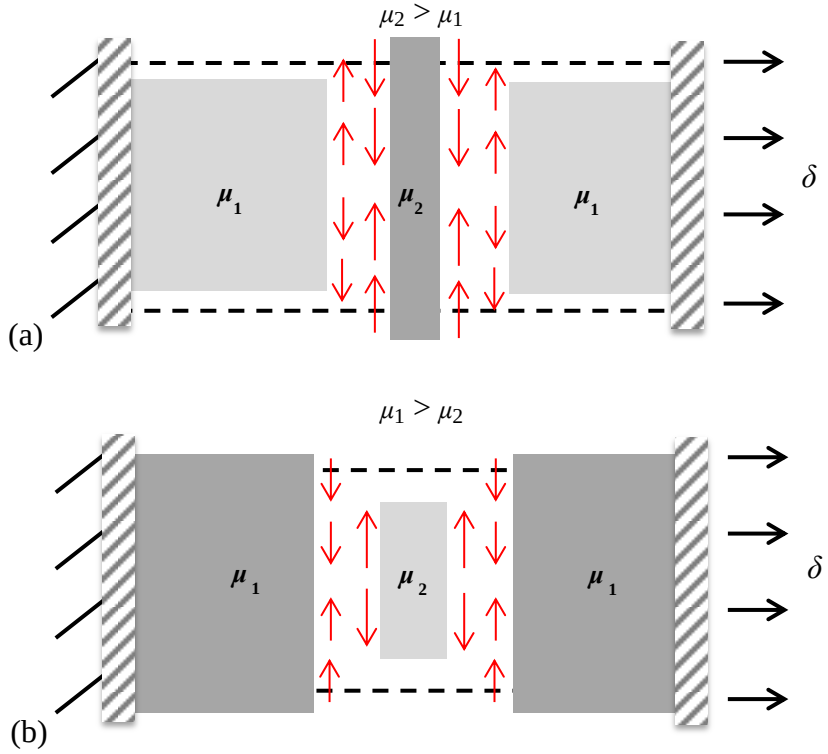

Figure 6.3: Schematic illustration of an inhomogeneous thin sheet deformation when subjected to clamped-ends stretching: (a) with stiffness ratio, $\rho > 1$; (b) with stiffness ratio, $\rho < 1$.

Figure 6.4 shows the comparison of stress distribution in inhomogeneous sheets with homogeneous thin sheet at 10% nominal strain. For the inhomogeneous case, the stiffness ratio (ρ) is taken as 0.5 and 2. As illustrated in Figure 6.3a for $\rho > 1$, both longitudinal (ε_x) and transverse (ε_y) strain reduces at the center region (material 2) as compared to the homogeneous case or vice-versa when $\rho < 1$. Assuming both material 1 and material 2 as incompressible, the transverse strain (ε_y) is proportional to the longitudinal strain. Therefore, transverse strain in material 2 increases or decreases relative to the homogeneous case, as stiffness ratio (ρ) is decreased ($\rho < 1$) or increased (ρ

> 1) respectively. Thus, qualitatively the deformation in thin inhomogeneous sheets can be approximately shown as in Figure 6.3. Further, the transverse compressive stress in the thin homogeneous sheets is compared to the homogeneous sheet case through a FEA. Figures 6.4a and 6.4b shows the transverse compressive stress distribution in inhomogeneous sheets in the transverse and longitudinal direction respectively. With stiffness ratio, $\rho = 1$, it simplifies to a homogeneous thin sheet case as studied in the previous chapters, the stress distribution for which is shown for the comparison. When stiffness ratio is smaller than 1 ($\rho < 1$), action of shear traction on material 2 weakens the effect of transverse compression relative to the homogeneous case and transverse compressive stress decreases in this case. As shown in Figure 6.4a, the transverse stress is positive locally around the central region of the sheet. Also, the distribution of transverse compressive stress is found similar to the homogeneous case in material 1 as shown in Figure 6.4b. On the other hand, with increase in stiffness ratio ($\rho > 1$), the shear traction acting on material 2, adds to the transverse compression due to the clamped ends and net compression is higher in case of ρ higher than 1. Therefore, as stiffness ratio is increased or decreased from 1, the mismatch or equivalently the shear traction between material 1 and material 2 increases at the interface. But this shear traction at the interface may increase or decrease the transverse compression depending on the stiffness ratio.

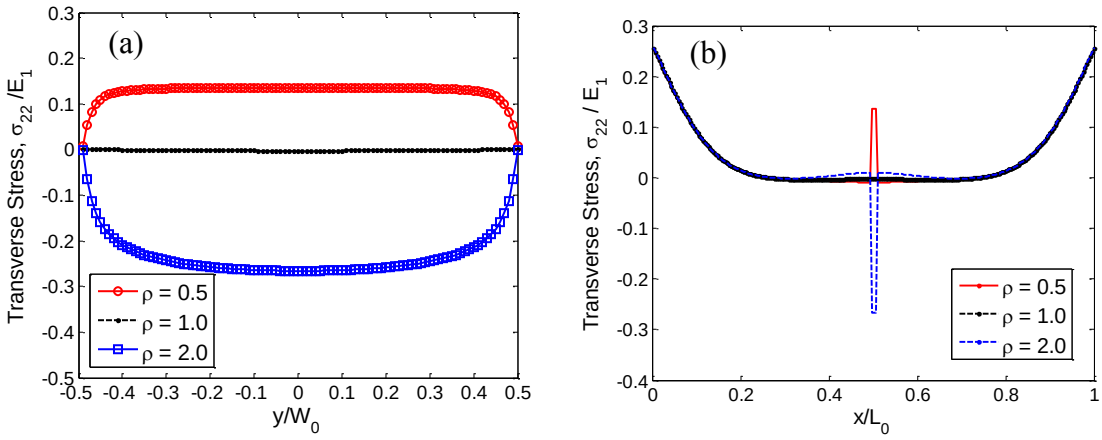

Figure 6.4: Stress and strain distributions for an inhomogeneous thin sheet with stiffness ratio, ρ = 0.5 & 2, compared with the homogenous case (ρ = 1) under clamped-ends stretching: (a) normalized transverse stress (σ_y) along x-direction at y = 0; (b) normalized transverse stress (σ_y) along y-direction at x = L_0/2.

6.3 EIGEN VALUE ANALYSIS

To carry out the wrinkling analysis of thin inhomogeneous sheets, first a buckling eigen value analysis is performed. For given geometrical parameters, it is found that critical strain for onset of wrinkling is higher for the homogeneous sheets (ρ = 1) than the inhomogeneous sheets ($\rho \neq 1$), as shown in Figure 6.5. It shows the critical strain computed for the onset of buckling in inhomogeneous sheets as a function of stiffness ratio (ρ). It is observed that the critical strain decreases significantly as the stiffness ratio changes from 1, thus suggesting that the inhomogeneous sheets become more prone to buckling.

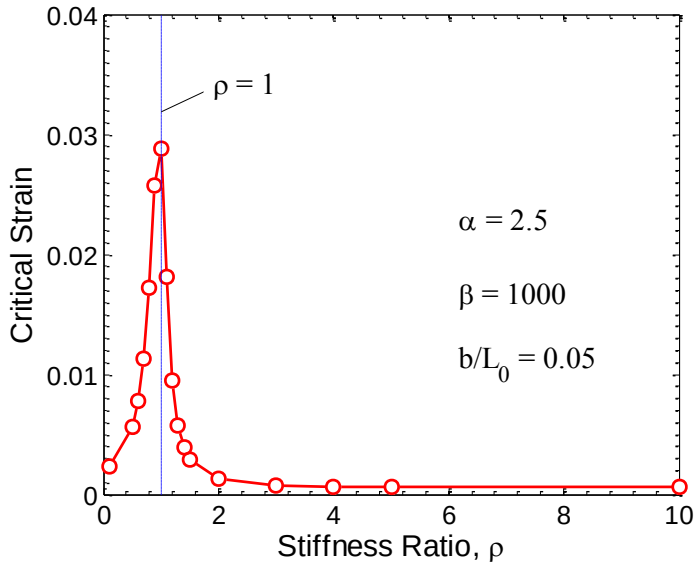

Figure 6.5: Critical strain predicted by buckling eigen value analysis for an inhomogeneous thin sheet as a function of stiffness ratio, under clamped-ends stretching.

Also, the shapes of buckling modes observed in inhomogeneous sheet buckling are different from the homogenous sheet case. Figures 6.6a, 6.6b and 6.6c shows the 1st buckling mode under clamped-ends stretching for cases with stiffness ratio, ρ = 1, 0.5 and 2 respectively. Each of the figures show shape of the 1st buckling mode from three different views: front view (*x*-*y* plane), side view (*y*-*z* plane) and top view (*x*-*z* plane). It is found that the shape of the buckling mode is closely related with the deformation trends and stress distribution for different stiffness ratio as studied in the previous section. As already discussed, with $\rho < 1$, transverse compression decreases relative to the homogenous case, it results in a lower local out-of-plane deformation as shown in Figure 6.6b relative to the homogeneous case (Figure 6.6a). The central narrow region (material

2) is relatively under lower compression, which results in a dip in the out-of-plane deformation along the longitudinal direction as seen from the *x*-*z* plane view of Figure 6.6b. On the other hand, with $\rho > 1$, the buckling mode shows locally higher deformation at the center of the sheet as shown in Figure 6.6c relative to the homogeneous case (Figure 6.6a). In this case, there is an increase in the transverse compression as discussed in the previous section which results in this type of deformation with a higher local out-of-plane deformation along the longitudinal direction as seen from the *x*-*z* plane view of Figure 6.6c.

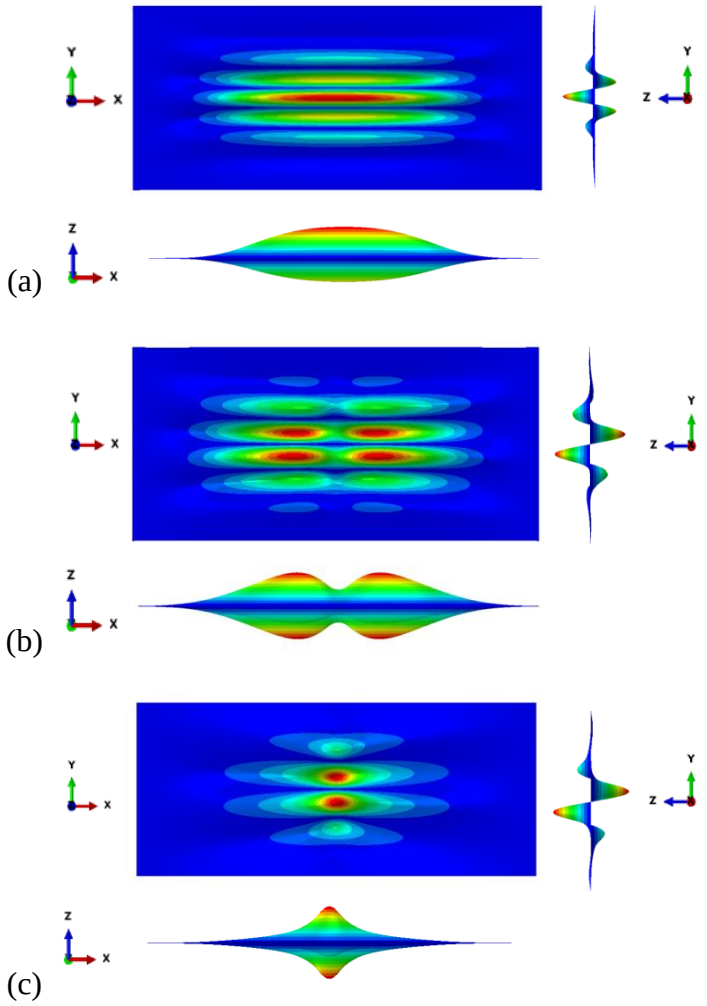

Figure 6.6: First buckling mode for clamped-ends stretching of thin inhomogeneous sheets as obtained from the buckling eigen value analysis with stiffness ratio: (a) $\rho = 1$; (b) $\rho = 0.5$; (c) $\rho = 2$.

6.4 POST-BUCKLING ANALYSIS

To perform the post-buckling analysis, the 1st eigen mode obtained from the buckling eigen value analysis is used as an initial imperfection in the sheet, where the imperfection magnitude is around 1% of the sheet thickness. In this case, the out-of-plane deformation shows similar characteristics as noticed in the buckling modes based on the

stiffness ratio (ρ). With $\rho > 1$, out-of-plane deformation is higher at the center and vice-versa. Overall, wrinkle response is found similar to the homogeneous clamped-ends stretching case, where wrinkles initiate at a critical strain, wrinkle amplitude first increases and then decreases with increasing nominal strain. In addition to that, the wrinkle affected regions are significantly different in these cases. Also, the evolution of wrinkles with increasing nominal strain shows a different trend as compared to the homogeneous thin sheet wrinkling case. In this case, the number of wrinkles starts to increase with increasing nominal strain. Figure 6.7 shows the out-of-plane deformation contours for an inhomogeneous sheet with stiffness ratio, $\rho = 1.1$ as it is stretched with clamped ends. It is noticed that the wrinkle amplitude is higher locally at the central (material 2) along the longitudinal direction, which is qualitatively similar to the buckling mode shape observed in the buckling eigen value analysis. Figure 6.8 shows the normalized wrinkle profile for this case along the mid-section of the sheet ($x = L_0/2$) for the strains corresponding to the contours shown in Figure 6.7. As clearly seen in the figure, the number of wrinkles keep increasing and consequently sheet flattening out is not seen in this case.

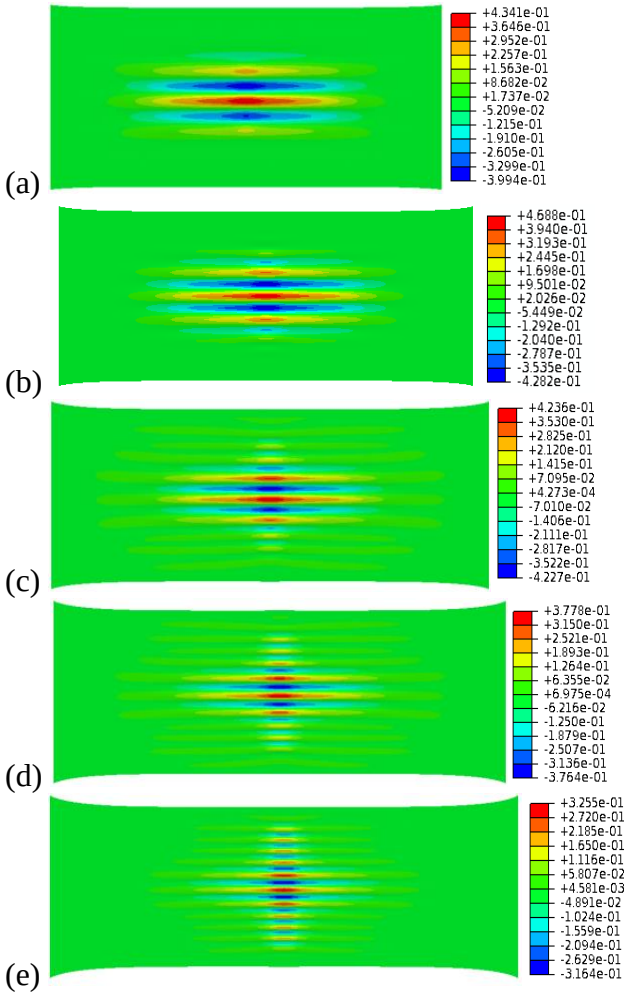

Figure 6.7: Out-of-plane deformation contours in an end-clamped thin inhomogeneous rectangular sheet with an aspect ratio α = 2.5 and β = 1000 and stiffness ratio, ρ = 1.1 under different nominal strains: (a) ε = 6%; (b) ε = 12%; (c) ε = 18%; (d) ε = 24%; (e) ε = 30%.

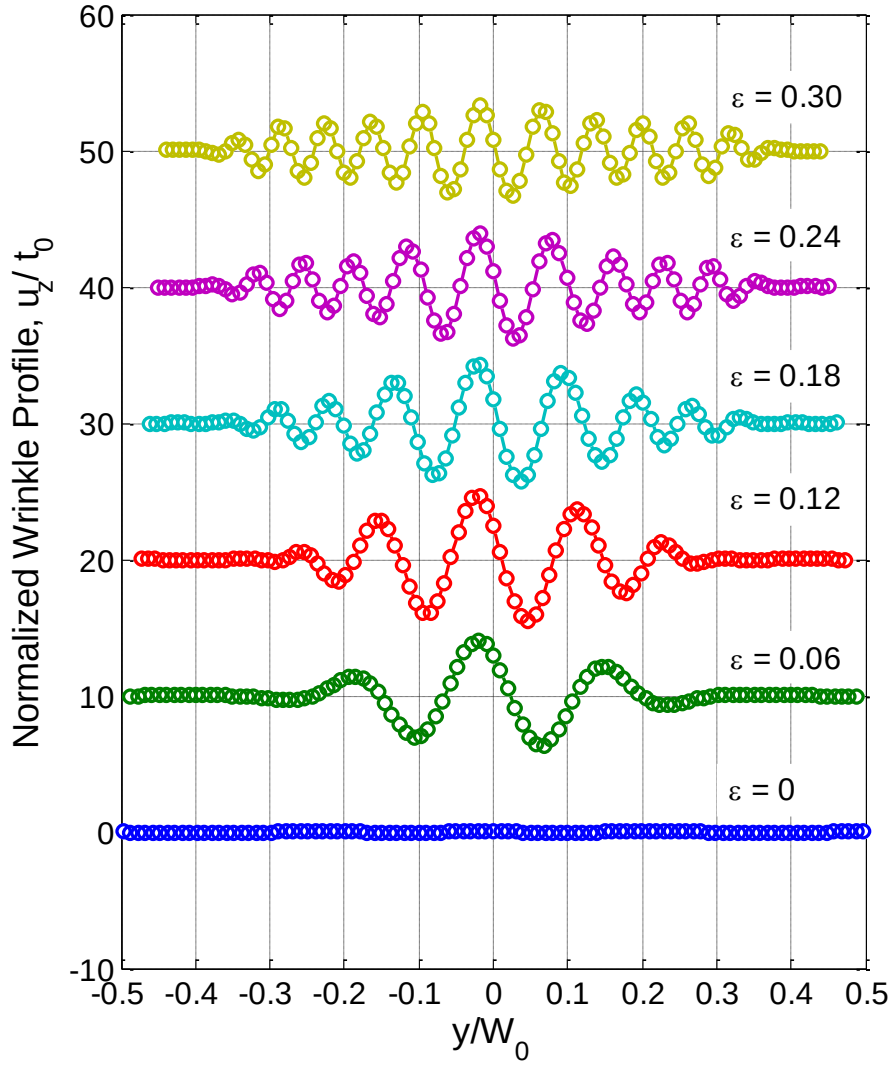

Figure 6.8: Normalized wrinkle profile for a thin inhomogeneous sheet with stiffness ratio, ρ = 1.1, along the mid-section ($x = L_0/2$) of the sheet with α = 2.5 and β = 1000, at different nominal strains.

Next, the wrinkle profile for a case with stiffness ratio smaller than 1 is shown. Figure 6.9 shows the out-of-plane deformation contours for an inhomogeneous sheet with stiffness ratio, ρ = 0.9 as it is stretched with clamped ends. In this case, the out-of-plane

deformation shows smaller amplitude at the center, qualitatively similar to that observed in the eigen value buckling analysis for stiffness ratio less than 1. Qualitatively similar to the previous case, the number of wrinkles keeps increasing in this case as nominal strain is increased and sheet flattening out is not observed. Figure 6.10 shows the normalized wrinkle profile for this case along the section offset from the mid-section of the sheet by 1.5*b* as marked in Figure 6.9a. Maximum wrinkle amplitude in this case does not exist along one particular transverse section in this problem, in contrast to the cases with stiffness ratio greater than 1 or the homogenous thin sheet case where maximum amplitudes exists along the sheet mid-section. We plot the normalized wrinkle profile along the section, $x = L_0/2 + 1.5b$ in Figure 6.10 corresponding to the out-of-plane deformation contours shown in Figure 6.9. As clearly seen in Figure 6.10, the number of wrinkles keep increasing and consequently the sheet flattening out is not observed in this case also. The wrinkling pattern in this case if found qualitatively similar to that shown in Figures 6.1a and 6.1b.

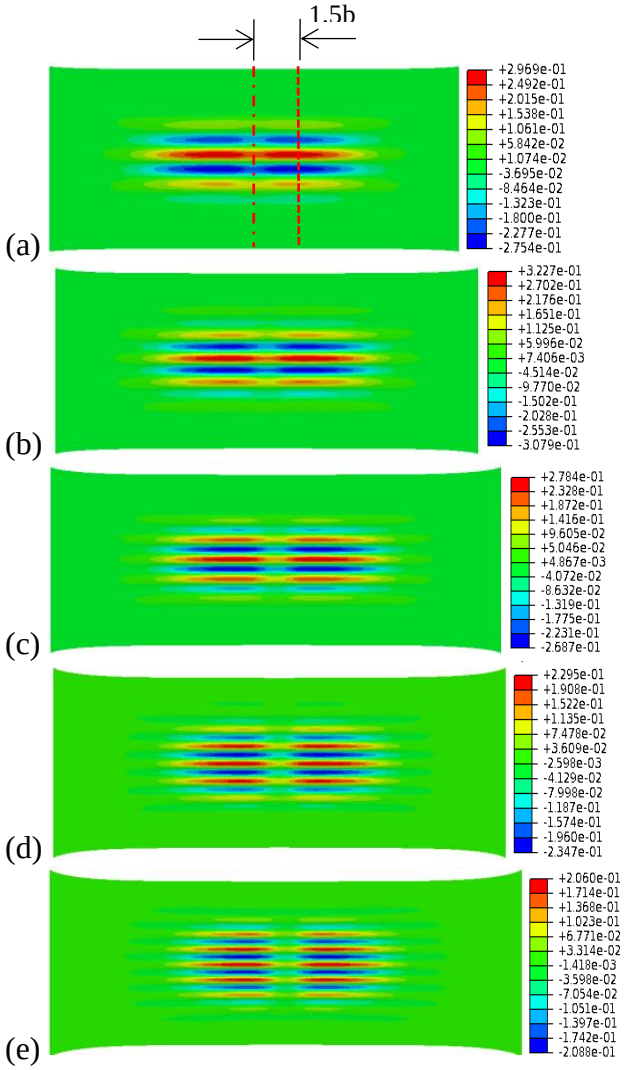

Figure 6.9: Out-of-plane deformation contours in an end-clamped thin inhomogeneous rectangular sheet with an aspect ratio α = 2.5 and β = 1000 and stiffness ratio, ρ = 0.9 under different nominal strains: (a) ε = 6%; (b) ε = 12%; (c) ε = 18%; (d) ε = 24%; (e) ε = 30%.

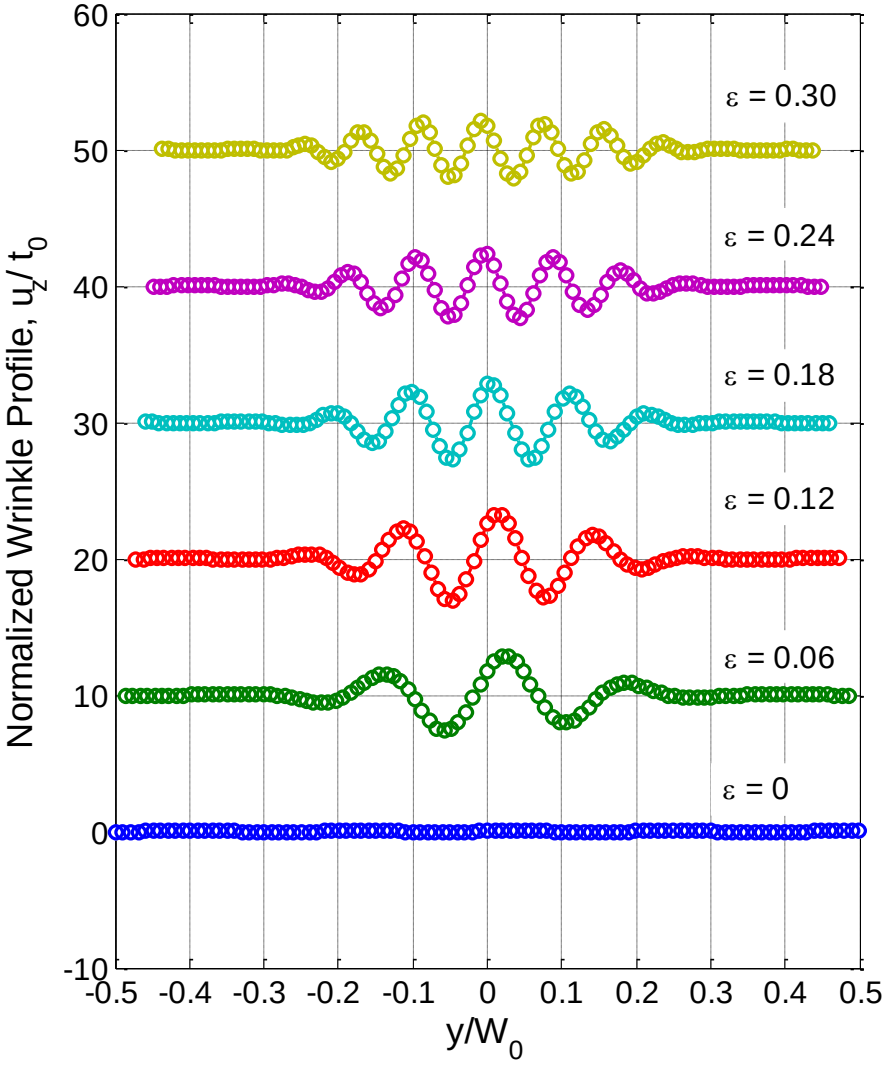

Figure 6.10: Normalized wrinkle profile for a thin inhomogeneous sheet with stiffness ratio, ρ = 0.9, along the transverse section ($x = L_0/2 + 1.5b$) of the sheet with α = 2.5 and β = 1000 at different nominal strains.

The wrinkle amplitude (A_0) is defined as $A_0 = [\max(u_z) - \min(u_z)]/2$ and plotted as a function of the nominal strain in Figure 6.11. It shows amplitude-strain response for inhomogeneous thin sheets under clamped-ends stretching for different stiffness ratios

(ρ), where Figures 6.11a and 6.11b shows the amplitude-strain response as stiffness ratio is decreased and increased respectively. The amplitude-strain response for the homogeneous thin sheet is also shown for the comparison. The differences found in this case as compared to the homogeneous thin sheet case are as follows; first, the critical strain for wrinkle initiation decreases with inhomogeneity for any stiffness ratio, $\rho \neq 1$; second, wrinkle amplitudes increase in presence of inhomogeneity; third, the number of wrinkles increase with increasing nominal strain and thus sheet flattening out with increasing nominal strain is not observed in inhomogeneous thin sheet stretching case. Although, Figures 6.11a and 6.11b shows that wrinkle amplitude decreases with nominal strain after its peak occurs, but this happens due to the increase in number of wrinkles, which keep increasing with strain and thus not allowing the sheet to flatten out. Also, if the stiffness ratio is relatively small or high, the wrinkle amplitude stops decreasing with increasing nominal strain. As observed for the stiffness ratio, $\rho = 0.5$, the wrinkle amplitude almost remains constant with increasing nominal strain. On the other hand, if the stiffness ratio is very close to 1, the wrinkling behavior is almost the same as in the inhomogeneous sheet. Figure 6.11b shows an amplitude-strain response for a case with $\rho = 1.01$, which shows an amplitude-strain response very close to the homogeneous thin sheet ($\rho = 1$).

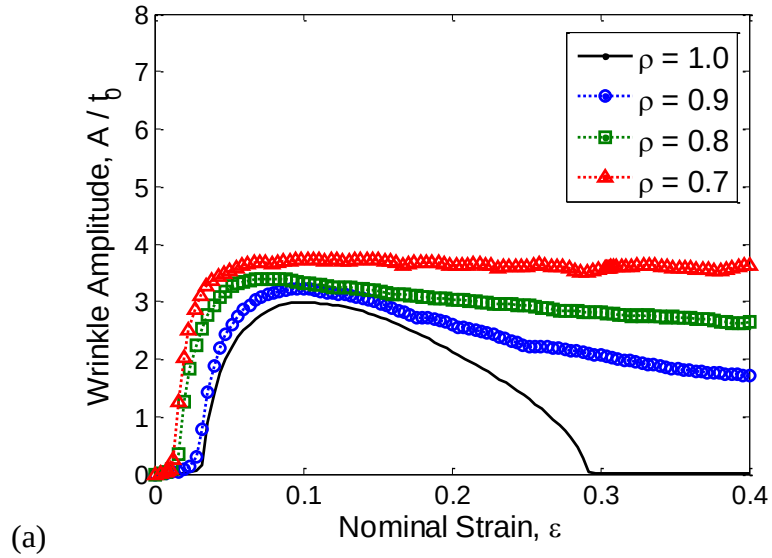

(a)

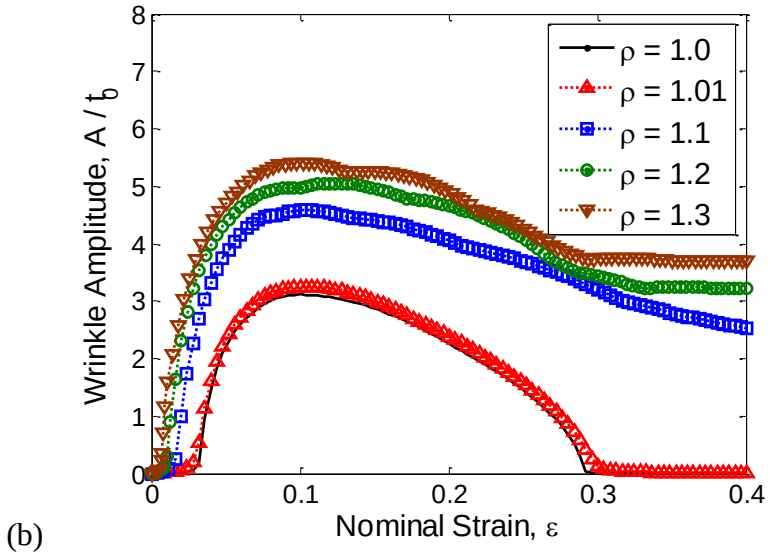

(b)

Figure 6.11: Amplitude-strain response for thin inhomogeneous thin sheets under clamped-ends stretching with: (a) stiffness ratios, $\rho \leq 1$; (b) stiffness ratios, $\rho \geq 1$.

Next, Figure 6.12 compares the change in number of wrinkles in inhomogeneous thin sheets while nominal strain is increasing with the homogeneous thin sheet under stretch. As already seen in the previous chapters that the number of wrinkles does not

change in case of homogenous thin sheets stretched with clamped ends. On the other hand, in presence of inhomogeneity, the number of wrinkles keeps increasing with strain. This is further shown in Figure 6.12, where number of wrinkles in inhomogeneous sheets with stiffness ratio, ρ = 1.1 and ρ = 0.9 are compared to the homogeneous sheet case.

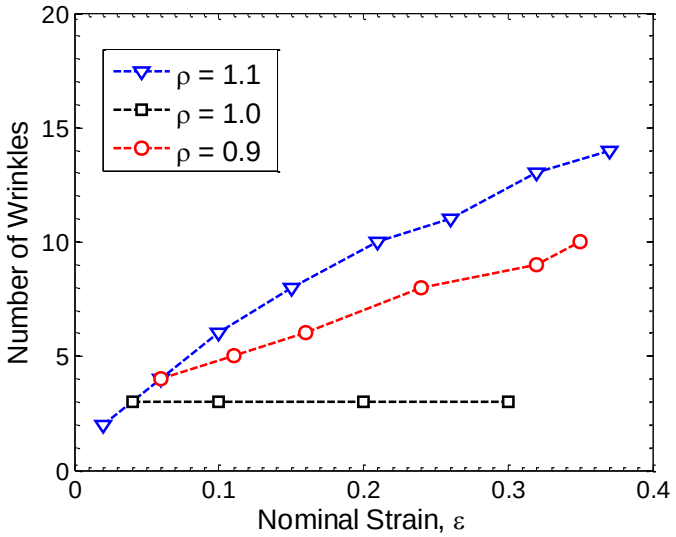

Figure 6.12: Change in number of wrinkles in thin inhomogeneous sheets with increasing nominal strain for different stiffness ratios (ρ) compared with the homogeneous thin sheet stretching case.

Figure 6.13 compares wrinkle wavelength of inhomogeneous sheets with an inhomogeneous sheet on a log-log scale. Similar to the homogenous thin sheet case, the wavelength of wrinkles in inhomogeneous sheets keep decreasing as nominal strain is increased. Though, the wavelength does not change as predicted by the scaling relation as discussed in chapter 3, however the results show that in the present case also, the wrinkle wavelength can be scaled with nominal strain.

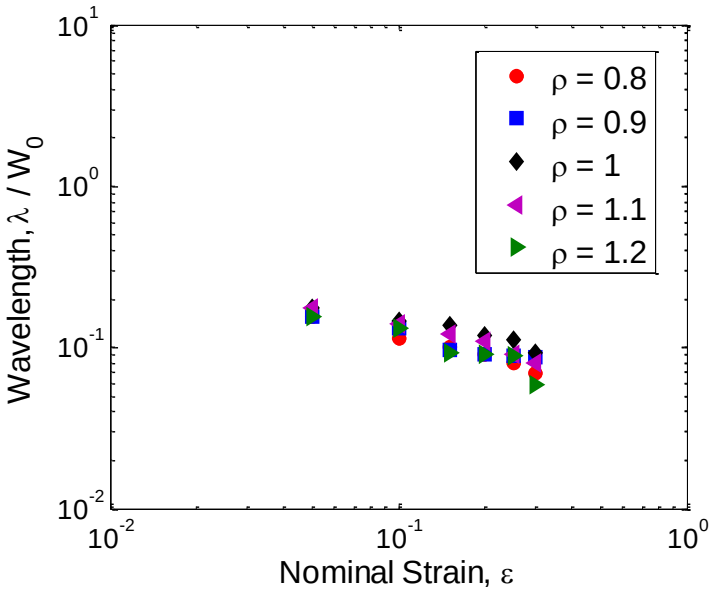

Figure 6.13: Change in average wrinkle wavelength with increasing nominal strain for different stiffness ratios (ρ) compared with the homogeneous thin sheet stretching case.

In case of stretching of thin inhomogeneous sheets with clamped ends, it is noticed that there are two reasons for wrinkling. First is the clamped-ends boundary condition which induces the transverse compression due to the boundary conditions. Second, the inhomogeneity in thin sheets also serves as a source of buckling. As already discussed, when inhomogeneous sheets are stretched it results in shear tractions at the interface of two materials. These shear tractions occur as a result of applied stretch and are able to induce transverse compression in the sheet. Thus, even in the absence of clamped-ends, the transverse compression is induced due to the inhomogeneous sheet properties. To illustrate this, we consider a case where a thin inhomogeneous sheet is subjected to stretch without clamps. In the absence of clamps, there is no shear traction at

the two ends but shear is present in the central region around the interface of two materials. Shear at the interface of two materials serve as a driving force for the sheet wrinkling even in the absence of clamps. Figure 6.14a shows the out-of-plane deformation contour for a thin inhomogeneous sheet with stiffness ratio, $\rho = 1.1$, which is stretched by 10% in the absence of clamps. The in-plane (α) and out-of-plane (β) aspect ratios assumed in this case are 2.5 and 100 respectively. Figure 6.14b shows the normalized wrinkle profile at different strain levels. Although the number of wrinkles increases with strain in this case also, wrinkles are relatively uniform in wavelength as compared to stretching in presence of clamps and again sheet flattening out with increasing nominal strain is not observed.

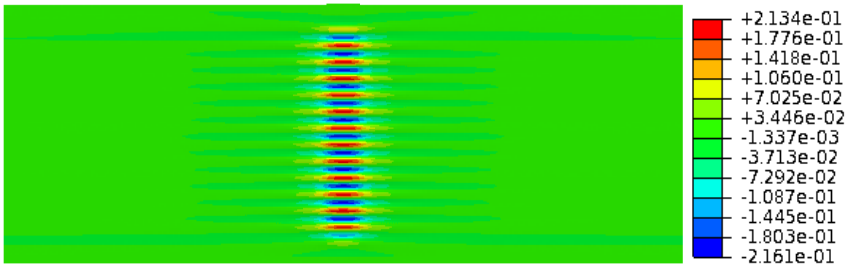

(a)

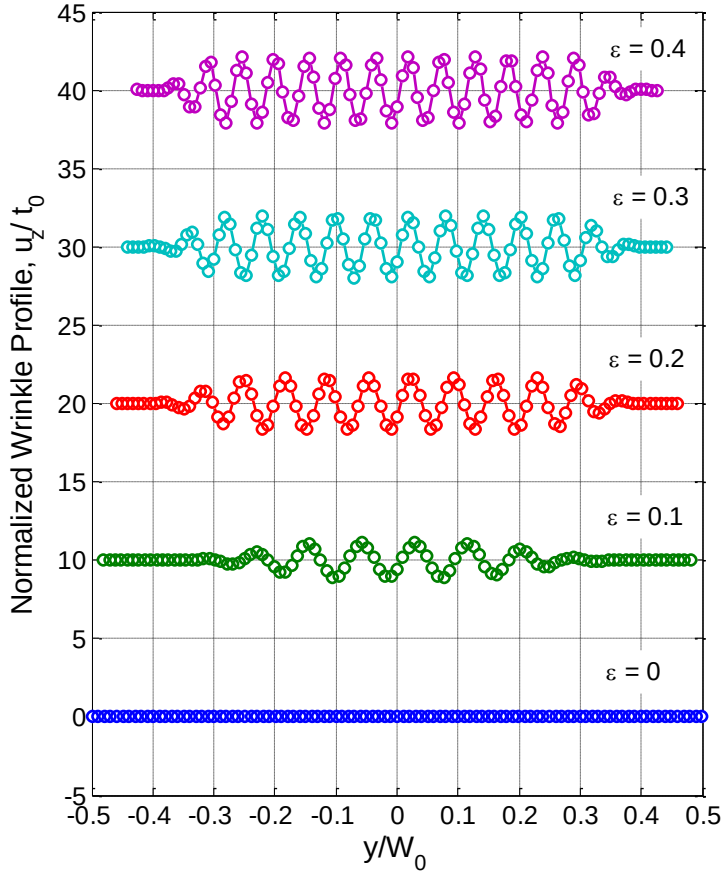

(b)

Figure 6.14: Thin inhomogeneous rectangular sheet with α = 2.5, β = 1000 and ρ = 1.1 subjected to uniaxial stretch in the absence of clamps: (a) showing the out-of-plane deformation contour at 10% nominal strain; (b) showing normalized wrinkle profile along the mid-section of the sheet under increasing nominal strain.

The amplitude-strain response for the inhomogeneous thin sheet without clamps is compared to the case with clamps in Figure 6.15. It is noticed that amplitude-strain response in absence of clamps is completely different from clamped-ended stretching case of homogeneous/inhomogeneous thin sheets. Wrinkle amplitude in this case increases monotonically after the onset of buckling. Hence, the non-monotonic wrinkle amplitude behavior with increasing strain as observed for both homogeneous and inhomogeneous thin sheets is due to the clamped-ends boundary condition. Thus, the role of clamped-ends boundary condition with respect to the homogeneous thin sheet is as follows: first due to clamped-ends boundary conditions, in-plane transverse compression is induced in the sheet which may or may not be sufficient to form wrinkles. In case of wrinkling, the clamped-ends boundary condition is further responsible for the non-monotonic behavior of wrinkle amplitude. Under increasing nominal strain, the wrinkle amplitude starts to decrease after reaching peak amplitude. It is understood that due to the clamped-ends, the biaxial tension in the sheet that is initially present only near the clamps, spreads with increasing nominal strain and hence decreasing the transverse compressive stress and consequently decreasing the wrinkle amplitude. Finally, under large strains, the sheet becomes free of in-plane transverse compression and hence wrinkles are not supported anymore. Both homogeneous and inhomogeneous thin sheets on stretching show qualitatively similar non-monotonic amplitude-strain response in presence of clamps provided that stiffness ratio (ρ) is within a certain range for inhomogeneous sheets.

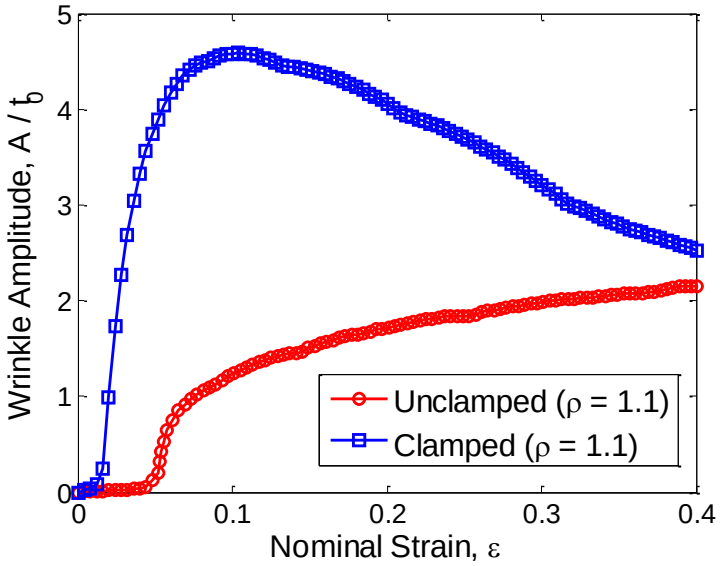

Figure 6.15: Comparison of wrinkle amplitude as a function of nominal strain for a thin inhomogeneous rectangular sheet when stretched uniaxially in the presence of clamps with the amplitude-strain response in the absence of clamps.

6.5 SUMMARY

In this chapter, the effect of inhomogeneity on thin sheet wrinkling was studied by varying the stiffness of inhomogeneity. It was found that in presence of inhomogeneity, the critical strains for onset of wrinkling decreases irrespective of the stiffness ratio. The wrinkling patterns found were also significantly different in this case as compared to the homogeneous case. Overall, the sheet was found more susceptible to wrinkling in presence of inhomogeneity with increase in wrinkle amplitudes. Further the flattening of sheet with increasing nominal strain was not observed in this case; instead the number of wrinkles was found increasing with increasing nominal strain. Also, it was found that non-monotonic behavior of wrinkle amplitude with increasing strain is because of the

clamping of sheet at two ends. For the homogeneous sheets, the clamped-ends boundary conditions promote wrinkling instability at small strains and suppress wrinkles under large strains.

CHAPTER 7

Conclusions and Future Studies

In this dissertation, stretch-induced wrinkling phenomenon in thin sheets is studied using a model problem. A thin rectangular sheet is clamped at two opposite ends and stretched. The model problem is studied numerically as well as experimentally. Following are the main outcomes of this study.

7.1 Stress Analysis of thin sheets

It is found that under clamped-ends stretching, transverse compressive stress develops in the sheet with the in-plane aspect ratio (α) greater than 1. Both clamped-ends boundary conditions and material's Poisson's ratio are crucial for inducing compression. Distribution and magnitude of compressive stress depend on both the in-plane aspect ratio (α) and the applied strain. Based on distribution of compressive stress, different phases of transverse compressive stress are predicted.

It is also found that magnitude of transverse compressive stress depend on sheet aspect ratio (α) and applied strain. Transverse compressive stress at each point in the sheet shows a non-monotonic behavior with nominal strain, i.e. it increases and then decreases with increasing nominal strain. Finally, there exists a critical strain for each aspect ratio at which transverse compression becomes zero. The stress magnitude is found to depend on sheet aspect ratio (α) only up to a limit. If sheet aspect ratio (α) is sufficiently large, stress magnitude becomes independent of aspect ratio (α) and becomes a function of nominal strain only. In such cases, sheet areas under compression near the

clamps do not interact with each other, and the compressive stress near the clamped ends depends on the applied strain.

Similar analyses for viscoelastic materials show qualitatively similar stress patterns. In addition to that, compressive stress magnitude increases with applied strain rate. In case of viscoelastic materials, critical strain for transverse compression to become zero depends on sheet aspect ratio (α) and the applied strain rate. The critical strain changes non-monotonically with increasing strain rate. When strain rate is sufficiently high/low, the critical strain is closer to the hyperelastic response due to the elastic response of the viscoelastic material at high or low strain rates.

7.2 WRINKLING OF THIN SHEETS

Through buckling and post-buckling analyses, it is observed that stretch-induced compressive stress is closely related to the sheet wrinkling in terms of wrinkles location and its behavior with applied strain. It is found that, as the aspect ratio (α) approaches 1, the critical strain for buckling increases and eventually no buckling modes can be found for $\alpha \leq 1$. The sheet thickness is a critical parameter in the buckling analysis; with lower thickness, the critical strain for buckling decreases. In addition, the regions affected by buckling are closely related to the distribution of transverse compression.

Post-buckling analysis further showed non-monotonic behavior of wrinkle amplitude with applied strain. The wrinkling is found to occur between two critical strains only. In between these two critical strain levels, the wrinkle amplitude increases, reaches its peak value and then finally start decreasing with increasing nominal strain. Qualitatively, for all sheets that show buckling, similar trend for wrinkle amplitude is

observed. With lower thickness, wrinkle amplitude and number of wrinkles is found to increase. Also, range of strain in which wrinkles are observed increase with decrease in thickness. Wrinkle response is found independent of material stiffness but it depends on material Poisson's ratio.

Next, experiments were conducted using a polyethylene sheets. The sheet was clamped and then stretched using an Instron machine under displacement control. Through the tests, non-monotonic behavior of wrinkling was confirmed. By comparing the results with the hyperelastic material response, it is found that wrinkle response is dependent on strain rate. Though, this dependence is very small upto 20% nominal strain. Beyond this point, there is considerable deviation from the hyperelastic response.

Further, material is characterized through uniaxial loading tests and relaxation tests under uniaxial stress. First, a hyper viscoelastic model was used to take into account the viscoelastic properties of the material. Although this model was found insufficient to capture the properties of the material, but the effect of viscoelastic properties on wrinkling was studied though this model.

To better model the material used in the experiments and to understand the experiments, a nonlinear viscoelastic model was used. A parallel network non-linear viscoelastic model was used, through which the material response under uniaxial tension and relaxation tests was captured fairly well. Overall, this model showed better comparison with the experiments as compared to the hyper viscoelastic model.

7.3 INHOMOGENEOUS SHEETS

During the course of experimental study on clamped-ends stretching of polyethylene, several effects of inhomogeneous material properties are observed. To study the effect of inhomogeneous properties on wrinkling, a model problem is chosen. In the model problem, stiffness of a clamped thin sheet is varied locally. A buckling eigen value analysis shows decrease in the critical strain for wrinkling by either increasing or decreasing the stiffness value of inhomogeneity. Also, the buckling modes show different out-of-plane displacement profile in case of inhomogeneous sheets.

Through post-buckling analyses, it is found that the wrinkle amplitude increases and the number of wrinkles also increase with increasing nominal strain in inhomogeneous sheets. Further, sheet flattening is not observed with increasing nominal strain. Overall, in case of inhomogeneity, sheet becomes more susceptible to winkling. It is also found that, in case of inhomogeneity wrinkling can occur even in the absence of clamped-edges, provided that sheet thickness is sufficiently small.

7.4 FUTURE STUDIES

In this study, the experiments with clamped-ends boundary conditions, except polyethylene experiments were also tried on a Mylar and rubber sheets. However, the experimental setup used in this study was found insufficient for these materials with relatively high/ low stiffness. In case of Mylar sheets, the problem was because of its high stiffness (nearly 10 times polyethylene), the methodology used for clamping was found inappropriate to hold the sheet during stretching. It was further tried to fix the sheet within the clamps using an epoxy, but even that was found insufficient to apply high

strains for wrinkling to occur. On the other hand, in case of rubber sheets, large out-of-plane deformation occurred due to its own weight and wrinkling due to the clamped-ends stretching cannot be analyzed properly in such situation. Thus, the experimental setup used for the experiments was found limited to the polyethylene sheets used in the present study because of its favorable stiffness value. A better experimental setup needs to be developed to test materials such as Mylar and Kapton because of their proposed applications in many of the inflatable space structures. With emerging technologies involving soft materials, understanding of wrinkling in these materials could be crucial; hence a better experimental framework is required to address all these related issues.

In the present study, we have shown that wrinkles form when certain critical conditions (geometry & strain) are satisfied, thus sheet flatness can be controlled by with appropriate loads. But one question still remains unanswered and that is how to suppress wrinkles. In some situations, it might not be possible to avoid wrinkles simply by avoiding critical conditions, thus more studies are required to explore the ideas that may be helpful in avoiding wrinkles. Zheng (2009) showed one such example in which dielectric actuation was used to suppress wrinkles in a dielectric elastomer. Orszulik et al. (2012) showed that with use fuzzy logic surface flatness of thin sheets can be controlled. As pointed out in the present study, the primary reason for wrinkling to occur is the transverse compressive stress in the sheet, which is a necessary condition for wrinkling. However, if compressive stresses are not allowed to build up to the critical level, the onset of buckling can be avoided. So, in order to avoid compressive stress reaching the critical levels, an in-plane tension that cancels the compressive effect may be induced by

use of an electric or magnetic field. For instance, in clamped-ends stretching case, if such a field is able to relax the transverse compression, it may avoid wrinkling under any strain and for any aspect ratio. Such a technique would be dependent on the material type that undergoes wrinkling. Reinforcing the thin sheet structures is another possible means of avoiding wrinkles. In order to use this method, the design of the reinforcement should be carefully analyzed otherwise this may actually act as wrinkle initiator instead of wrinkle arrestor. As shown in chapter 6, in case of inhomogeneous materials the critical strains for winkling decreases.

Appendix A

The boundary-value problem (BVP) as shown in Figure 1.8a contains a single loading parameter, δ, the end displacement, which is normalized by the length of the sheet to define the nominal strain, $\varepsilon = \delta / L_0$. The dimensions of the sheet are parameterized by two dimensionless ratios, $\alpha = L_0/W_0$ and $\beta = W_0/h_0$. The remaining physical parameters of the BVP depend on the constitutive model for the material. Regardless of the material model, the wrinkle amplitude normalized by the sheet thickness is a dimensionless quantity and can only be a function of the dimensionless parameters of the BVP. In general, we may write

$$A/h_0 = f\left(\varepsilon, \alpha, \beta; M_i, i = 1,2,3...\right) \tag{A.1}$$

where M_i (i = 1, 2, 3, …) represent a set of dimensionless parameters related to the material model.

In general, it can be concluded that the wrinkle amplitude as a function of the applied strain does not depend on the elastic stiffness of the material alone. In the case of a linear elastic material, it depends on Poisson's ratio, but not Young's modulus. In the case of an elastic-plastic material, it depends on the yield stress and hardening modulus, both normalized by the elastic modulus. If the material behavior is time dependent, the time or the loading rate can be normalized by the material time scale in the constitutive model so that the wrinkle amplitude becomes rate/time-dependent. A few specific material models are considered as follows.

Elastic materials

First, if the material is isotropic and linear elastic, the only dimensionless parameter in the material model is Poisson's ratio, and thus

$$A/h_0 = f(\varepsilon, \alpha, \beta; \nu) \tag{A.2}$$

If the material is isotropic and hyperelastic, described by the incompressible neo-Hookean model, the Poisson's ratio is invariably 0.5, and the material model does not have any other dimensionless parameter. Therefore,

$$A/h_0 = f(\varepsilon, \alpha, \beta) \tag{A.3}$$

More generally, the behavior of a hyperelastic material can be described by a strain energy potential function of one particular form, e.g., the Mooney-Rivlin form, the Ogden form, the Gent form, the Arruda-Boyce form, etc. Take the Mooney-Rivlin form as an example. The strain energy function is

$$W = C_1(\bar{I}_1 - 3) + C_2(\bar{I}_2 - 3) + D_1(J-1)^2 \tag{A.4}$$

where $\bar{I}_1$ and $\bar{I}_2$ are the first and second invariants of the deviatoric stretch matrix (the left Cauchy-Green strain tensor), J is the volume ratio (J = 1 if incompressible), and C_1, C_2, D_1 are three material parameters. For small deformation, the strain energy (A.4) can be reduced to the linear elastic form with the initial shear modulus and bulk modulus

$$G_0 = 2(C_1 + C_2) \text{ and } K_0 = 2D_1 \tag{A.5}$$

The ratio between the shear and bulk moduli defines an initial Poisson's ratio

$$\nu_0 = \frac{3K_0 - 2G_0}{2(3K_0 + G)} = \frac{3D_1 - 2C_1 - 2C_2}{6D_1 + 2C_1 + 2C_2} \tag{A.6}$$

In addition, a second dimensionless parameter may be defined as C_2/C_1. Therefore, the wrinkle amplitude takes the form

$$A/h_0 = f\left(\varepsilon, \alpha, \beta; \nu_0, C_2/C_1\right) \tag{A.7}$$

The compressible Neo-Hookean model is simply the Mooney-Rivlin model with $C_2 = 0$, and hence only the initial Poisson's ratio matters for the wrinkle amplitude.

Viscoelastic materials

Next consider the finite-strain viscoelastic model, which is a time domain generalization of the hyperelastic constitutive model, hence called hyper-viscoelasticity. Assuming incompressibility, the uniaxial stress in the current configuration at time t is

$$\sigma(t) = \sigma_0(t) + \int_0^t \frac{2\dot{G}(s)}{9G_0}\left(\bar{\lambda} + \frac{2}{\bar{\lambda}^2}\right)\sigma_0(t-s)ds \tag{A.8}$$

where $\sigma_0 = G_0\left(\lambda - \frac{1}{\lambda^2}\right)$ is the instantaneous stress by the incompressible neo-Hookean model with the initial shear modulus G_0 and $\lambda = 1 + \varepsilon$, $\bar{\lambda} = \lambda(t-s)/\lambda(t)$, $\dot{G}(t) = dG/dt$, and $G(t)$ is the time-dependent shear relaxation modulus. The relaxation modulus is assumed to take the form of a Prony series,

$$G(t) = G_0\left(1 - \sum_{i=1}^{N} g_i\left(1 - e^{-\frac{t}{\tau_i}}\right)\right) \tag{A.9}$$

With this material model, we have a set of time scales (τ_i, i = 1,…,N) and a set of dimensionless parameters (g_i, i = 1,…,N). Therefore, the wrinkle amplitude under a ramp loading with a constant strain rate ($\dot{\varepsilon}$) takes the form

$$A/h_0 = f\left(\varepsilon, \alpha, \beta, \dot{\varepsilon}\tau_i, g_i; i = 1,..., N\right) \tag{A.10}$$

It is expected that the time-dependent material behavior renders a history-dependent wrinkling behavior. For example, in the case of relaxation tests, the wrinkle amplitude is a function of time (t), which can be written as

$$A/h_0 = f\left(\varepsilon, \alpha, \beta, t/\tau_i, g_i; i = 1,..., N\right) \tag{A.11}$$

At the long-time limit ($t \to \infty$), it is expected that the wrinkle amplitude in the hyper-viscoelastic model approaches that in the hyperelastic model, namely

$$\lim_{t\to\infty} A/h_0 = f\left(\varepsilon, \alpha, \beta\right) \tag{A.12}$$

Elastic-Plastic materials

For a rate-independent elastic-plastic material, the constitutive model specifies the yield surface, the plastic flow rule, and hardening in addition to elasticity. To be specific, consider an elastic-plastic model with a Mises yield surface and associated plastic flow. Assuming isotropic hardening, the yield stress can be written as a function of the equivalent plastic strain, namely

$$\sigma_y = \sigma_y\left(\bar{\varepsilon}_p\right) \tag{A.13}$$

where $\bar{\varepsilon}_p = \int \sqrt{\frac{2}{3}\dot{\varepsilon}_{ij}^p \dot{\varepsilon}_{ij}^p}\, dt$ is a scalar measure of the accumulated plastic strain magnitude. A power-law hardening is often assumed in practice with

$$\sigma_y = \sigma_{y0} + H\bar{\varepsilon}_p^n \tag{A.14}$$

where σ_{y0} is the initial yield stress, H is the hardening modulus, and n is the hardening exponent. With such a constitutive model for the material, three dimensionless parameters are added into Eq. (A.1) along with the elastic Poisson's ratio, namely

$$\frac{A}{h_0} = f\left(\varepsilon, \alpha, \beta, \nu, \frac{\sigma_{y0}}{E}, \frac{H}{E}, n\right) \tag{A.15}$$

Hence in this case the elastic modulus of the material enters the equation through the ratios with the yield stress and the hardening modulus.

Nonlinear viscoelastic-viscoplastic materials

Many forms of nonlinear viscoelastic-viscoplastic constitutive models have been developed to describe time/rate-dependent, large deformation behavior of polymers. Here we consider a particular model due to Bergstrom and Boyce (1998). In the Bergstrom-Boyce (BB) model, the instantaneous stress can be calculated from a strain energy density function consisting of two parts

$$W = W_\infty\left(\bar{I}_1, \bar{I}_2, J\right) + W_t\left(\bar{I}_1^e, \bar{I}_2^e\right) \tag{A.16}$$

where $W_\infty\left(\bar{I}_1, \bar{I}_2, J\right)$ specifies the strain energy density in the fully relaxed material (the hyperelastic part) and $W_t\left(\bar{I}_1^e, \bar{I}_2^e\right)$ is the transient contribution to the strain energy that gradually relaxes with time with $\bar{I}_1^e$ and $\bar{I}_2^e$ being the two invariants of the elastic part of the left Cauchy-Green strain tensor. The total deformation gradient is decomposed into elastic and plastic parts as $\mathbf{F} = \mathbf{F}^e\mathbf{F}^p$. The specific functional form for the strain energy density is based on the eight-chain network model due to Arruda and Boyce (1993):

$$W_\infty = \mu_\infty \sum_{n=1}^{5} \frac{C_n}{\beta_\infty^{2n-2}}\left(\bar{I}_1^n - 3^n\right) + \frac{K}{2}\left(\frac{J^2-1}{2} - \ln J\right) \tag{A.17}$$

$$W_t = \mu_t \sum_{n=1}^{5} \frac{C_n}{\beta_t^{2n-2}}\left[\left(\bar{I}_1^e\right)^n - 3^n\right] \tag{A.18}$$

where C_n is a set of constants (C_1 = ½, C_2 = 1/20, …). In addition, the plastic strain rate is described in the form similar to creep:

$$D_{ij}^{p} = \dot{\gamma}\frac{s_{ij}}{\sqrt{2}\tau_e} \tag{A.19}$$

where s_{ij} is the deviatoric stress and $\tau_e = \sqrt{s_{ij}s_{ij}/2}$. The magnitude of the plastic strain rate is a function of the effective stress in the form

$$\dot{\gamma} = \dot{\gamma}_0\left(\sqrt{\frac{\bar{I}_1^e}{3}} - 1\right)^N \left(\frac{\tau_e}{\tau_0}\right)^m \tag{A.20}$$

Together, the material parameters in the BB model include the two shear moduli, μ_∞ and μ_t, the bulk modulus *K*, the coefficients β_∞ and β_t, and the parameters in (20), $\dot{\gamma}_0$, τ_0, *N*, and *m*. These material parameters would then affect the wrinkle amplitude through eight dimensionless groups, namely

$$A/h_0 = f\left(\varepsilon, \alpha, \beta, \frac{\dot{\varepsilon}}{\dot{\gamma}_0}; \frac{K}{\mu_\infty}, \frac{\mu_t}{\mu_\infty}, \beta_\infty, \beta_t, \frac{\tau_0}{\mu_\infty}, N, m\right) \tag{A.21}$$

which is also rate dependent for monotonic loading. In this case, the time scale depends on the single parameter, $\dot{\gamma}_0$, whereas multiple time scales are used in the Prony series for the viscoelastic materials (τ_i, i = 1,…, *N*).

Next, we consider the parallel network nonlinear viscoelastic model as discussed in Chapter 5. As already discussed, the material parameters in this model include the two shear moduli, μ_A and μ_B, *B*, *n* and *m*. These material parameters effect the wrinkle amplitude through seven dimensionless groups, namely

$$A/h_0 = f\left(\varepsilon, \alpha, \beta, \mu_B B^{\frac{1}{n}} \dot{\varepsilon}^{-\frac{m+1}{n}}; \frac{\mu_A}{\mu_B}, n, m\right) \tag{A.22}$$

In addition to the wrinkle amplitude, the other quantities may be analyzed similarly by the dimensional consideration. For example, the wrinkle wavelength normalized by the sheet thickness, λ/h_0, should depend on the same set of dimensionless parameters as the wrinkle amplitude for each material model. Moreover, the critical condition, in terms of either the applied strain or the applied force, can be expressed in similar forms:

$$\varepsilon_c = f_c(\alpha, \beta; M_i, i = 1,2,3...) \tag{A.23}$$

or

$$\frac{P_c}{EW_0h_0} = g_c(\alpha, \beta; M_i, i = 1,2,3...) \tag{A.24}$$

where E can be one of the material parameters with the unit of elastic modulus. Note that the dimensionless material parameters, M_i (i = 1, 2, 3, …), include the strain rate dependence for the time/rate-dependent constitutive models (e.g., viscoelastic and viscoplastic materials).

Appendix B

A jig is used to clamp the polyethylene sheet specimen at the two ends. Use of jig ensures that polyethylene sheet specimen (with width, W_0 = 100 mm) is clamped with right alignment with respect to the clamps with the sheet length (L_0). The sheet is attached to a pair of clamps at each end such that it is sandwiched between the two clamps. To attach the sheet with the clamps, a double-sided tape is used which holds the clamps and the sheet together at each end. In addition to that, once the sheet is clamped at two ends, each pair of clamps is secured by nut-bolts to grip the sheet firmly. Following section explains the steps followed to prepare the clamped sheet specimen.

First of all a bed is prepared to hold the clamps. A pair of sufficiently long pins is passed through the bed at the two ends which are protruding out of the bed. Figure B.1 schematically shows a bed with four pins P1, P2, P3 and P4 through which the clamps are held at the opposite ends. Each of the four clamps is prepared by attaching a double sided tape on one if its face as shown schematically in Figure B.2.

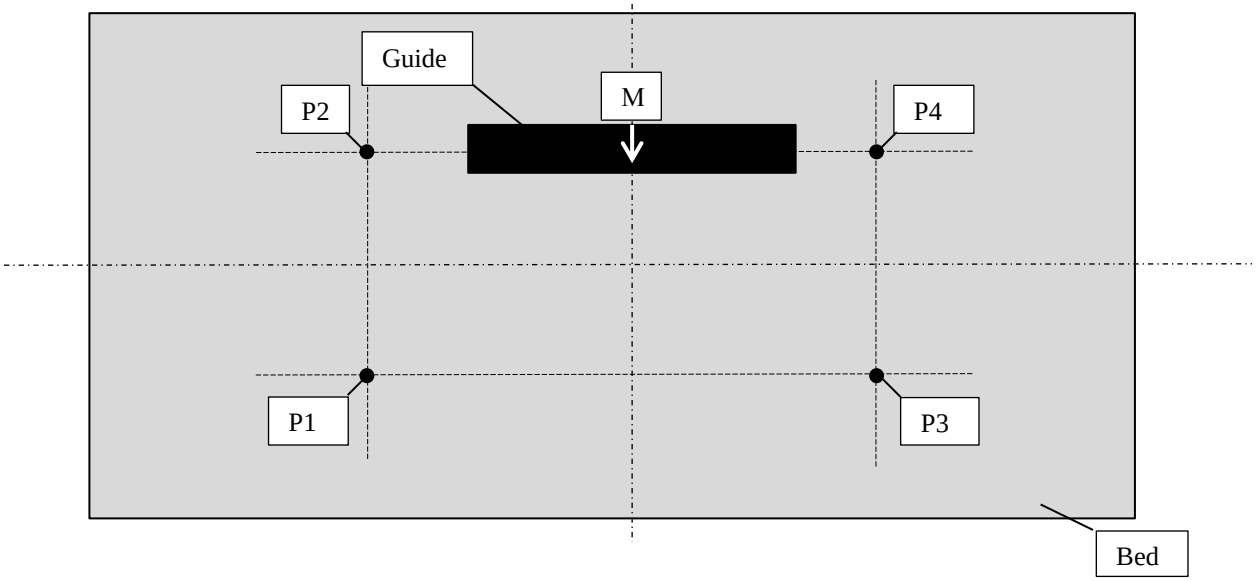

Figure B.1: Bed used to hold the clamps with specified distance and orientation with respect to each other.

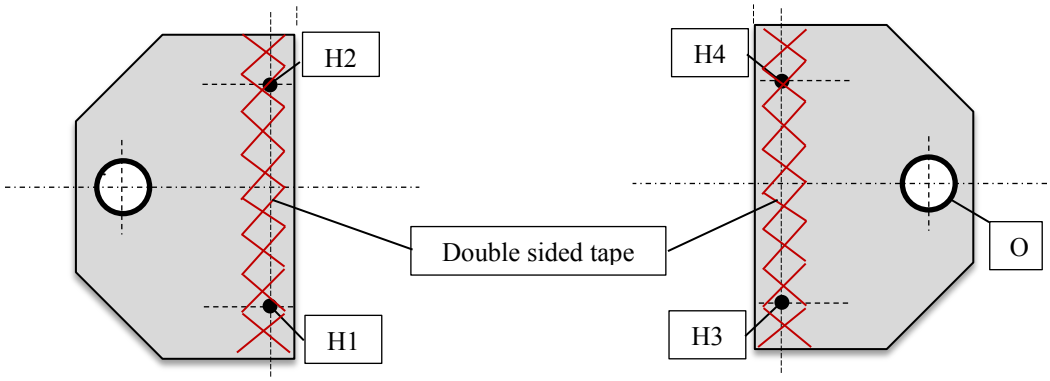

Figure B.2: A pair of clamps taped on one side using a double sided tape is slid through the pins in the bed such that hole H1, H2, H3 and H4 passes through pins P1, P2, P3 and P4 respectively.

Next, the clamps are slid through the pair of pins at each end such that hole H1, H2, H3 and H4 (marked in Figure B.2) passes through pins P1, P2, P3 and P4 respectively. The taped side of each clamp is kept facing upwards. Bed is designed in

such a way that it maintains the required distance (L_0) in-between the two clamps and the two clamps are in line, once they are passed through the pins. After passing the clamps through the pins, the polyethylene sheet specimen can be attached to it. Before the sheet specimen is attached, a plate with thickness same as two clamps is placed in between the two clamps at two ends. The purpose of this plate is to fill the space in between the two clamps so that the polyethylene sheet specimen does not sag down when it is attached to the two clamps. Also there is a guide running parallel to the specimen length, which is fixed to the bed as shown in Figure B.1. Before attaching the sheet to the clamps, the specimen is aligned with this guide to keep the sheet at right angle with respect to the clamps. To keep the speckle pattern (Figure B.3) at the center of the clamped sheet, the mark, 'M' is used as a reference to position the sheet just before attaching it to the clamps.

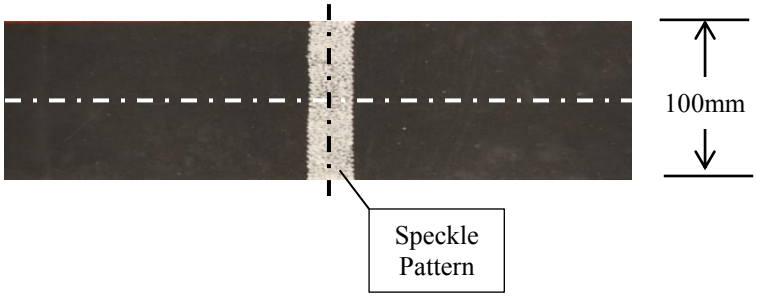

Figure B.3: A polyethylene sheet specimen to be attached on to the two clamps held positioned on the bed using the pins.

Once the sheet is attached to one clamp at each end, second pair of similar clamps with double sided tape facing downwards is slid through the same pins P1, P2, P3 and P4. This way the sheet specimen is sandwiched between a pair of clamps at each end. Once

the sheet is firmly attached with the clamps, the pins are removed and a sheet with length, L_0 and width, W_0 (= 100 mm) is clamped at two ends as shown in Figure B.4.

Two clamps at each end are further secured together by using nut-bolt assembly through holes H1, H2, H3 and H4. This avoids any slipping of the sheet specimen with respect to the clamps while stretching the sheet. To hold the clamped sheet specimen in the Instron machine, the type of grips used are shown in Figure B.5. The clamps are pinned by passing pins through holes 'O' in the clamped sheet assembly (Figure B.4) and the grips (Figure B.5).

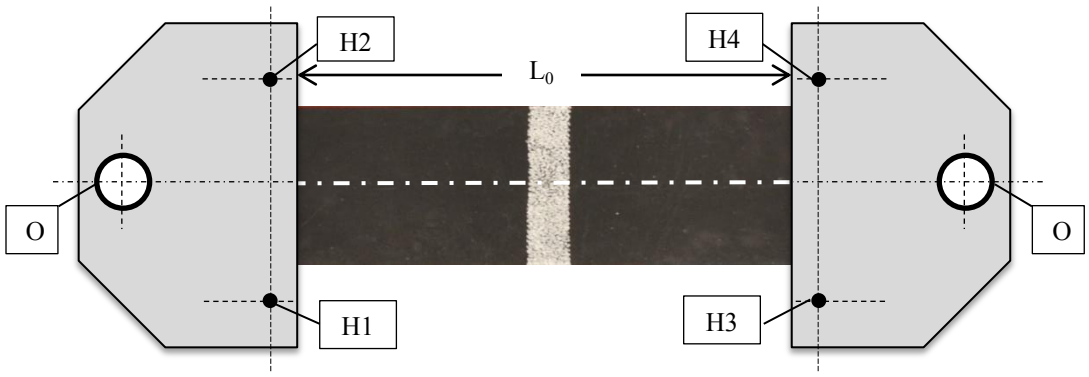

Figure B.4: After attaching the second pair of clamps on top of polyethylene specimen, the clamped sheet specimen is released from the bed and bolts are passed through holes H1, H2, H3 and H4 to tightly secure the clamps at each end.

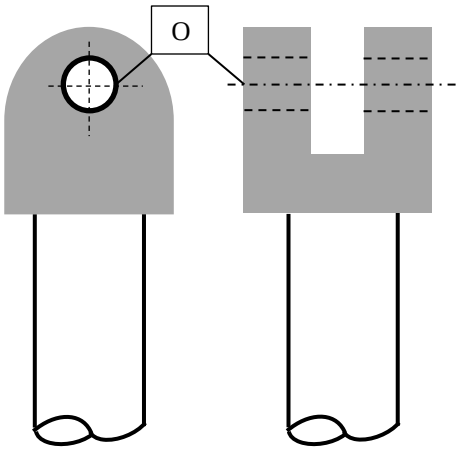

Figure B.5: Grips used to hold the clamps in the Instron machine by passing a pin through hole ‘O’ in the clamps and the grips.

References

1. ABAQUS, 2012. Theory and User's Manual, Version 6.12.
2. Aguirre, F., Kyriakides, S. and Yun, H.D., 2004. Bending of steel tubes with Lüders bands, International Journal of Plasticity 20, 1199–1225.
3. Alder, A. L., Mikulas, M. M., and Hedgepeth, J. M. (2000). Static and dynamic analysis of partially wrinkled membrane structures. In Proc. 41st AIAA/ASME/ASCE/AHS/ASC Structures, Structures Dynamics, and Material Conference and Exhibit. Atlanta. AIAA-2000-1810.
4. Benthem, J.P., 1963. A Laplace transform method for the solution of semi-infinite and finite strip problems in stress analysis. Q. J. Mech. Appl. Math. 16, 413-429.
5. Bergstrom J.S. and Boyce, M.C., 1998. Constitutive Modeling of the Large Strain Time-Dependent Behavior of Elastomers, *J. Mech. Phys.* Solids 46, 5, 931-954.
6. Blandino, J.R., Johnston, J.D. and Dharmasi, U.K., 2002. Corner Wrinkling of a Square Membrane Due to Symmetric Mechanical Loads. Journal of Spacecraft and Rockets 39 (5), 717-724.
7. Blonk, B.J., Moore, J.D., Patrick, B.G. and Flint, E.M., 2006. Chapter 2 in Recent Advances in Gossamer Spacecraft (C.H. Jenkins, Ed.), AIAA Progress in Astronautics and Aeronautics Series 212, 45-108.
8. Block, J., Straubel, M., Wiedemann, M., 2011. Ultralight deployable booms for solar sails and other large gossamer structures in space, Acta Astronautica 68, 984–992.
9. Burton, K., Park, J. H., Taylor, D.L., 1999. Keratocytes Generate Traction Forces in Two Phases, Molecular Biology of the Cell 10, 3745–3769.
10. Burton, K., Taylor, D.L., 1997. Traction forces of cytokinesis measured with optically modified elastic substrata. Nature 385, 450-454.
11. Coman, C.D., 2007. On the applicability of tension field theory to a wrinkling instability problem. Acta Mech. 190, 57–72.
12. Coman, C.D., Haughton, D. M., 2006. Localized wrinkling instabilities in radially stretched annular thin films. Acta Mech. 185, 179-200.

13. Cerda, E., 2005. Mechanics of scars, Journal of Biomechanics 38, 1598–1603.
14. Cerda, E., Mahadevan, L., 2003. Geometry and Physics of Wrinkling, Physical Review Letters 90, 074302.
15. Cerda, E., Ravi-Chandar, K., Mahadevan, L., 2002. Wrinkling of an elastic sheet under tension, Nature 419, 579-580.
16. Chung, J.Y., Nolte, A.J., and Stafford, C.M., 2011. Surface Wrinkling: A Versatile Platform for Measuring Thin-Film Properties, Adv. Mater. 23, 349–368.
17. Danielson, D.A., Natarajan, S., 1975. Tension field theory and the stress in stretched skin. J. Biomech. 8, 135–142.
18. Diaby, A., Le van, A., Wielgosz, C., 2006. Buckling and wrinkling of prestressed membranes. Finite Elements in Analysis and Design 42, 992-1001.
19. Fischer, F.D., Rammerstorfer, F.G., Friedl, N., 2003. Residual Stress-Induced Center Wave Buckling of Rolled Strip Metal. ASME Journal of Applied Mechanics 70, 84-90.
20. Fischer, F.D., Rammerstorfer, F.G., Friedl, N., Wieser, W., 2000. Buckling phenomena related to rolling and levelling of sheet metal. International Journal of Mechanical Sciences 42, 1887-1910.
21. Friedl, N., Rammerstorfer, F.G., Fisher, F.D., 2000. Buckling of stretched strips. Computers and Structures 78, 185-190.
22. Garbe, G.P., Wie, B., Murphy, D., Ewing, A., Lichodzewski, L., Derbes, B., Campbell, B., Wang, J., Taleghani, B., Canfield, S.L., Beard, J.W. III, Peddieson, J., 2006. Chapter 5 in Recent Advances in Gossamer Spacecraft (C.H. Jenkins, Ed.), AIAA Progress in Astronautics and Aeronautics Series 212, 191-261.
23. Geminard, J.-C., Bernal, R., and Melo, F., 2004. Wrinkle formations in axi-symmetrically stretched membranes, Eur. Phys. J. E 15, 117-126.
24. Hallai, J.F., Kyriakides, S., 2011. On the effect of Lüders bands on the bending of steel tubes. Part I: Experiments, International Journal of Solids and Structures 48, 3275–3284.

25. Harris, A.K., Wild, P., Stopak, D., 1980. Silicone rubber substrata: a new wrinkle in the study of cell locomotion, Science 208, 177–179.
26. Healey, T.J., Li, Q., Cheng, R.B., 2013. Wrinkling Behaviour of Highly Stretched Rectangular Elastic Films via Parametric Global Bifurcation, Journal of Nonlinear Science, *in Press.*
27. Huang, J., Juszkiewicz, M., H. de Jeu, W., Cerda, E., Emrick, T., Menon, N., Russell, T.P., 2007. Capillary Wrinkling of Floating Thin Polymer Films. Science 317, 5838, 650-653.
28. Iwasa, T., Natori, M.C., Higuchi, K., 2004. Evaluation of tension field theory for wrinkling analysis with respect to the post-buckling study. Journal of Applied Mechanics 71, 532-540.
29. Jacques, N., Elias, A., Potier-Ferry, M., Zahrouni, H., 2007. Buckling and wrinkling during strip conveying in processing lines, Journal of Materials Processing Technology 190, 33–40.
30. Jacques, N., Potier-Ferry, M., 2005. On mode localisation in tensile plate buckilng. C. R. Mecanique 333, 804–809.
31. Jang, W.Y., Kyriakides, S., 2009. On the crushing of aluminum open-cell foams: Part II analysis, International Journal of Solids and Structures 46, 635–650.
32. Jenkins, C. H. M., Hossain, A., Woo, K., Igawa, H., Wang, J., Sleight, D., and Tessler, A., 2006. Chapter 3 in Recent Advances in Gossamer Spacecraft (C. H. Jenkins, Ed.), AIAA Progress in Astronautics and Aeronautics Series 212, 109-163.
33. Johnston, J.D., 2002. Finite element analysis of wrinkled membrane structures for sunshield applications. In: Proc. 43rd AIAA/ASME/ASCE/AHS/ASC Structures, Structural Dynamics and Materials Conference, Denver, Colorado. AIAA 2002-1456.
34. Johnson, L., Whorton, M., Heaton, A., Pinson, R., Laue, G., Adams, C., 2011. NanoSail-D: A solar sail demonstration mission, Acta Astronautica, 68, 571–575.

35. Johnson, W.N., 2009. Space-based Solar Power: Possible Defense Applications and Opportunities for NRL Contributions. NRL/FR/7650--09-10,179
36. Kim, T.Y., Puntel, E., Fried, E., 2012. Numerical study of the wrinkling of a stretched thin sheet. International Journal of Solids and Structures, 49, 771-782.
37. Kim, J. B., Yoon, J. W. and Yang, D. Y., 2003. Investigation into the wrinkling behaviour of thin sheets in the cylindrical cup deep drawing process using bifurcation theory. International Journal for Numerical Methods in Engineering, 56, 1673–1705.
38. Lee, K., Lee, S.W., 2002. Analysis of gossamer space structures using assumed strain formulation solid shell elements. In: Proc. 43rd AIAA/ASME/ASCE/AHS/ASC Structures, Structural Dynamics and Materials Conference, Denver, Colorado. AIAA 2002-1559.
39. Leifer, J., Belvin, W. K., 2003. Prediction of wrinkle amplitudes in thin film membranes using finite element modeling. 44th AIAA/ASME/ASCE/AHS/ASC Structures, Structural Dynamics and Materials Conference, Norfolk, VA. AIAA 2003-1983.
40. Liu, X., Jenkins, C. H. and Schur, W. W., 2001. Large deflection analysis of pneumatic envelopes using a penalty parameter modified material model. Finite Elements in Analysis and Design 37, 233-251.
41. Luo, P., Chao, Y., Sutton, M., Peters, W., 1993. Accurate measurement of three-dimensional deformations in deformable and rigid bodies using computer vision. Exp. Mech. 33, 123-132
42. Mansfield, E. H., 1970. Load transfer via a wrinkled membrane. Proc. Roy. Soc. Lond. A. 316, 269-289.
43. Miyamura, T., 2000. Wrinkling on stretched circular membrane under in-plane torsion: Bifurcation analyses and experiments, Engineering Structures 23, 1407–1425.

44. Nayyar, V., Ravi-Chandar, K., Huang, R., 2011. Stretch-induced stress patterns and wrinkles in hyperelastic thin sheets, International Journal of Solids and Structures 48, 3471-3483.
45. Orszulik, R.R., Shan, J., 2012. Fuzzy logic active flatness control of a space membrane structure, Acta Astronautica 77, 68–76.
46. Pipkin, A. C., 1986. The relaxed energy density for isotropic elastic membrane. IMA Journal of Applied Mathematics 36, 85-99.
47. Peypoudat, V., Defoort, B., Lancour, D., Brassier, P., Couls, O.L., Langlois, S., Lienard, S., Bernasconi, M., Gotz, M., 2005. Development of a 3.2m-long inflatable and rigidizable solar array breadboard. In: Proc. 46th AIAA/ASME/ASCE/AHS/ASC Structures, Structural Dynamics and Materials Conference, Austin, Texas. AIAA 2005-1881.
48. Puntel, E., Deseri, L., Fried, E., 2011. Wrinkling of a stretched thin sheet. Journal of Elasticity 105, 137-170.
49. Rammerstorfer, F. G., Fischer, F. D., Friedl, N., 2001. Buckling of Free Infinite Strips Under Residual Stresses and Global Tension. ASME Journal of Applied Mechanics 68, 399-404.
50. Redell, F.H., Kleber, J., Lichodziejewski, D., Greschik, G., 2005. Design parameters for wrinkle reduction in membrane space structures. In: Proc. 46th AIAA/ASME/ASCE/AHS/ASC Structures, Structural Dynamics and Materials Conference, Austin, Texas. AIAA 2005-1879.
51. Sakamoto, H., Park, K.C., 2005. Design parameters for wrinkle reduction in membrane space structures. In: Proc. 46th AIAA/ASME/ASCE/AHS/ASC Structures, Structural Dynamics and Materials Conference, Austin, Texas. AIAA 2005-1974.
52. Segedin, R.H., Collins, I.F., Segedin, C.M., 1988. The elastic wrinkling of rectangular sheets. Int. J. Mech. Sci. 30(10), 719-732.

53. Simo, J. C., "On a Fully Three-Dimensional Finite-Strain Viscoelastic Damage Model: Formulation and Computational Aspects," Computer Methods in Applied Mechanics and Engineering 60, 153–173, 1987.
54. Sleight, D.W., Michii, Y., Lichodziejewski, D., Derbes, B., Mann, T.O., Slade, K.N., and Wang, J.T., 2005. Finite element analysis and test correlation of a 10-meter inflation-deployed solar sail. In: Proc. 46th AIAA/ASME/ASCE/AHS/ASC Structures, Structural Dynamics and Materials Conference, Austin, Texas. AIAA 2005-2121.
55. Stafford, C.M., Harrison, C., Beers, K.L., Karim, A., Amis, E. J., Vanlandingham, M. R., Kim, H. C., Volksen, W., Miller, R. D., and Simonyi, E. E., 2004. A buckling-based metrology for measuring the elastic moduli of polymeric thin films, Nat. Mater. 3, 545.
56. Steigmann, D.J., 1990. Tension-field theory. Proc. R. Soc. Lond. Ser. A, Math. Phys. Sci. 429, 141–173.
57. Steigmann, D.J., 2008. Two-dimensional models for the combined bending and stretching of plates and shells based on three-dimensional linear elasticity. Int. J. Eng. Sci. 46, 654–676.
58. Stein, M. and Hedgepeth, J. M., 1961. Analysis of partly wrinkled membranes. NASA Technical Note, D-813.
59. Sutton, M.A., Orteu J.J., Schreier, H.W., 2009. Image correlation for shape, motion and deformation measurements: basic concepts, theory and applications. Springer, New York. doi:10.1007/978-0-387-78747-3
60. Szyszkowski, W, Glockner, P.G., 1987. Spherical membranes subjected to vertical concentrated loads: an experimental study. Engineering Structures 9(3), 183-192.
61. Takei, A., Brau, F., Roman, B., Bico, J., 2011. Stretch-induced wrinkles in reinforced membranes: From out-of-plane to in-plane structures, EPL 96, 64001.
62. Talley, C., Clayton, W., Gierow, P., McGee, J., and Moore, J., 2002. Advanced membrane materials for improved solar sail capabilities. In: Proc. 43rd

AIAA/ASME/ASCE/AHS/ASC Structures, Structural Dynamics and Materials Conference, Denver, Colorado. AIAA 2002-1561.

63. Tessler, A., Sleight, D.W., Wang, J.T., 2005. Effective Modeling and Nonlinear Shell Analysis of Thin Membranes Exhibiting Structural Wrinkling. Journal of Spacecraft and Rockets 42, 287-298.
64. Tomita, Y. and Shindo, A., 1988. Onset and growth of wrinkling in thin square plate subjected to diagonal tension. Int. J. Mech. Sci. 30, 921-931.
65. Timoshenko, S.P. and Gere, J.M., 1985. *Theory of elastic stability*. McGraw-Hill.
66. Wagner, H., 1929. Flat sheet metal girder with very thin metal web. *Zeitschrift f¨ur Flugtechnik und Motorluftschiffahrt* 20, 200-314.
67. Wang, X., Zheng, W., Hu, Y.R., 2007. Active Flatness Control of Membrane Structures Using Adaptive Genetic Algorithm. Proc. of SPIE, vol. 6572, 652704. International Journal of Solids and Structures 46, 1516–1526.
68. Wang, C.G., Du, X.W., Tan, H.F., He, X.D., 2009. A new computational method for wrinkling analysis of gossamer space structures. International Journal of Solids and Structures 46, 1516–1526.
69. Wong, Y.W., Pellegrino, S., 2006a. Wrinkled membranes. Part I: Experiments. Journal of Mechanics of Materials and Structures 1, 1-23.
70. Wong, Y.W., Pellegrino, S., 2006b. Wrinkled membranes. Part II: Analytical models. Journal of Mechanics of Materials and Structures 1, 25-59.
71. Wong, Y.W., Pellegrino, S., 2006c. Wrinkled membranes. Part III: Numerical simulations. Journal of Mechanics of Materials and Structures 1, 61-93.
72. Wu, C.H., 1978. Nonlinear wrinkling of nonlinear membranes of revolution. J. Appl. Mech. 45, 533–538.
73. Yu, T. X. and Johnson, W., 1982. The buckling of annular plates in relation to the deep-drawing process, International Journal of Mechanical Sciences 24 (3), 175-188.
74. Zheng, L., 2009. Wrinkling of Dielectric Elastomer Membranes. PhD Thesis, California Institute of Technology, Pasadena, CA.

Vita

Vishal attended high school at D.A.V. College, Amritsar, India and graduated in May, 2004. After graduating from high school, he enrolled at Panjab University, Chandigarh, India for undergraduate studies. He graduated with a Bachelor's degree in Mechanical Engineering with honors in year 2008. After completing his Bachelor's degree in May 2008, he joined the Master's degree program in the Department of Aerospace Engineering & Engineering Mechanics at the University of Texas at Austin under the advisement of Dr. Rui Huang. In August 2010, after finishing his master's degree he joined the Ph.D. program and continued working under the supervision of Dr. Rui Huang and co-supervision of Dr. K. Ravi-Chandar. For his research work at UT Austin, Vishal studied stretch-induced wrinkling in thin sheets.

Email address: vishal.nayyar@utexas.edu

This dissertation was typed by Vishal Nayyar.